Study of the Neutral B Meson Oscillations using the OPAL Detector

Hideto Fukui

Doctral Thesis

Submitted to
Graduate School of Science and Technology, Kobe University

March 6, 1995

Abstract

This thesis reports the study of the time dependent oscillation of neutral B mesons using the OPAL detector at LEP. Events with two leptons (dilepton events) were selected from 1991–1993 data, corresponding to about 1.5 million multihadron events. By fitting the observed proper time distributions for unlike-sign lepton events and like-sign lepton events simultaneously, the mass difference of B_d meson was obtained. The result is $\Delta m_d = 0.462\ ^{+0.040}_{-0.053}$ (stat.) $^{+0.037}_{-0.036}$ (sys.) psec^{-1}. At the same time the lower limit of the mass difference of B_s meson was set to be $\Delta m_s >$ 2.2 psec^{-1} at 95% C.L.. Based on these results obtained from this analysis, the constraint of the Cabbibo-Kobayashi-Maskawa Matrix elements was calculated and some discussions are given.

Contents

Chapter 1

Introduction

The unified electroweak theory, which was proposed by S. Weinberg and A. Salam in 1967-1968 [1], can explain the various phenomena of elementary particle physics and no contradictory experimental observations have been found so far. This theory and the Quantum Chromo Dynamics (QCD) which describes the interaction between quarks form the so-called "Standard Model". This model, however, includes a lot of free parameters which can not be decided theoretically; for example, the gauge coupling constants, the fermion masses, the Higgs mass and the quark mixing angles. To complete this theory, many experiments have tried to measure these free parameters. This theory can predict some interesting phenomena. Among them, B^0-$\bar{\mathrm{B}}^0$ mixing is one of the predictions from the Standard Model.

The first observation of the B^0-$\bar{\mathrm{B}}^0$ mixing was reported by UA1 experiment in 1987 [2]. After that, ARGUS collaboration and CLEO collaboration observed the B^0-$\bar{\mathrm{B}}^0$ mixing using the decay mode, $\Upsilon(4s) \rightarrow \mathrm{B}^0\bar{\mathrm{B}}^0 \rightarrow \ell\ell\mathrm{X}$ [3]. This phenomenon has been also reported from LEP experiments and studied very well. But all the studies suffered from low statistics and the precision of these measurements was limited by a statistical fluctuation.

Nowadays, LEP is running very smoothly and all the experimental groups have collected about 1.5 million $\mathrm{Z}^0 \rightarrow \mathrm{q}\bar{\mathrm{q}}$ decays each. With high statistics of data, not only the average B^0-$\bar{\mathrm{B}}^0$ mixing but also the oscillation of the neutral B mesons can be studied. At first, ALEPH collaboration reported the observation of the $\mathrm{B_d}$ meson oscillation using events which contain D^* in one hemisphere and a lepton in the other hemisphere [4]. Next, ALEPH reported the neutral B meson oscillations using dilepton events [5]. The latter technique is very similar with the technique used in this analysis. For $\mathrm{B_d}$ oscillation measurements, the OPAL collaboration already published the results using two techniques; one of them is by using a jet-charge technique for events including D^* and a lepton in one hemisphere [6] and the other is by using events including D^* and a lepton for each hemisphere [7] like a previous publication of ALEPH. DELPHI also reports the $\mathrm{B_d}$ meson oscillation using D^* and a lepton [8].

In this thesis the study of the neutral B meson oscillations is reported using the data collected by the OPAL detector in the period of 1991 to 1993, corresponding to about 1.5 million multihadronic events. The strategy for this analysis is briefly described below. In order to tag $\mathrm{Z}^0 \rightarrow \mathrm{b}\bar{\mathrm{b}}$ decays and to determine the charge of each b quark (or $\bar{\mathrm{b}}$ quark) in a B hadron, events with two leptons (which are called *"dilepton events"*) were selected. To obtain information on the proper decay time, the secondary vertex, which is a decay point of a particle, was reconstructed and the Lorentz boost factor was estimated by measuring the energy of the jet including the lepton track. Taking into account the combinations of signs of each lepton charge, the proper time distributions for each combination were fitted simultaneously to obtain the mass differences for B_d and B_s.

The composition of this thesis is as follows; in chapter 2, the electroweak theory is briefly summarized and the motivation of physics is described by explaining the mechanism of the neutral B meson oscillation. In chapter 3, the LEP machine and the OPAL detector are reviewed. In chapter 4, the event selection criteria, the secondary vertex reconstruction and the likelihood method are described in detail and the results of this study are shown. In chapter 5, the constraint to Cabbibo-Kobayashi-Maskawa Matrix elements is calculated and the possibility of a future extension of this analysis is discussed. At last, in chapter 6, the conclusions of this report are given.

Chapter 2

Physics

2.1 Electroweak Theory

2.1.1 Overview

In this world, it is believed that there exist four types of interactions; electromagnetic interaction, weak interaction, strong interaction and gravity. The electromagnetic interaction and the gravity are very familiar in our usual life. Particles with same charge repulse each other and particles with opposite charge pull each other. This is a good example for the electromagnetic interaction. As an example of the gravity, the motion of planets can be beautifully described. On the other hand, the strong interaction and the weak interaction are not so familiar. The reason why protons and neutrons are confined in nuclei is attributed to the strong interaction. The weak interaction can be observed in the β decay of nuclei.

The present-day theory of elementary particle physics claims that the force can be transferred by exchanging an intermediate particle, which is called *Gauge Boson.* Now, four kinds of intermediate particles, γ, g, Z^0 and $W^\pm$, are known. The electromagnetic interaction is mediated by γ, which is called *photon.* Photons have no mass, so the interaction range for the electromagnetic interaction is infinity. The strong interaction is mediated by g, which is called *gluon.* The carrier of the gravitational force is *graviton*, but this boson is not experimentally observed yet.

The weak interaction is mediated by Z^0 and/or $W^\pm$. Z^0 is a neutral gauge boson and $W^\pm$ are charged gauge bosons. These masses are so heavy that the interaction range of the weak interaction is very short.

As objects affected by these interactions there are twelve types of *fermions* in this world. These can be categorized into '*quarks*' and '*leptons*'. Quarks are summarized as;

$$\begin{pmatrix} \mathrm{u} \\ \mathrm{d} \end{pmatrix} \qquad \begin{pmatrix} \mathrm{c} \\ \mathrm{s} \end{pmatrix} \qquad \begin{pmatrix} (\mathrm{t}) \\ \mathrm{b} \end{pmatrix}$$

where u, d, s, c, b and t are called *up*, *down*, *strange*, *charm*, *bottom* and *top* respectively, and a type of quark is called *flavor.* Top quarks are not discovered yet. [1] And u, c, t quarks are categorized into *up-type* quarks and d, s, b quarks are categorized into *down-type* quarks. Leptons are also summarized as;

$$\begin{pmatrix} \nu_{\mathrm{e}} \\ \mathrm{e} \end{pmatrix} \qquad \begin{pmatrix} \nu_\mu \\ \mu \end{pmatrix} \qquad \begin{pmatrix} \nu_\tau \\ \tau \end{pmatrix}$$

---

[1] CDF collaboration reported the evidence of the top quark in 1994 [9]

where e, μ and τ, which are called *electron*, *muon* and *tau* respectively, are categorized into charged leptons and ν_e, ν_μ and ν_τ, which are called *electron neutrino*, *muon neutrino* and *tau neutrino* respectively, are categorized into neutrinos (or neutral leptons). And each doublet is called *family* both for quarks and leptons.

The electroweak theory is a combined theory of the electromagnetic interaction and the weak interaction. Various tests to this theory have been performed and not a single experiment is reported which claims the failure of this theory. The justification of this theory is still being tested around the world. For example, Z^0 decays have been investigated at LEP very precisely.

2.1.2 Electroweak Theory

The weak interaction can be formalized by a current-current interaction like the electromagnetic interaction. The coupling between a fermion and a gauge boson is described by Feynman diagrams as shown in figure 2.1. The couplings for each type are written by

$$J^\mu = \bar{u}_{\mathrm{f}}\gamma^\mu(c_V^{\mathrm{f}} - c_A^{\mathrm{f}}\gamma^5)u_{\mathrm{f}} \qquad \text{for a neutral current, } \mathrm{Z}^0 \tag{2.1}$$

and

$$J^\mu = \bar{u}_{\mathrm{f}'}\frac{1}{2}\gamma^\mu(1 - \gamma^5)u_{\mathrm{f}} \qquad \text{for a charged current, } \mathrm{W}^+, \tag{2.2}$$

where γ^μ (μ=0,1,2 and 3) are γ matrices

$$\gamma^0 = \begin{pmatrix} I & 0 \\ 0 & -I \end{pmatrix}, \quad \gamma^k = \begin{pmatrix} 0 & \sigma_k \\ \sigma_k & 0 \end{pmatrix} \quad \text{for } k = 1,2,3$$

and

$$\gamma^5 = i\gamma^0\gamma^1\gamma^2\gamma^3 = \begin{pmatrix} 0 & I \\ I & 0 \end{pmatrix}.$$

σ_k ($k = 1,2,3$), called Pauli matrices, are

$$\sigma_1 = \begin{pmatrix} 0 & 1 \\ 1 & 0 \end{pmatrix}, \quad \sigma_2 = \begin{pmatrix} 0 & -i \\ i & 0 \end{pmatrix}, \quad \sigma_3 = \begin{pmatrix} 1 & 0 \\ 0 & -1 \end{pmatrix},$$

c_V^{f} is a vector coupling constant and c_A^{f} is an axial vector coupling constant. c_V^{f} and c_A^{f} can be written by $c_V^{\mathrm{f}} = T_f^3 - 2\sin^2\theta_W Q_f$ and $c_A^{\mathrm{f}} = T_f^3$ respectively, where T_f^3 is a third component of the weak isospin and Q_f is a charge of the particle. θ_W is the Weinberg angle, which is one of the unknown parameters in the standard model. The values of c_V^{f} and c_A^{f} for each fermion are listed in table 2.1.

In the neutral current (2.1), the fermion type is not changed. In the charged current (2.2), on the other hand, a third component of the weak isospin is changed within a family.

There exist, however, transitions between different quark families in the charged current. In $\mathrm{K}_\mathrm{L}^0 \to \pi^+\ell^-\bar{\nu}$ decay, for example, a strange quark in K_L^0 is converted to an up quark in the final state π^+. In order to explain the phenomenon like that, it was proposed that the eigenstates of quarks for the strong interaction were 'rotated' resulting in the eigenstates for the weak interaction. By rotating the eigenstates of down-type quarks, new sets of doublets

$$\begin{pmatrix} \mathrm{u} \\ \mathrm{d}' \end{pmatrix} \qquad \begin{pmatrix} \mathrm{c} \\ \mathrm{s}' \end{pmatrix} \tag{2.3}$$

f	Q_f	$c_V^{\rm f}$	$c_A^{\rm f}$
$\nu_{\rm e}$, ν_μ, ν_τ	0	$1/2$	$1/2$
e, μ, τ	-1	$-1/2$	$-1/2 + 2\sin^2\theta_W$
u, c, t	$2/3$	$1/2$	$1/2 - 4/3\sin^2\theta_W$
d, s, b	$-1/3$	$-1/2$	$-1/2 + 2/3\sin^2\theta_W$

Table 2.1: Summary of the values of $c_V^{\rm f}$ and $c_A^{\rm f}$.

Figure 2.1: Feynman diagrams for a coupling of a gauge boson to fermions. a) is for a neutral current (Z^0) and b) is for a charged current (W^+)

are obtained, where $\mathrm{d}' = \mathrm{d}\cos\theta_c + \mathrm{s}\sin\theta_c$ and $\mathrm{s}' = -\mathrm{d}\sin\theta_c + \mathrm{s}\cos\theta_c$. So far, only two families are considered. Using this idea the weak current in the formula (2.2) is modified to be

$$J^\mu = (\bar{\mathrm{u}}\ \bar{\mathrm{c}})\frac{1}{2}\gamma^\mu(1-\gamma^5)V\begin{pmatrix}\mathrm{d}\\ \mathrm{s}\end{pmatrix}, \tag{2.4}$$

where

$$V = \begin{pmatrix}\cos\theta_c & \sin\theta_c\\ -\sin\theta_c & \cos\theta_c\end{pmatrix}.$$

θ_c is well known as a *Cabbibo Angle* and $\sin\theta_c = 0.2205 \pm 0.0018$ [10]. This means that a transition of not only $\mathrm{s} \leftrightarrow \mathrm{u}$ describing the above mentioned K^0_L decay but also $\mathrm{c} \leftrightarrow \mathrm{d}$ happens. Based on this formalism, S. L. Glashow, I. Illiopoulos and L. Maiani predicted the existence of a charm quark [11] in 1970 to explain the non-existence of flavor changing neutral current and in 1974–1976 the heavy mesons including a charm quark(s) ($J/\psi(\mathrm{c}\bar{\mathrm{c}})$, $\mathrm{D}^+(\mathrm{c}\bar{\mathrm{u}})$ and so on) were discovered.

2.1.3 Cabbibo-Kobayashi-Maskawa Matrix

M. Kobayashi and T. Maskawa expanded this idea to three families [12]. Doublets of quarks (formula (2.3)) are changed as

$$\begin{pmatrix}\mathrm{u}\\ \mathrm{d}'\end{pmatrix} \quad \begin{pmatrix}\mathrm{c}\\ \mathrm{s}'\end{pmatrix} \quad \begin{pmatrix}\mathrm{t}\\ \mathrm{b}'\end{pmatrix}$$

and the weak current (formula (2.4)) is also modified as,

$$J^\mu = (\bar{\mathrm{u}}\ \bar{\mathrm{c}}\ \bar{\mathrm{t}})\frac{1}{2}\gamma^\mu(1-\gamma^5)V\begin{pmatrix}\mathrm{d}\\ \mathrm{s}\\ \mathrm{b}\end{pmatrix}$$

where the matrix V is known as *Cabbibo-Kobayashi-Maskawa matrix* (CKM matrix). CKM matrix has nine elements, i.e.,

$$V = \begin{pmatrix}V_{\mathrm{ud}} & V_{\mathrm{us}} & V_{\mathrm{ub}}\\ V_{\mathrm{cd}} & V_{\mathrm{cs}} & V_{\mathrm{cb}}\\ V_{\mathrm{td}} & V_{\mathrm{ts}} & V_{\mathrm{tb}}\end{pmatrix}$$

where $V_{\mathrm{td}}, V_{\mathrm{ts}}, V_{\mathrm{tb}}$ are not measured directly because a top quark is not yet discovered. But using unitarity condition, the parameters can be estimated from known parameters. These matrix elements can be parametrized using Wolfenstein parametrization [13],

$$V = \begin{pmatrix}1-\lambda^2/2 & \lambda & A\lambda^3(\rho-i\eta)\\ -\lambda & 1-\lambda^2/2 & A\lambda^2\\ A\lambda^3(1-\rho-i\eta) & -A\lambda^2 & 1\end{pmatrix} \tag{2.5}$$

λ equals to $\sin\theta_c$, and $A = 0.8 \pm 0.1$, which was determined by the measurement of V_{cb} in semileptonic B decay [14]. η is related to the imaginary part of the matrix element.

Currently, the absolute values of each matrix element are determined as follows;

$$V = \begin{pmatrix} 0.9747 \sim 0.9759 & 0.218 \sim 0.224 & 0.002 \sim 0.005 \\ 0.218 \sim 0.224 & 0.9738 \sim 0.9752 & 0.032 \sim 0.048 \\ 0.004 \sim 0.015 & 0.030 \sim 0.048 & 0.9988 \sim 0.9995 \end{pmatrix}$$

The examples for obtaining each element are briefly described below [10].

$|V_{\mathrm{ud}}|$ is measured by the precision measurement of nuclear β decays. β decays include the process $\mathrm{d}\to\mathrm{ue}\nu_{\mathrm{e}}$. Compared with muon decays, $|V_{\mathrm{ud}}|$ can be determined [15] to be $|V_{\mathrm{ud}}| = 0.9744 \pm 0.0010$.

$|V_{\mathrm{us}}|$ is measured by studying a kaon decay [16], $\mathrm{K}^+ \to \pi^0\mathrm{e}^+\nu_{\mathrm{e}}$. $\bar{\mathrm{s}}$ in K^+ decays into $\bar{\mathrm{u}}$ in π^0 via W^+ emission. By this study, $|V_{\mathrm{us}}| = 0.2196 \pm 0.0023$. On the other hand, this value can be estimated also by the study of hyperon decays. This suffers from a large theoretical uncertainty due to first order SU(3) symmetry breaking effects in the axial-vector coupling. By taking into account the result from WA2 [17], the corrected value $|V_{\mathrm{us}}| = 0.222 \pm 0.003$ is obtained. The average value of these results is $|V_{\mathrm{us}}| = 0.2205 \pm 0.0018$.

$|V_{\mathrm{cd}}|$ is measured by neutrino and antineutrino production of charm decays. By study of cross section of dimuon productions at CDHS group [18], $\bar{\mathrm{B}}_{\mathrm{c}\to\ell}|V_{\mathrm{cd}}| = (0.41 \pm 0.07) \times 10^{-2}$ is obtained, where $\bar{\mathrm{B}}_{\mathrm{c}\to\ell}$ is an average semileptonic branching ratio of charm hadrons. The value is obtained also at Tevatron Experiment [19], $\bar{\mathrm{B}}_{\mathrm{c}\to\ell}|V_{\mathrm{cd}}| = (0.534\ {}^{+0.052}_{-0.078}) \times 10^{-2}$. On average, $\bar{\mathrm{B}}_{\mathrm{c}\to\ell}|V_{\mathrm{cd}}| = (0.47 \pm 0.05) \times 10^{-2}$. $\bar{\mathrm{B}}_{\mathrm{c}\to\ell}$ can be estimated [20], weighted by a production rate of $\mathrm{D}^0/\mathrm{D}^+ = (60 \pm 10)/(40 \mp 10)$, to be 0.113 ± 0.015. Then $|V_{\mathrm{cd}}| = 0.204 \pm 0.017$ is obtained.

$|V_{\mathrm{cs}}|$ is estimated by charm meson decays, $\mathrm{D}\to \bar{\mathrm{K}}\mathrm{e}^+\nu_{\mathrm{e}}$. The decay width of this process is expressed as $\Gamma(\mathrm{D} \to \bar{\mathrm{K}}\mathrm{e}^+\nu_{\mathrm{e}}) = |\mathrm{f}_+^{\mathrm{D}}(0)|^2|\mathrm{V}_{\mathrm{cs}}|^2(1.54 \times 10^{11})\ \mathrm{sec}^{-1}$, where $f_+^{\mathrm{D}}(q^2)$ is a form factor for this process and $q = p_{\mathrm{D}} - p_{\mathrm{K}}$. p_{D} and p_{K} are a momentum for D and K mesons respectively. Taking into account the measurements of the decay width of this decay mode [21] and accurate value [22] of the lifetime of τ_{D^+} and τ_{D^0}, $\Gamma(\mathrm{D} \to \bar{\mathrm{K}}\mathrm{e}^+\nu_{\mathrm{e}}) = (0.762 \pm 0.055) \times 10^{11}\ \mathrm{psec}^{-1}$ is obtained. Therefore, this means $|f_+^{\mathrm{D}}(0)|^2|V_{\mathrm{cs}}|^2 = 0.495 \pm 0.036$. The calculation of the form factor is performed by several techniques [23, 24] and $f_+^{\mathrm{D}}(0)$ is estimated to be 0.7 ± 0.1. Then $|V_{\mathrm{cs}}| = 1.01 \pm 0.18$ is obtained.

The ratio $|V_{\mathrm{ub}}|/|V_{\mathrm{cb}}|$ is estimated by measuring the energy spectrum of leptons coming from $\mathrm{b}\to\mathrm{c}\ell\nu$ decays and $\mathrm{b}\to\mathrm{u}\ell\nu$ decays on $\Upsilon(4S)$ resonance. Both CLEO and ARGUS collaborations have reported the evidence of $\mathrm{b}\to\mathrm{u}\ell\nu$ decay [25]. These results depend on the theoretical uncertainty on the spectrum of leptons coming from b decays [24, 26]. Taking into account experimental and theoretical uncertainties, $|V_{\mathrm{ub}}|/|V_{\mathrm{cb}}| = 0.08 \pm 0.02$ is obtained.

$|V_{\mathrm{cb}}|$ is determined by the direct measurement of the decay width of the semileptonic decays of b hadrons. This decay width is written by $\Gamma(\mathrm{b} \to c\ell\bar{\nu}_\ell) = \mathrm{B}(\mathrm{b} \to c\ell\bar{\nu}_\ell)/\tau_{\mathrm{b}} = \frac{\mathrm{G}_{\mathrm{F}}^2\mathrm{m}_{\mathrm{b}}^5}{192\pi^3}\mathrm{F}(\mathrm{m}_{\mathrm{c}}/\mathrm{m}_{\mathrm{b}})|\mathrm{V}_{\mathrm{cb}}|^2$, where τ_{b} is the b lifetime and $F(m_{\mathrm{c}}/m_{\mathrm{b}})$ is a phase factor, which is about 1.5. From ARGUS and CLEO experiments [27], $|V_{\mathrm{cb}}| = 0.040 \pm 0.005$ is obtained, where $\tau_{\mathrm{b}} = (1.49 \pm 0.04)$ psec [28] is used.

The $\mathrm{B_d}$-$\bar{\mathrm{B}}_{\mathrm{d}}$ and $\mathrm{B_s}$-$\bar{\mathrm{B}}_{\mathrm{s}}$ oscillations provide information about $|V_{\mathrm{tb}}V_{\mathrm{td}}|$ and $|V_{\mathrm{tb}}V_{\mathrm{ts}}|$ respectively as will be described in section 2.2. So the study of these oscillations is essential to the check of CKM matrix elements including top quarks.

2.1.4 *CP* Violation

There exist some discrete transformations in nature which play an important role in particle physics; charge conjugation (C), parity transformation (P) and time reversal (T). The charge conjugation is an operation which reverts a sign of a charge of particle. A parity transformation is an operation which reverts spatial coordinates, $(x, y, z) \to (-x, -y, -z)$. The electromagnetic and strong interactions are invariant under these transformations. The weak interaction is, however, not invariant under each transformation: C, P. A time reversal is an operation which reverts an arrow of time, $T \to -T$. Under the CPT transformation, which performs a charge conjugation, a parity transformation and a time reversal at the same time, any interaction is invariant. This is known as *CPT Theorem.*

In the weak interaction, symmetry under a charge conjugation and a parity transformation is broken, which is illustrated in figure 2.2 by considering neutrino (anti-neutrino) helicity states. Neutrinos have a *left-handed* spin and anti-neutrinos have a *right-handed* spin. *Left-handed* means that a momentum and a spin are antiparallel (negative helicity). On the other hand, *right-handed* means that a momentum and a spin are parallel (positive helicity). A charge conjugation changes neutrino with a left-handed spin into *anti*-neutrino with a left-handed spin. And a parity transformation changes neutrino with a left-handed spin into neutrino with a *right-handed* spin. These states after transformation are not observed experimentally. But, CP transformation, simultaneous C- and P-transformation, changes neutrino with a left-handed spin into *anti*-neutrino with a *right-handed* spin, which is observed. So, it was considered that under CP transformation the symmetry was not broken.

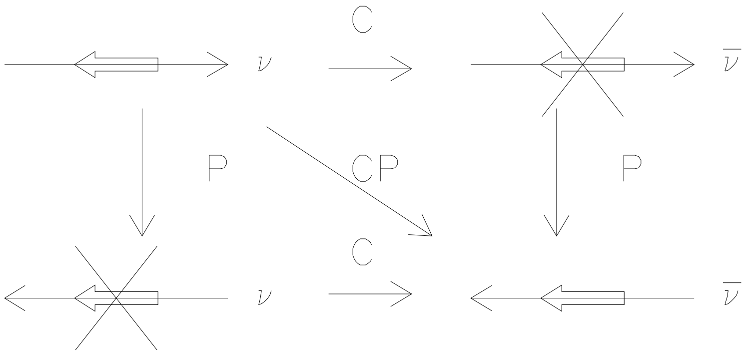

Figure 2.2: Results on neutrino spin state under C and P operations

But in 1964 CP violation was observed by discovering a specific neutral kaon decay mode, $\mathrm{K}^0_\mathrm{L} \to \pi^+\pi^-$ [29]. In the framework of the standard model, CP violation can be explained by CKM matrix formalism as follows.

Two reactions, ab → cd and cd → ab, are considered. If CP conservation is not broken, which means that T transformation is not broken due to the CPT theorem, the scattering amplitudes of these two reactions should be same.

The scattering amplitude of ab → cd, $\mathcal{M}$, is written by

$$\begin{aligned}
\mathcal{M} &\sim J_{\mathrm{ca}}{}^{\mu} J_{\mathrm{bd}}{}_{\mu}^{\dagger} \\
&= (\bar{u}_c \gamma^\mu (1-\gamma^5) V_{ca} u_a)(\bar{u}_b \gamma_\mu (1-\gamma^5) V_{bd} u_d)^\dagger \\
&= V_{ca} V_{db}^* (\bar{u}_c \gamma^\mu (1-\gamma^5) u_a)(\bar{u}_d \gamma_\mu (1-\gamma^5) u_b).
\end{aligned}$$

By C transformation, the above amplitude is modified as;

$$\mathcal{M}_C \sim V_{ca} V_{db}^* (\bar{u}_a \gamma^\mu (1+\gamma^5) u_c)(\bar{u}_b \gamma_\mu (1+\gamma^5) u_d).$$

P transformation is equal to operating γ^0 on the spinor, so by P transformation to the $/matM_C$,

$$\mathcal{M}_{CP} \sim V_{ca}V^*_{db}(\bar{u}_a\gamma^\mu(1-\gamma^5)u_c)(\bar{u}_b\gamma_\mu(1-\gamma^5)u_d). \tag{2.6}$$

This scattering amplitude $\mathcal{M}_{CP}$ corresponds to reaction cd $\rightarrow$ ab. And the original scattering amplitude of ab $\rightarrow$ cd, $\mathcal{M}$, can be written by

$$\mathcal{M} \sim V^*_{ca}V_{db}(\bar{u}_a\gamma^\mu(1-\gamma^5)u_c)(\bar{u}_b\gamma_\mu(1-\gamma^5)u_d). \tag{2.7}$$

By comparing the formula (2.6) and the formula (2.7), the relation, $\mathcal{M}_{CP} = \mathcal{M}$ can be obtained if all matrix elements are real numbers. But if some matrix elements contain an imaginary part, $\mathcal{M}_{CP} \neq \mathcal{M}$ is obtained, resulting in the broken CP invariance. Non-zero η in the CKM matrix elements implies the existence of the CP violation.

It is very important to give some constraints to CKM matrix elements. CKM matrix is an unitary matrix, $VV^\dagger = V^\dagger V = 1$. According to this relation, the following relation is obtained,

$$V_{\mathrm{ud}}V^*_{\mathrm{ub}} + V_{\mathrm{cd}}V^*_{\mathrm{cb}} + V_{\mathrm{td}}V^*_{\mathrm{tb}} = 0.$$

It is very interesting to consider this relation geometrically. The above relation forms the *unitarity triangle* in the complex plane. Using Wolfenstein parametrization these terms can be denoted as $V_{\mathrm{ud}}V^*_{\mathrm{ub}} \sim A\lambda^3(\rho + i\eta), V_{\mathrm{cd}}V^*_{\mathrm{cb}} = -A\lambda^3$ and $V_{\mathrm{td}}V^*_{\mathrm{tb}} = A\lambda^3(1-\rho-i\eta)$, where $O(\lambda^5)$ is ignored. On the complex plane, $V_{\mathrm{ud}}V^*_{\mathrm{ub}}$, $V_{\mathrm{cd}}V^*_{\mathrm{cb}}$ and $V_{\mathrm{td}}V^*_{\mathrm{tb}}$ can be written as a vector (ρ,η), $(-1,0)$ and $(1-\rho,-\eta)$ respectively, where the unit is $A\lambda^3(=\lambda V_{\mathrm{cb}})$. It can be understood that these vectors form a triangle as is shown in figure 2.3. The three angles are named α, β and γ. These are expressed as $\alpha = \arg(-V_{\mathrm{td}}V^*_{\mathrm{tb}}/V_{\mathrm{ud}}V^*_{\mathrm{ub}})$, $\beta = \arg(-V_{\mathrm{cd}}V^*_{\mathrm{cb}}/V_{\mathrm{td}}V^*_{\mathrm{tb}})$ and $\gamma = \arg(-V_{\mathrm{ud}}V^*_{\mathrm{ub}}/V_{\mathrm{cd}}V^*_{\mathrm{cb}})$.

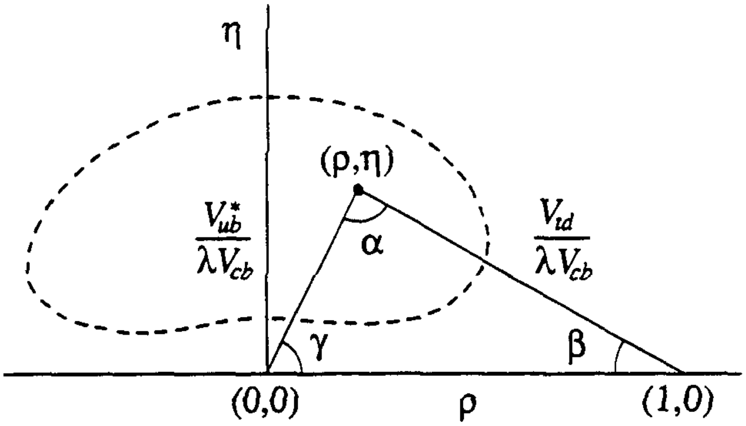

Figure 2.3: The unitarity triangle in the (ρ,η) plane. This triangle is normalized by $\lambda V_{\mathrm{cb}}(= A\lambda^3)$. The current uncertainty on the (ρ,η) is shown by dashed curve at 95% C.L.

2.2 B^0-$\bar{\mathrm{B}}^0$ Mixing

The electroweak theory predicts the existence of B^0-$\bar{\mathrm{B}}^0$ mixing as well as K^0-$\bar{\mathrm{K}}^0$ and D^0-$\bar{\mathrm{D}}^0$ mixings. This mixing phenomenon implies that the particle (antiparticle) translates into its antiparticle (particle) before it decays. This phenomenon can be explained by the second order box diagram via two W bosons exchange as shown in figure 2.4 for the case of B^0-$\bar{\mathrm{B}}^0$ mixing.

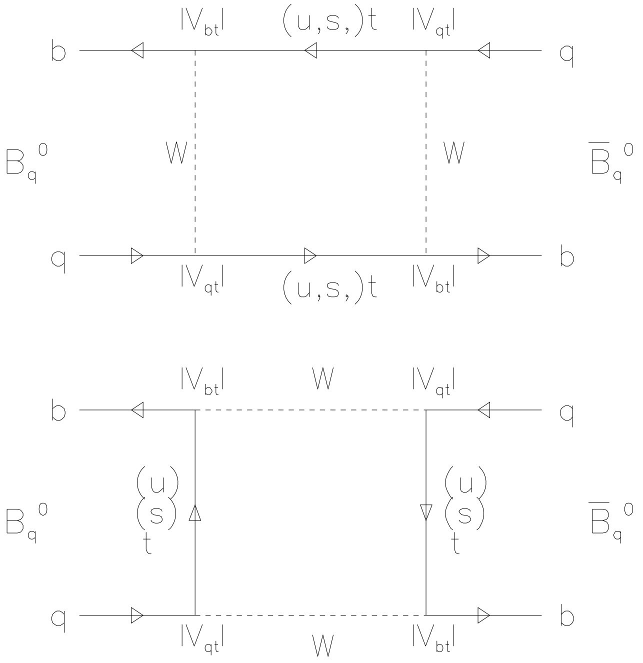

Figure 2.4: Feynman diagrams for B^0-$\bar{\mathrm{B}}^0$ mixing

In the analogy to the K^0 case, the mass eigenstates $|m_{1,2}\rangle$ of B meson can be written as follows;

$$\begin{aligned} |m_1\rangle &= \frac{1}{\sqrt{2}}(|\mathrm{B}^0\rangle + |\bar{\mathrm{B}}^0\rangle) \\ |m_2\rangle &= \frac{1}{\sqrt{2}}(|\mathrm{B}^0\rangle - |\bar{\mathrm{B}}^0\rangle). \end{aligned}$$

The effect of CP violation is neglected. Suppose B^0 is generated at time $t = 0$. The probability that B^0 is observed as B^0 after a time t, $Prob(\mathrm{B}^0 \to \mathrm{B}^0)$, is written by

$$\begin{aligned} Prob(\mathrm{B}^0 \to \mathrm{B}^0) \;\propto\; & \frac{1}{4}(\exp(-\Gamma_1 t) + \exp(-\Gamma_2 t) \\ & + \exp(-\frac{1}{2}(\Gamma_1 + \Gamma_2)t)\exp(-i(m_1 - m_2)t) \\ & + \exp(-\frac{1}{2}(\Gamma_1 + \Gamma_2)t)\exp(i(m_1 - m_2)t)) \end{aligned}$$

Now, supposing $\Gamma_1 = \Gamma_2 = 1/\tau$, where τ is the lifetime of a B meson, the above formula is modified as follows;

$$Prob(\mathrm{B}^0 \to \mathrm{B}^0) \propto \frac{1}{4}\mathrm{e}^{-\mathrm{t}/\tau}(2 + \exp(i(\mathrm{m}_1 - \mathrm{m}_2)\mathrm{t})) + \exp(-i(\mathrm{m}_1 - \mathrm{m}_2)\mathrm{t}))).$$

Using $\Delta m = m_1 - m_2$, the normalized probability is;

$$Prob(\mathrm{B}^0 \to \mathrm{B}^0) = \frac{1}{\tau}\mathrm{e}^{-\mathrm{t}/\tau}\cos^2(\frac{\Delta \mathrm{m}}{2}\mathrm{t}).$$

Similarly, the probability that B^0 generated at $t = 0$ is observed as $\bar{\mathrm{B}}^0$ after a time t, $Prob(\mathrm{B}^0 \to \bar{\mathrm{B}}^0)$, is written by

$$Prob(\mathrm{B}^0 \to \bar{\mathrm{B}}^0) = \frac{1}{\tau}\mathrm{e}^{-\mathrm{t}/\tau}\sin^2(\frac{\Delta \mathrm{m}}{2}\mathrm{t}).$$

The sum of these probabilities is normalized to be unity after the integration over t. These probabilities depend not on only the proper time of B meson but also on a mass difference of a neutral B meson, Δm. If $\Delta m = 0$, B^0 generated at $t = 0$ is observed as B^0 necessarily. But if Δm is not zero, the oscillation of B meson takes place and B^0 might be observed as a $\bar{\mathrm{B}}^0$ due to the B^0-$\bar{\mathrm{B}}^0$ mixing. In other word, this variable, Δm, is a basic parameter which describes the magnitude of the neutral B meson oscillation.

The Standard Model predicts the mass difference to be about 0.5 psec^{-1} for $\mathrm{B_d}$ and to be more than 10 psec^{-1} for $\mathrm{B_s}$, implying quite a rapid oscillation for $\mathrm{B_s}$.

When the mixing parameter, x, is defined as

$$x = \Delta m \tau,$$

each probability is written by

$$\begin{aligned} Prob(\mathrm{B}^0 \to \mathrm{B}^0) &= \frac{1}{\tau}e^{-t/\tau}\cos^2(\frac{x}{2}\frac{t}{\tau}) \\ Prob(\mathrm{B}^0 \to \bar{\mathrm{B}}^0) &= \frac{1}{\tau}e^{-t/\tau}\sin^2(\frac{x}{2}\frac{t}{\tau}). \end{aligned}$$

In figure 2.5, the probability of B^0 and $\bar{\mathrm{B}}^0$ are shown as a function of time. For each figure, the dashed line is for $Prob(\mathrm{B}^0 \to \mathrm{B}^0)$ and the dotted line is for $Prob(\mathrm{B}^0 \to \bar{\mathrm{B}}^0)$. The solid line is a sum of two probabilities. In the case of $x = 0.5$, the frequency of the B^0-$\bar{\mathrm{B}}^0$ mixing is relatively small, and it is easy to observe the oscillation of a neutral meson. But, in the case of the large x, for example $x = 10.0$, the frequency of the mixing becomes large, then it is difficult to observe the oscillation if the time resolution at the short proper time region is not so good.

The 'integrated' mixing parameter, χ, is defined as

$$\chi = \frac{\Gamma(\mathrm{b} \to \bar{\mathrm{b}} \to \ell^+)}{\Gamma(\mathrm{b} \to \ell^-) + \Gamma(\mathrm{b} \to \bar{\mathrm{b}} \to \ell^+)},$$

where $\Gamma(\mathrm{b} \to \ell^-)$ is the decay width of the semileptonic decays of b quarks and $\Gamma(\mathrm{b} \to \bar{\mathrm{b}} \to \ell^+)$ is the decay width of the semileptonic decays in the case of B^0-$\bar{\mathrm{B}}^0$ mixing.

$\Gamma(\mathrm{b} \to \bar{\mathrm{b}} \to \ell^+)$ and $\Gamma(\mathrm{b} \to \ell^-) + \Gamma(\mathrm{b} \to \bar{\mathrm{b}} \to \ell^+)$ are written respectively by using x as follows,

$$\begin{aligned} \Gamma(\mathrm{b} \to \bar{\mathrm{b}} \to \ell^+) &= \frac{1}{2\tau}(\frac{x^2}{1+x^2}) \\ \Gamma(\mathrm{b} \to \bar{\mathrm{b}} \to \ell^+) + \Gamma(\mathrm{b} \to \ell^-) &= \frac{1}{\tau}. \end{aligned}$$

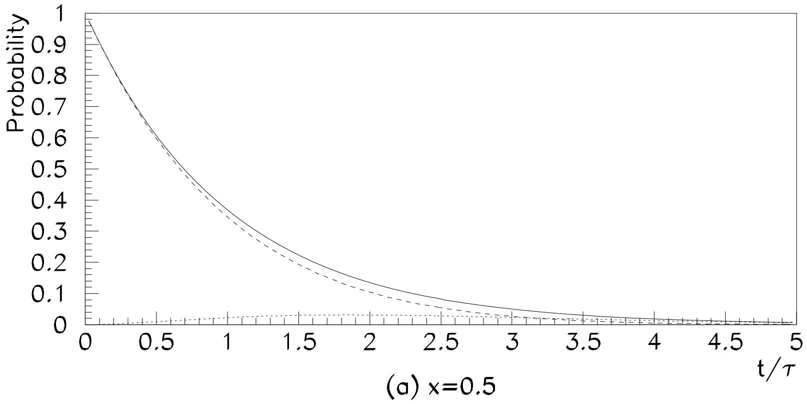

(a) x=0.5

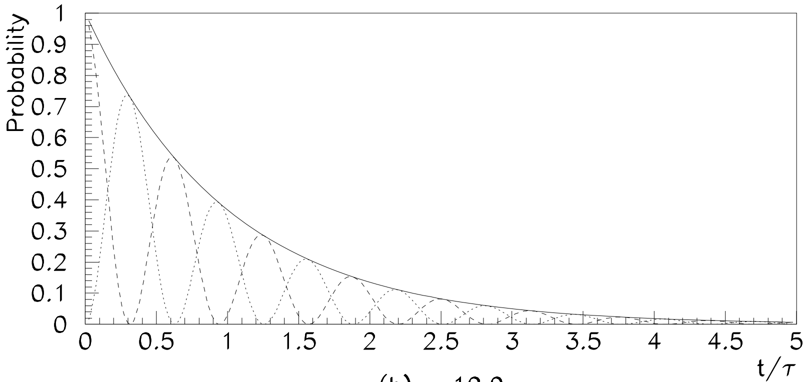

(b) x=10.0

Figure 2.5: $Prob(\mathrm{B}^0 \rightarrow \mathrm{B}^0)$ and $Prob(\mathrm{B}^0 \rightarrow \bar{\mathrm{B}}^0)$ as a function of time. The top figure (a) is for $x = 0.5$ and the bottom figure (b) is for $x = 10.0$. For each figure, the dashed line is for $Prob(\mathrm{B}^0 \rightarrow \mathrm{B}^0)$ and the dotted line is for $Prob(\mathrm{B}^0 \rightarrow \bar{\mathrm{B}}^0)$.

So, the integrated mixing parameter, χ, is obtained as

$$\chi = \frac{1}{2}\frac{x^2}{1+x^2}$$

When x is very large (greater than about 5.0), χ is close to 0.5, so this case is called the 'full mixing' which means that the mixing of a neutral B meson occurs as soon as B meson is generated. For example, $\mathrm{B_s}$-$\bar{\mathrm{B}}_\mathrm{s}$ mixing corresponds to this case as described above.

The average mixing parameter, $\bar{\chi}$, is written by

$$\bar{\chi} = f_d\chi_d + f_s\chi_s$$

as a function of two integrated mixing parameters, χ_d for $\mathrm{B_d}$ and χ_s for $\mathrm{B_s}$, where f_d and f_s are the fraction of the $\mathrm{B_d}$ and $\mathrm{B_s}$ production in a hadronization process of b quarks. The current experimental results of χ_d and $\bar{\chi}$ are summarized in table 2.2, figure 2.6 and table 2.3, figure 2.7 respectively.

	Type	χ_d	Ref.
ARGUS	$\mathrm{D}^{*-}\ell^+\ell^+$	$0.188 \pm 0.078 \pm 0.023$	[31]
ARGUS	$\ell^+\ell^+$	$0.185 \pm 0.040 \pm 0.049$	[31]
ARGUS	$\ell^+\ell^+\pi^-$	$0.162 \pm 0.043 \pm 0.038$	[32]
CLEO	$\ell^+\ell^+$	$0.152 \pm 0.037 \pm 0.040$	[33]
CLEO	$\ell^+\ell^+$	$0.167 \pm 0.017 \pm 0.024$	[34]
CLEO	$\ell^+\ell^+\pi^-$	$0.153 \pm 0.024 \pm 0.021$	[34]

Table 2.2: Summary of the results of χ_d measurements.

	Type	$\bar{\chi}$	Ref.
ALEPH	Jet charge (Q_{jet}) ℓ^+	$0.113 \pm 0.018 \pm 0.027$	[35]
DELPHI	Jet charge (Q_{jet}) ℓ^+	$0.144 \pm 0.014 \;^{+0.017}_{-0.011}$	[36]
DELPHI	$\Lambda\ell^+$	$0.129 \;^{+0.075}_{-0.065} \pm 0.044$	[37]
DELPHI	$\ell^+\ell^+$	$0.121 \pm 0.016 \pm 0.006$	[37]
L3	$\ell^+\ell^+$	$0.125 \pm 0.011 \pm 0.008$	[38]
OPAL	$\ell^+\ell^+$	$0.143 \;^{+0.022}_{-0.021} \pm 0.007$	[39]
UA1	$\ell^+\ell^+$	$0.148 \pm 0.029 \pm 0.017$	[40]
CDF	$\ell^+\ell^+$	$0.176 \pm 0.031 \pm 0.032$	[41]

Table 2.3: Summary of the results of $\bar{\chi}$ measurements.

The mass difference Δm_q is described as

$$\Delta m_q = \frac{G_F^2}{6\pi^2} m_t^2 B_B f_B^2 M_{\mathrm{B_q}} |V_{\mathrm{tq}}V_{\mathrm{tb}}^*|^2 \frac{A(z_t)}{z_t}\eta_{QCD} \qquad q = \mathrm{d\ or\ s},$$

where G_F is a Fermi coupling constant, f_B is a decay constant and m_t and $M_{\mathrm{B_q}}$ are the top quark mass and $\mathrm{B_q}$ mass, respectively [30]. $A(z_t)$ is a function of $z_t = m_t^2/M_W^2$, where M_W is a

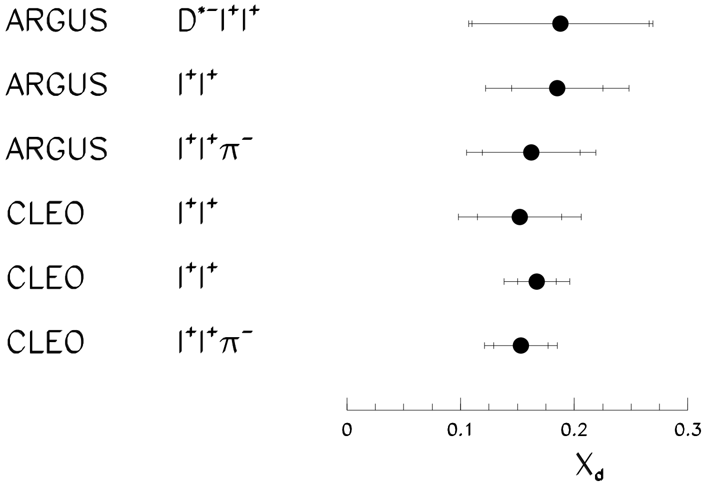

Figure 2.6: Summary of the results of χ_d measurements.

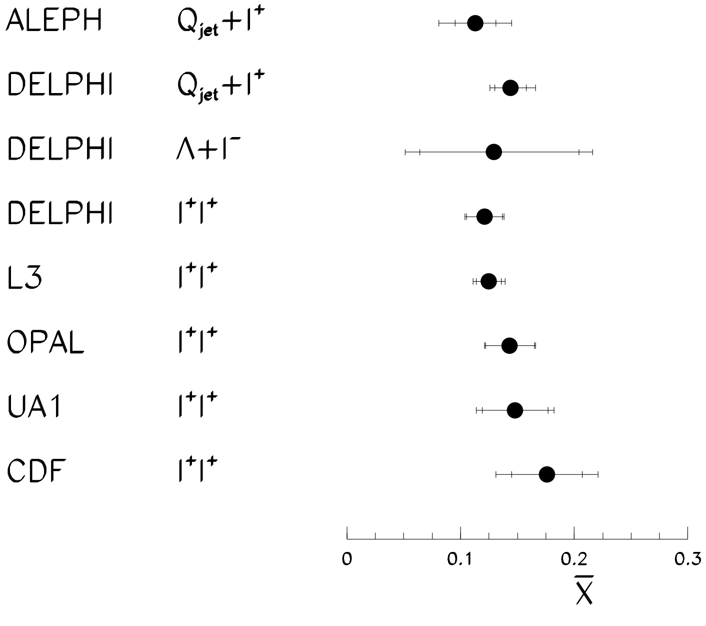

Figure 2.7: Summary of the results of $\bar{\chi}$ measurements.

mass of W boson. B_B is called 'Bag factor' and is constant. Due to a poor knowledge on $B_B f_B^2$, it is difficult to obtain information on the CKM matrix elements by only Δm_d or Δm_s. If the ratio $\Delta m_s/\Delta m_d$ is taken, various unknown factors are canceled and the following relation is obtained;

$$\frac{\Delta m_s}{\Delta m_d} \sim |V_{\mathrm{ts}}/V_{\mathrm{td}}|^2.$$

In other words, information on the CKM matrix elements can be obtained from $\Delta m_s/\Delta m_d$. According to the prediction from the Standard Model, $|V_{\mathrm{ts}}|$ is much larger than $|V_{\mathrm{td}}|$. This means that the mass difference of $\mathrm{B_s}$ is much larger than the mass difference of $\mathrm{B_d}$.

Chapter 3

Experimental Apparatus

3.1 Accelerator

The European laboratory for high energy physics, CERN (**C**onceil **E**uropéen pour la **R**echerche **N**ucléaire), was built in a suburbs of Geneva, Switzerland in 1954 and many important results, like discoveries of Z^0 and $W^\pm$ bosons by UA1 experiment, have been reported.

In 1986, a circular electron-positron collider was built to investigate the electroweak theory more precisely. This collider is called LEP (**L**arge **E**lectron **P**ositron collider) with a circumference of about 27 km across the border between Switzerland and France. The maximum beam energy of electrons (positrons) is designed to be about 100 GeV corresponding to the center-of-mass energy $\sqrt{s} \sim 200$ GeV. This collider is the largest in the world and is believed to be 'the last circular electron-positron collider'. In 1989, LEP started to run and the first $Z^0 \rightarrow q\bar{q}$ events was observed by the OPAL detector.

The cross section of e^+e^- annihilation due to a photon exchange becomes smaller as a function of the center-of-mass energy. But the resonant cross section of Z^0 production is very large at $\sqrt{s} \sim Z^0$ mass as shown in figure 3.1. So far, LEP energy is on or near the Z^0 mass to investigate the Z^0 boson decays. Many Z^0 bosons are generated everyday and new results on the Z^0 decays continue to be published. Therefore, the LEP can be called a machine for 'Z factory'.

LEP consists of four accelerators; one linear accelerator (linac) with a gun for electron and positron beams, two circular accelerators as a dumping ring and LEP main accelerator. The schematic layout of LEP is shown in figure 3.2.

At first, electrons are generated at the end point of the high-current electron linac and are accelerated by the electrostatistic field up to 200 MeV. Positrons are generated by the electron-positron converter which converts some of these accelerated electrons into positrons. The converter is the tungsten target with a thickness of two radiation lengths ($2X_0$= 7 mm). Electrons and positrons are focused and accelerated up to 600 MeV by a lower-current linac. Accelerated particles are injected into the electron-positron accumulating ring (EPA) and stored in this ring. The role of this ring is generating bunches for electrons and positrons with a high intensity and a constant energy. The high intense bunches with 600 MeV are transferred to the circular accelerator which is called 'Proton Synchrotron (PS)'.

The particles injected from EPA into PS are accelerated up to 3.5 GeV and subsequently injected into the second circular accelerator, 'Super Proton Synchrotron (SPS). Particles are still further accelerated up to 20 GeV in this ring.

Particles accelerated up to 20 GeV are injected into the main ring of LEP and finally

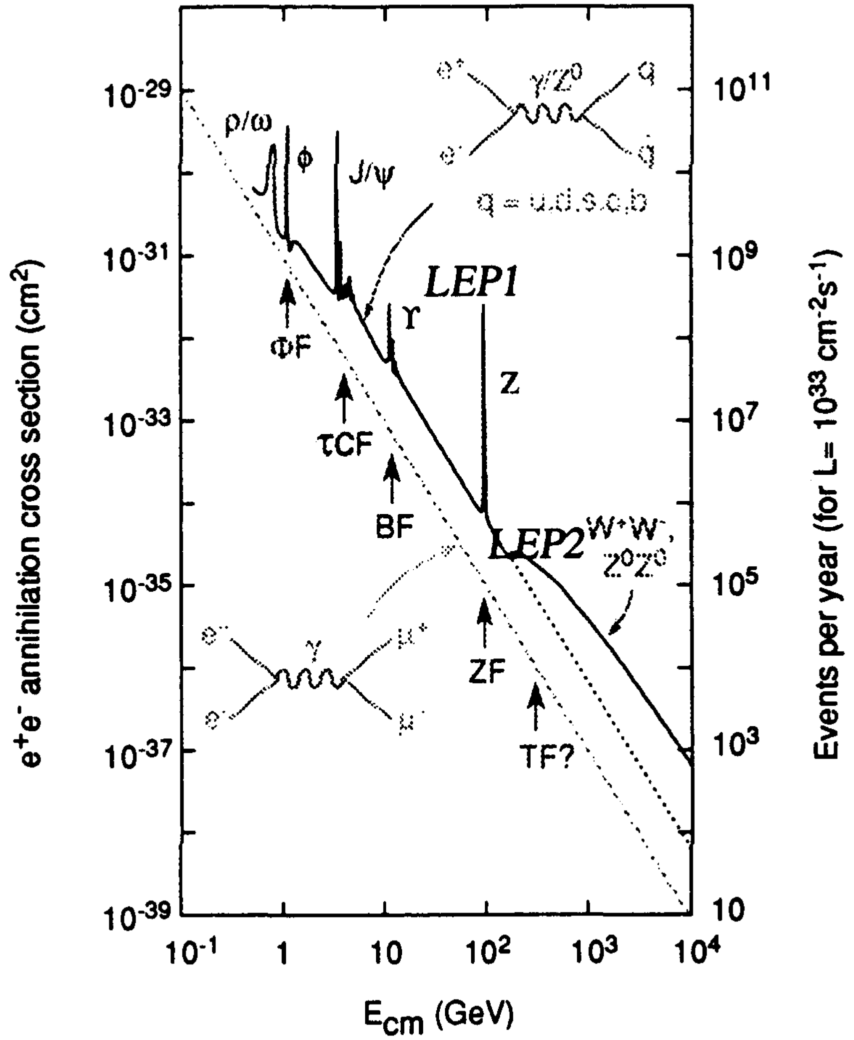

Figure 3.1: The cross section of e^+e^- annihilation as a function of center-of-mass energy.

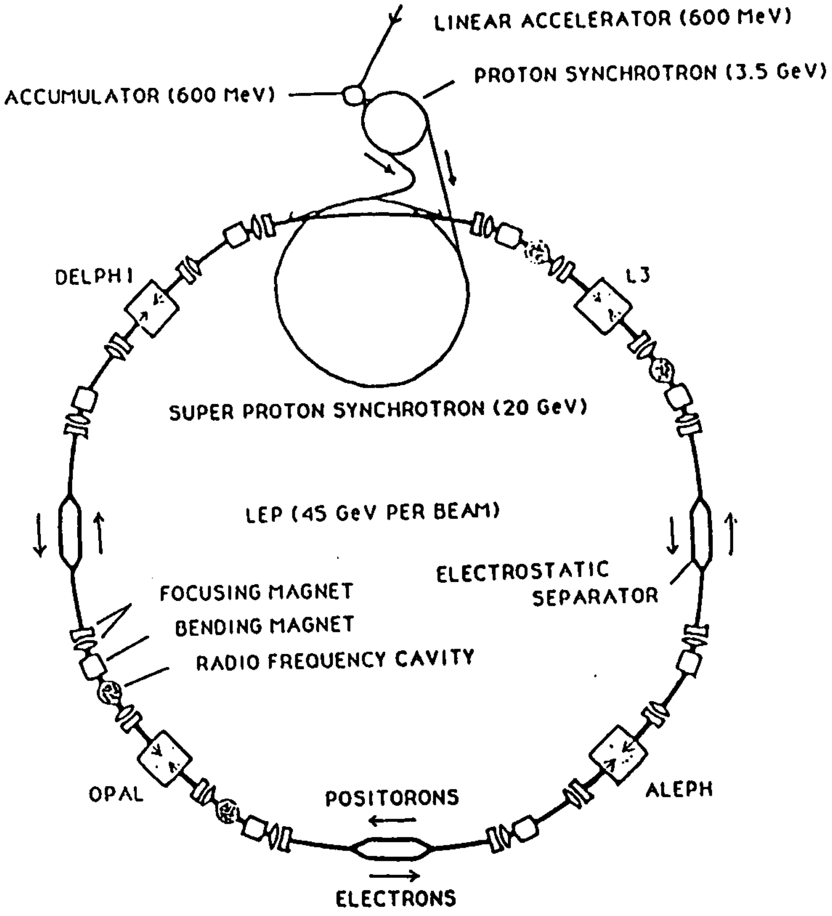

Figure 3.2: The schematic layout of LEP

accelerated up to about half of Z^0 mass (approximately 45.6 GeV). Bunches are focused by the collimeters at both sides of each detector and the electron and positron bunches collide at the center of each detector.

In table 3.1, general parameters of LEP in 1993 are listed [42].

Circumference	C	26658.87	m
Average bending radius	ρ	3026.4	m
No. of experimental collision points		4	
No. of bunches per beam	k_b	4 or 8	
No. of normal bending magnets		1104	
No. of quadrupoles		864	
No. of sextupoles		520	
No. of wigglers		20	
No. of electrostatic separators		43	
No. of 5- or 4-cell RF cavity units		140	
Phase advance per arc cell	μ_x, μ_y	90°,60°	
Betatron tunes	Q_x, Q_y	90.27,76.19	
Momentum compaction	α_c	1.856	$\times 10^{-4}$
Injection energy	E	20	GeV
($J_x = 1$, without/with wigglers)			
Twiss functions at even IP	β_x^*, β_y^*	2.5,0.21	m
Synchrotron radiation lass per turn	U_0	4.61/13.8	MeV
Transverse damping time	τ_x	772/270	msec
Natural horizontal emittance	ϵ_x	2.2/2.4	nm
Fractional energy spread	σ_E	0.31/1.74	$\times 10^{-3}$
Natural bunch length	σ_z	0.35/1.95	cm
Nominal energy for collisions	E	45.6	GeV
($J_x = 1$, no wigglers)			
Synchrotron radiation loss per turn	U_0	124.6	MeV
Transverse damping time	τ_x	65	msec
Natural horizontal emittance	ϵ_x	11.9	nm
Fractional energy spread	σ_E	7.01	$\times 10^{-3}$
Twiss functions at even IP	β_x^*, β_y^*	1.25,0.05	m
RF voltage	V_{RF}	266	MV
Synchrotron turn	Q_s	0.07	

Table 3.1: The parameters of LEP machine in 1993. For an injection energy, two sets of parameters are given. One is for the bare machine and the other is for one with the 4 damping and 12 polarization wigglers excited.

The LEP beam energy is calibrated by the resonant depolarization technique [43]. The LEP beam is naturally polarized vertically. By giving horizontal magnetic fields with one frequency, LEP beam can be depolarized due to the precession of a spin of electrons. This frequency, ν, is related with the beam energy, E; i.e, $\nu = E(\mathrm{MeV})/440.6486(1)(\mathrm{MeV})$. The accuracy of the energy calibration is estimated to be less than 1.1 MeV on the Z^0 pole.

LEP has eight straight sections where the electron and positron bunches can be collided.

ALEPH, DELPHI, L3 and OPAL detectors are installed at four sections of them and each bunch is separated not to collide at other sections. At present, four experimental groups continue to take data from 1989 and a large number of Z^0 events are collected using each detector.

3.2 The OPAL Detector

3.2.1 Overview of the OPAL detector

The OPAL (**O**mni **P**urpose **A**pparatus for **L**EP) detector [44, 45] is one of the detectors for the LEP experiments. The concept of the design of the OPAL detector is to collect all the Z^0 decay events with a high efficiency. To achieve this aim, the detector is designed to have a good uniformity and an excellent stability with well-established techniques. This detector mainly consists of four parts;

- Tracking detector to measure the momentum of a particle
- Calorimeter to measure the energy of a particle
- Muon chamber to detect muons
- Luminosity monitor to get information on the machine luminosity

The tracking detector consists of four subdetectors, which are the silicon microvertex detector, the central vertex detector, the central jet chamber and the z-chamber, and supplies information on momenta and ionization losses of the charged tracks. These tracking detectors are put in the pressure vessel filled with the common mixed gas to keep the pressure of 4 bars. In particular, information on the ionization loss is used for particle identification. The silicon microvertex detector was installed during the shutdown between 1990 and 1991 and the decay lengths of long-lived heavy hadrons can be measured very precisely. This contributes to the studies of heavy flavor physics. The calorimeter system is divided into two parts; one is the electromagnetic calorimeter and the other is the hadron calorimeter. The electromagnetic calorimeter with the presampler measures energies of particles such as electrons (positrons) and photons. Measuring energies of these particles is very important to get information on the multihadronic decays of Z^0, searches for the new particles and so on. And the hadron calorimeter measures energies of hadrons such as pions and kaons, and serves as the absorber for muon identification. The muon chamber system provides information on the tagging of the muons produced by Z^0 decays. The luminosity monitor system contributes to the measurement of an absolute machine luminosity. In particular, the silicon-tungsten luminosity monitor is installed during the shutdown between 1991 and 1992 and the measurement of the luminosity is improved very much. This improvement contributes to the precise measurement of the Z^0 line shape, and various information on the Z^0 boson can be obtained with an accuracy of less than 1%.

Three dimensional schematic view of the OPAL detector is shown in figure 3.3 and the quarter cross sections in the r-ϕ plane and the r-z plane are shown in figure 3.4. The tracking system, electromagnetic calorimeter system, hadron calorimeter system and the muon chamber system are installed in order from the center of the detector toward the outside. The luminosity monitoring system is installed surrounding the beam pipe at both sides of the detector. The solid angle of nearly 4π is covered for particle detection.

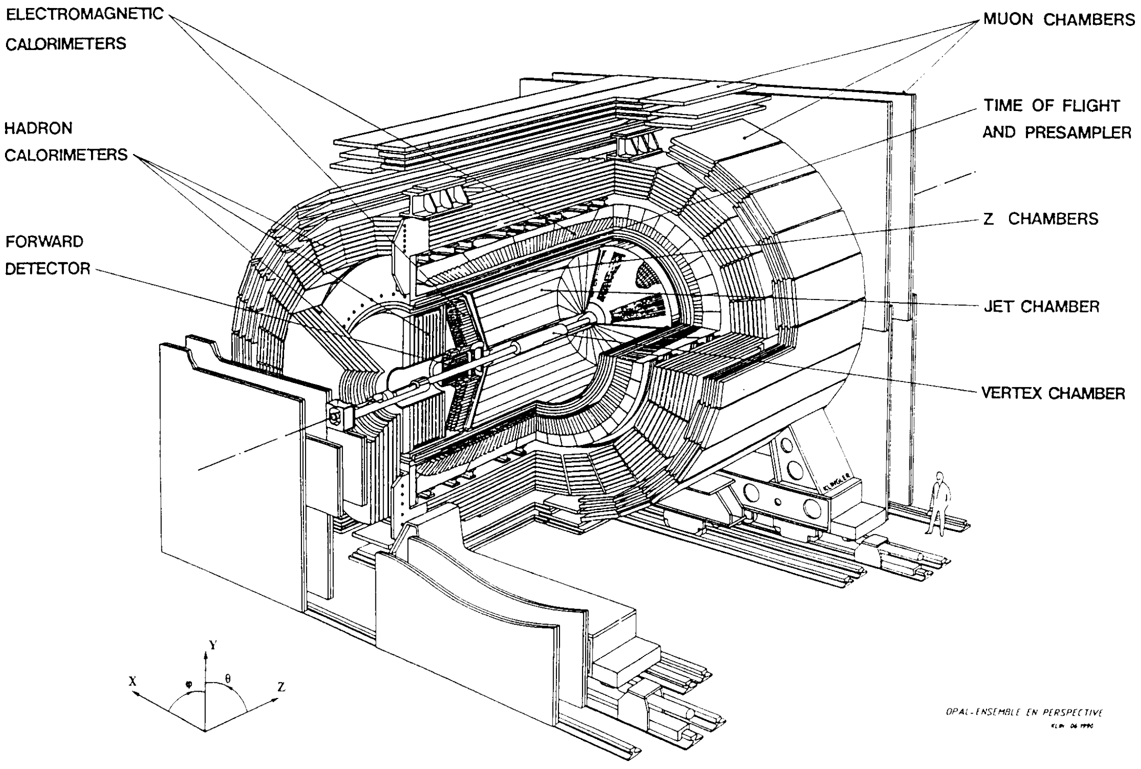

Figure 3.3: The three dimensional schematic view of the OPAL detector

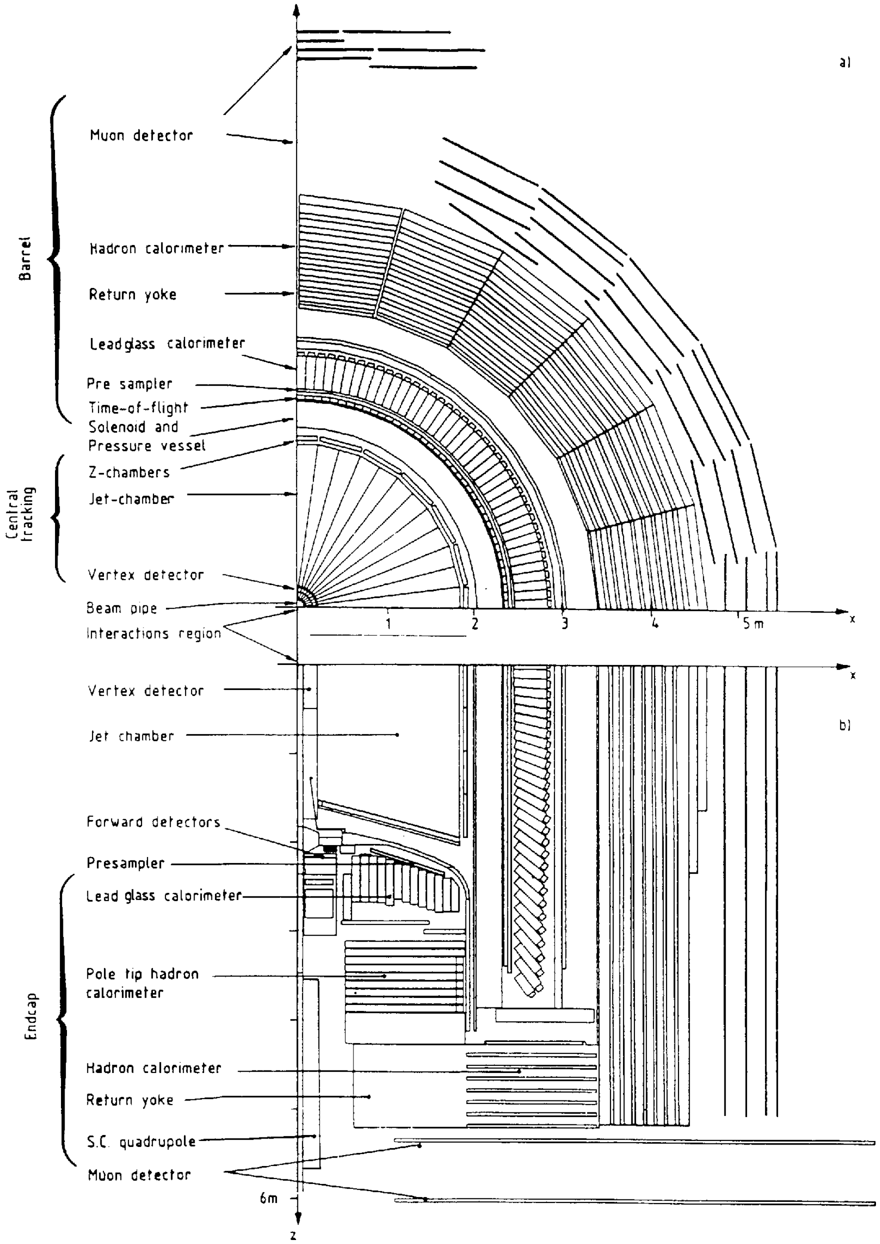

Figure 3.4: The quarter cross section of the OPAL detector in the r-ϕ plane (a) and the r-z plane (b). (N.B. The silicon tungsten luminosity monitor is not drawn in this figure.)

The solenoidal magnet supplies a uniform magnetic field of 0.435 T. Inside this coil, the tracking system is installed and this coil is surrounded by time-of-flight counters to get trigger signals rapidly and to reject cosmic ray backgrounds efficiently. Unfortunately, most of particles like electrons (positrons) and photons start to develop the electromagnetic shower before entering the calorimeter because the coil has a large material of about two radiation lengths. The presampler is installed just in front of the calorimeter to improve the energy and the spatial resolutions of the incident particles.

A sizable heat is emitted from the magnet and the electronics attached to the detector. If the heat can not be removed efficiently, the detector system would be damaged due to the high temperature. To remove the heat emitted from the magnet and electronics, the cooling water is flowed and the temperature of the cooling water is kept about 15°. In the rooms in which the data-taking electronics are installed, cold and dry air is flowed and not only the temperature is kept below about 25° but also the humidity is kept low.

The whole detector is located underground of about 100 m to reduce the backgrounds mainly due to cosmic ray muons. At present, most of the OPAL control systems are situated at the side of the OPAL detector. But the gas mixing systems are on the ground to be safely controlled and the mixed gas is transferred to the detector.

The coordinate system in the OPAL detector is defined as follows. The z axis is parallel to the beam axis and the direction of this axis is the same as that of electron beam. The x axis is defined to be the horizontal direction and the y axis is defined as the vertical direction toward the top. This coordinate system is also shown in figure 3.3. The polar angle, θ, is defined as the angle from the z axis and the azimuth angle, ϕ, is defined as the angle from the x axis toward the y axis.

In table 3.2, subdetectors consisting the OPAL detector are summarized. The descriptions for each subdetector, including the magnet and the beam pipe, are given below in more detail.

3.2.2 Magnet and Beam Pipe

The magnet installed in the OPAL detector is a cylindrical solenoidal magnet. Its mean diameter is 4.36 m and the maximum current is 7000 A. This magnet supplies the magnetic field of 0.435 T with an uniformity within $\pm 0.5\%$ in the fiducial volume along the beam pipe. Charged particles are bent in the central tracking chamber by this magnetic field. For example, the bending radius of particles with a momentum of 45 GeV/c is $\rho = 45/(0.3 \times 0.435) \sim 345$ (m). The heat is emitted from the magnet due to the resistance of the coil. In order to cool the magnet, the cooling water flows at a rate of 40 ℓ/sec and the temperature of the coil is kept constant. The magnet should be as thin as possible so that the particles could pass through the coil with less interactions. A thickness of the coil is about 150 mm corresponding to about 2 radiation lengths ($\sim 2X_0$). In table 3.3, parameters on the magnet are summarized.

The leakage of the magnet field from the coil is about 0.002 T and this effect to the subdetectors outside the magnet is negligible.

At the start of the experiment, the beam pipe made of carbon fibers with a thickness of 0.13 cm was installed at a radius of 7.8 cm. During the shutdown between 1990 and 1991, this beam pipe was replaced by the beryllium beam pipe to install the silicon microvertex detector. The radius of the beryllium beam pipe is 5.35 cm and the thickness is 0.11 cm corresponding to $\sim$0.003 radiation lengths ($\sim 0.003X_0$).

	Subdetector	Type	Channels
Central tracking system	Microvertex detector	silicon microstrips	15725
	Vertex chamber	drift chamber	648
	Jet chamber	drift chamber	7680
	Z-chamber	drift chamber	2304
Time-of-flight	Time-of-flight counter	scintillator	320
Electromagnetic calorimeter	Barrel calorimeter	lead glass calorimeter	9440
	Barrel presampler	limited streamer tube	21504
	Endcap calorimeter	lead glass calorimeter	22504
	Endcap presampler	thin, saturated gain wire chamber	6080
Hadron calorimeter	Tower (Barrel,Endcap)	limited streamer tubes	1696
	Strip (Barrel,Endcap)		56146
	Tower (Poletip)	thin, saturated gain wire chamber	336
	Strip (Poletip)		10240
Muon detector	Barrel	drift chamber	1320
	Endcap	limited streamer tube	42496
Luminosity monitor	Forward detector	proportional streamer tube (Tube chamber)	768
		drift chamber (Drift chamber)	192
		calorimeter and scintillator (other components)	216
	Silicon tungsten luminosity monitor	silicon microstrips	38912

Table 3.2: The summary of the subdetectors in the OPAL detector.

Central field	0.435 T
Mean coil diameter	4.36 m
Distance between pole faces	6.3 m
Solenoid thickness	96 mm of Al + 54 mm of glass-epoxy ($\sim$1.7 radiation lengths, including pressure vessel)
Maximum current	7000 A
Maximum power	5 MW
Cooling water flow	40 ℓ/sec
Pressure drop	15 bar
Barrel iron thickness	0.8 – 1.0 m
Coil weight	25 t
Overall magnet weight	2800 t

Table 3.3: The parameters of the magnet

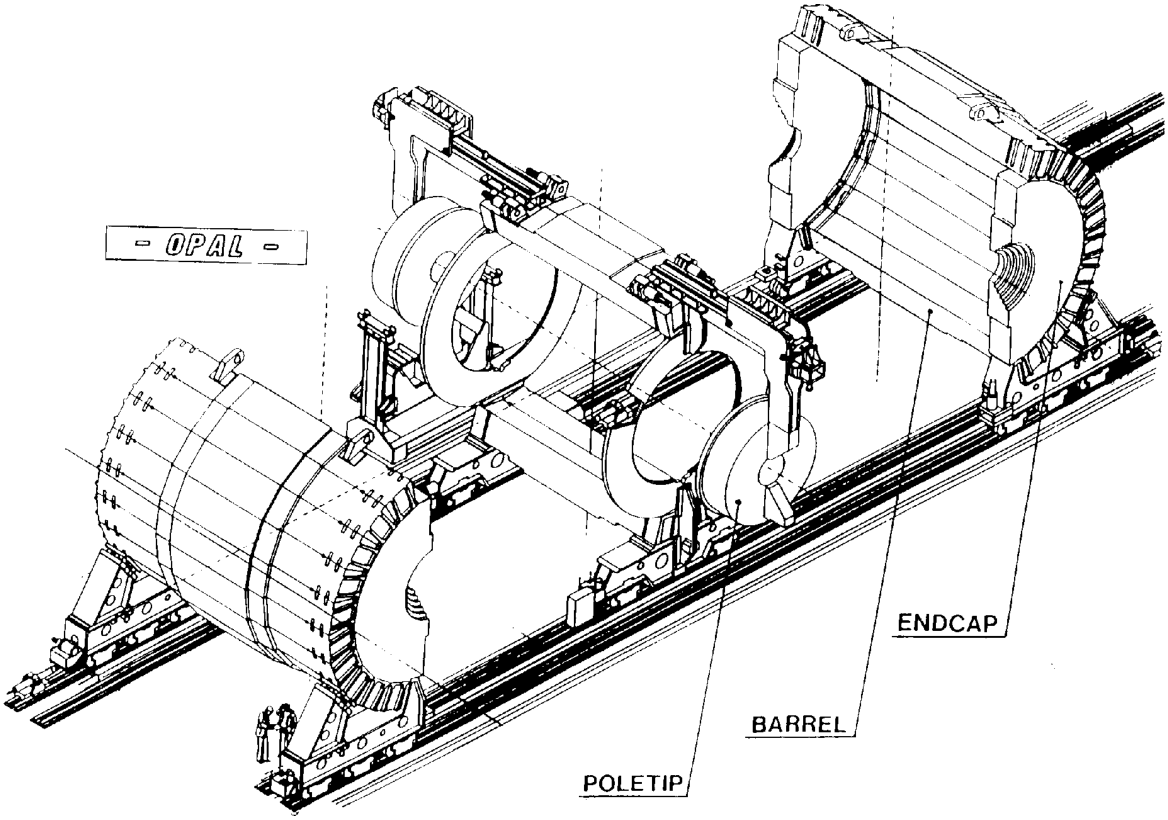

Figure 3.5: The view of the OPAL detector in open position

3.2.3 Tracking System

OPAL tracking system consists of four subdetectors, the silicon microvertex detector, the central vertex detector, the central jet chamber and the z-chamber. These subdetectors except for the silicon microvertex detector are so-called gas chambers and the same mixed gas is used. The components of the mixed gas are argon (88.2%), methane (9.8%) and isobutane (2.0%). And these gas chambers are located in the pressure vessel under the pressure of 4 bar. The design of the vertex detector is basically the same as that of the jet chamber. The silicon microvertex detector was installed during shutdown between 1990 and 1991 as described before. Tracking system provides useful information like the momentum and the ionization loss of charged particles and the decay length of heavy flavored hadrons.

a) Silicon Microvertex Detector

The silicon microvertex detector was installed and began taking data in June 1991 in order to improve the spatial resolution on the measurement of the decay point, which is called "secondary vertex", of the long-lived particles like b-flavored hadrons, τ leptons and some hypothetical new particles. First, this subdetector was the single-sided silicon detector, i.e., information only on the ϕ coordinate was provided. In March 1993, this subdetector was upgraded. The double-sided silicon detector, which is made by gluing the single-sided silicon detectors back-to-back, was adopted and not only ϕ coordinate but also z coordinate could be measured.

This silicon microvertex detector consists of two layers of silicon strip detectors. The schematic view of this detector is shown in figure 3.6 and the cross sectional view perpendicular to the beam pipe is shown in figure 3.7. The inner and the outer layers are located at the radius of 6.1 cm and 7.5 cm respectively, and these layers are put on between the beam pipe and the central vertex chamber. The coverage of this subdetector is $|\cos\theta| < 0.83$ for the inner layer and $|\cos\theta| < 0.77$ for the outer layer. The inner layer has 11 ladders and the outer layer has 14 ladders. The ladder in one layer is not overlapped each other. There is a gap between adjacent ladders. Then the ϕ acceptance is 88% for the inner layer and 91% for the outer layer. But a gap in the inner layer and a gap in the outer layer do not coincide so that there is no inefficient region in ϕ for charged particles. Each ladder has many strips to measure the position of charged particles. The implant strip pitch is 25 μm and the readout strip pitch is 50 μm along the ϕ direction. The strips for z coordinate measurement are drawn perpendicular to the beam axis and implant strip pitch is 25 μm and the readout strip pitch is 100 μm for these strips.

One ladder is 181 mm long and 33 mm wide and the readout chips are attached at one end of the ladder as shown in figure 3.8. Each ladder is divided into three silicon strip detectors along the z direction. In table 3.4, the properties of a ladder for the silicon microvertex detector are summarized.

The single hit resolution was tested by using 5 GeV pion beam. The intrinsic single hit resolution is 5 μm for the ϕ direction and 13 μm for the z direction at a normal incidence to the plane. The resolution for the z direction depends on the incident angle. The measured resolution is 15 μm at 30° and 20 μm at 45°. And the impact parameter resolutions, σ_{d_0} for the radial direction and σ_{z_0} for the z direction, were investigated by the 1993 data. For normal incident angle tracks $\sigma_{d_0} = 18$ μm and $\sigma_{z_0} = 85$ μm were obtained.

In table 3.5, the properties of the silicon microvertex detector are summarized.

b) Central Vertex Detector

The central vertex detector is a high precision drift chamber which is located outside the

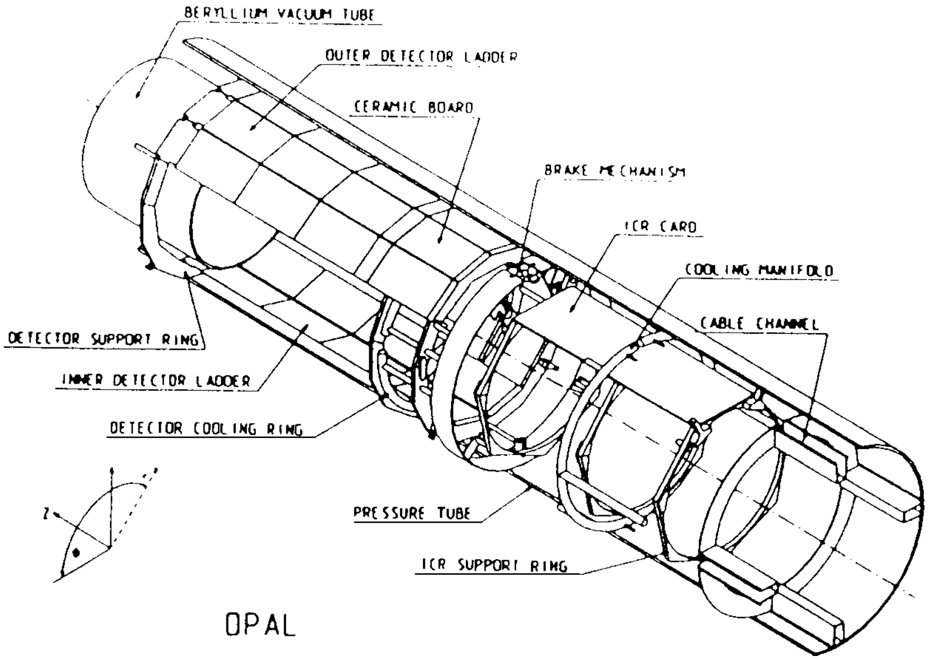

Figure 3.6: The schematic view of the silicon microvertex detector

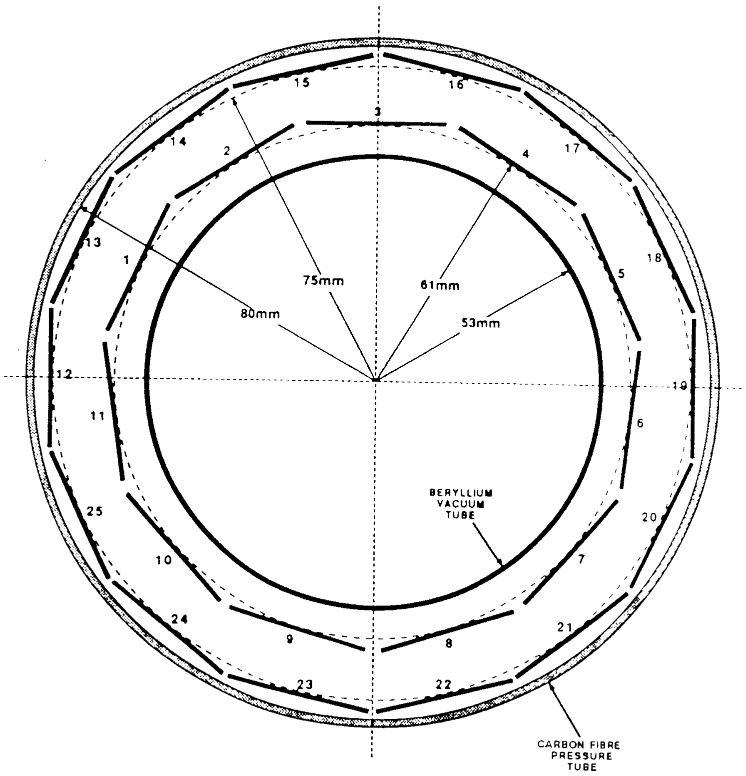

Figure 3.7: The view of cross section for the silicon microvertex detector

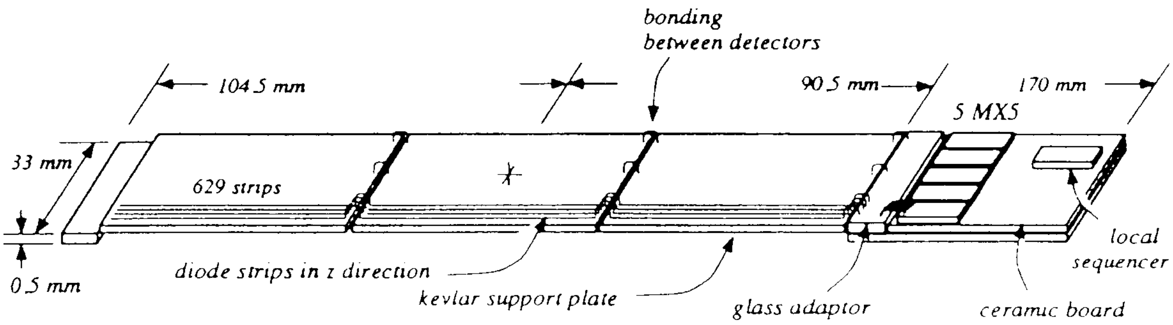

Figure 3.8: The schematic view of the ladder for the silicon microvertex detector

	ϕ side	z side
Silicon thickness	250 μm	
Implant strip pitch	25 μm	
Readout strip pitch	50 μm	100 μm
Intrinsic resolution	$\sim$5 μm	$\sim$13 μm
Number of readout channels	629	584
Signal to noise ratio (peak)	24	20

Table 3.4: The summary of a ladder for the silicon microvertex detector

Number of ladders/layer	11 (inner), 14 (outer)
Effective radius of layer	61 mm (inner), 75 mm (outer)
Maximum $\lvert\cos\theta\rvert$ acceptance	0.83 (inner), 0.77 (outer)
ϕ acceptance	88% (inner), 91% (outer)
Average material (radiation length)	1.5% at normal incidence
Strip biasing method	FoxFET (gated reachthrough channel)
2 coordinate detection	back-to-back ϕ and z single-sided detectors
z readout scheme	gold printed circuit on 200 μm thick glass
Number of active channels	30325
Readout chip, noise, power	MX7, 350e+15e/pF, 2 mW/channel
Radiation hardness	about 500 Gy (MX7 chip)
Cooling method	water cooling
Number of good channels	$\sim$99%

Table 3.5: The summary for the properties of the silicon microvertex detector

silicon microvertex detector. This detector is 1 m long and 23.5 cm radius and consists of two layers with 36 sectors. The inner and outer layers are separated by the foil at a radius of 17.5 cm. The angular coverage is $23^\circ \leq \theta \leq 157^\circ$ corresponding to 92% of the whole solid angle for the inner plus outer layers and $18^\circ \leq \theta \leq 162^\circ$ corresponding to 95% of the whole solid angle for the inner layer only. This subdetector works under the pressure at 4 bar within the pressure vessel. The mixed gas used consists of argon, methane and isobutane as described before. The schematic view of this subdetector is shown in figure 3.9 and the cross section of this subdetector is shown in figure 3.10.

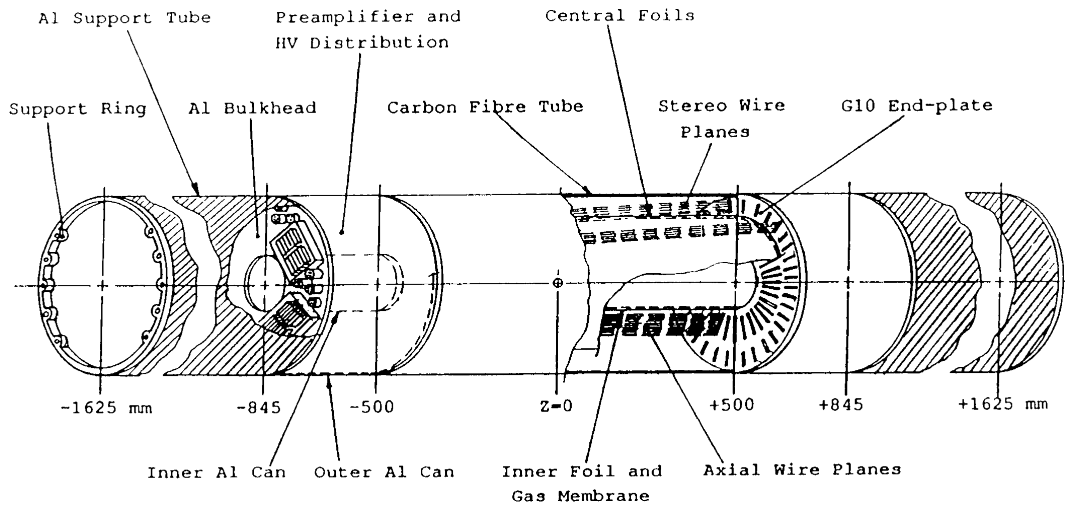

Figure 3.9: The schematic view of the central vertex detector.

The wire planes in the cells in the inner layer are parallel to the beam axis; i.e., axial wires. On the other hand, the wire planes in the cells in the outer layer are declined by about $\sim 4^\circ$ with respect to the beam axis; i.e., stereo wires. A wire plane is formed by 12 anode wires at the radius from 10.3 cm to 16.2 cm for the inner layer and 6 anode wires at the radius from 18.8 cm to 21.3 cm for the outer layer. The anode wires are the gold plated W-Rh wires whose diameter is 20 μm. The wire spacing is 5.4 mm for the inner layer and 5.0 mm for the outer layer, and a potential wire, which is the gold plated Cu-Be wire of 200 μm in diameter, is strung between the anode wires. The cathode wire planes consist of the Cu-Be wires whose diameter is 125 μm and those wires are strung at 1 mm interval. To adjust the electrostatic field in the cell, the field shaping rings are located at the edge of the cells. By these rings, the constant electrostatic field for all cells is formed.

This constant electrostatic field provides the constant drift velocity of electrons that are generated by the ionization loss when a charged particle passes through the vertex detector. By measuring this drift time precisely, the position in r-ϕ plane can be measured. The spatial resolution in r-ϕ plane is about 55 μm.

The z coordinate is measured by using information on the time difference between both ends of an anode wire. The spatial resolution in the z direction is 4 cm for a single anode wire. By combining information on the z coordinate obtained from inner layer (axial wire cells) and the outer layer (stereo wire cells), the spatial resolution in the z direction is further improved to be 700 μm.

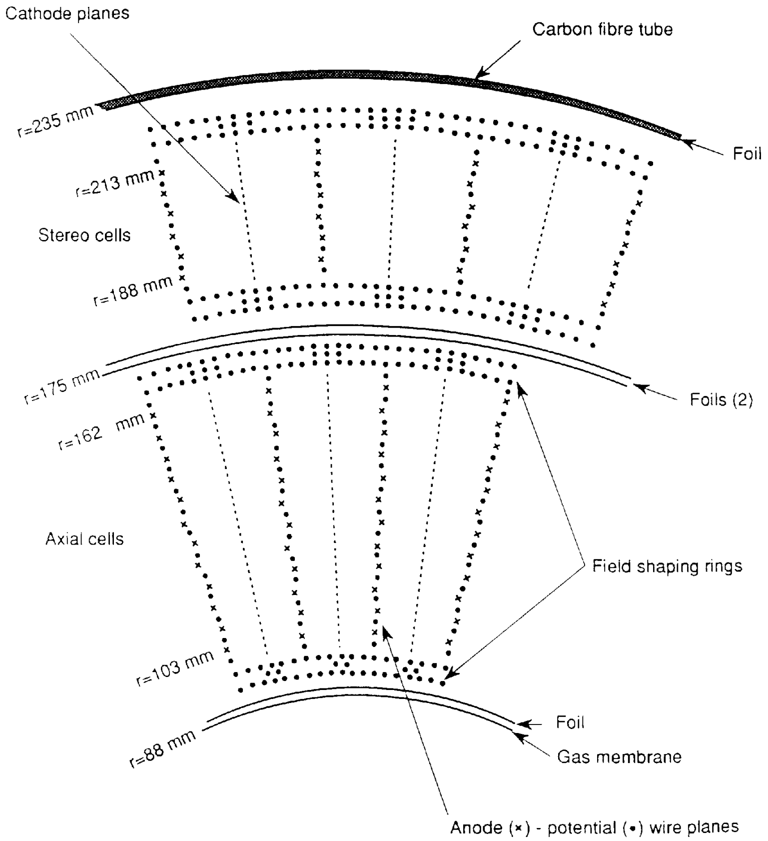

Figure 3.10: The cross section of the central vertex detector.

Multiple hits on a wire can be recorded. On each wire the hit nearest to the wire is recorded as the 'first hit' and all others as 'second hits'.

In table 3.6, the properties of the central vertex detector are summarized.

Wire organization	36 sectors axial – 12 wires/sector
	36 sectors stereo (4°) – 6 wires/sector
Wire spacing	5.3 mm for the inner layer
	5.0 mm for the outer layer
Wire stagger	$\pm 41\ \mu$m
maximum drift distance	1.4 cm
Maximum drift time	0.5 μsec
Gas	argon (88.2%), methane (9.8%), isobutane (2.0%)
Gas gain	2×10^4
Angular coverage	$23° \leq \theta \leq 157°$ for axial + stereo wires
	$18° \leq \theta \leq 162°$ for axial wires
Coordinate determination	drift time in the ϕ direction
	ΔT and stereo wires in the z direction
Spatial resolution	55 μm in the ϕ direction
	4 cm (ΔT), 700 μm (stereo) in the z direction
Double hit resolution	2.0 mm
Trigger z/r	all axial wires

Table 3.6: The summary for the properties of the vertex detector

c) Central Jet Chamber

The central jet chamber is a large volume tracking chamber and one of the main components of the OPAL detector. This detector is cylindrical and 4 m long. The inner and outer walls of the jet chamber are at the radii of 0.25 m and 1.85 m respectively. The jet chamber is divided into 24 sectors each with the anode wire plane consisting of 159 sense wires (anode wires). The spacing between anode wires is 1.0 cm. The cathode plane is formed by cathode wires at the border between two sectors. The cross sections of the central jet chamber in r-ϕ plane and r-z plane are shown in figure 3.11.

In figure 3.12, the cross section of the sector is shown. These anode wires are strung between radii of 25.5 cm and 183.5 cm and alternating at the right and left side of the anode wire plane to avoid the ambiguity whether particles pass through at the right or left side on the anode plane. This gap between the anode plane and an anode wire is 100 μm. The angular coverage is $43° \leq \theta \leq 137°$ corresponding to 73% of the solid angle of 4π for 159 wires and is $11° \leq \theta \leq 169°$ corresponding to 98% of the solid angle of 4π for the innermost 8 wires.

The position of the track is known by measuring the drift time precisely for the r-ϕ plane and by the charge division technique for the z coordinate. The drift length is 3 cm at the most inner wire and 25 cm at the most outer wire. The spatial resolution in the r-ϕ plane is 135 μm at the mean drift length of 7 cm. In the charge division technique, the charge collected from one anode wire is divided into two and each charge is measured at each end of the wire. Depending on the position where the charge is collected on the anode wire, the amount of charge varies at each end point. By using this difference between the charges at both ends, the z coordinate is measured and the spatial resolution for the z direction is 6 cm.

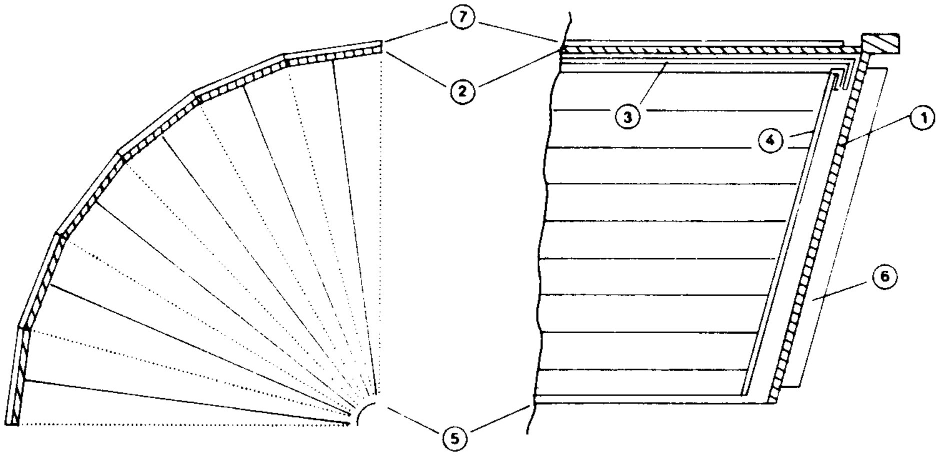

Figure 3.11: The cross sections of the central jet chamber in r-ϕ plane (left) and r-z plane (right). The numbers indicate the conical endplate (1), the shell of aluminum panels (2), barrel (3) and endcap (4) field shaping electrodes, the inner field shaping (5), the anode wire suspension (6), and the z-chambers.

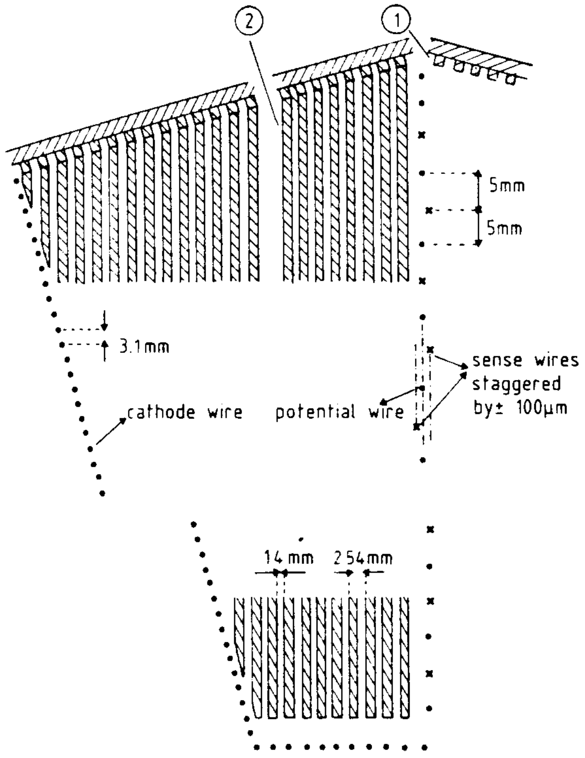

Figure 3.12: The cross section of one half sector of the jet chamber. The numbers indicate the barrel (1) and endcap (2) field shaping electrodes.

The ionization loss, called dE/dx, for each track is measured by the total charge collected from both ends of the wire. This information on the ionization loss is used to identify particles. In figure 3.13, the observed ionization losses are shown as a function of the momentum of the track in multihadronic events and dimuon events. The error of the measured ionization loss, $\sigma_{(dE/dx)}/(dE/dx)$, is 3.8% for the tracks with 159 hit points in dimuon events.

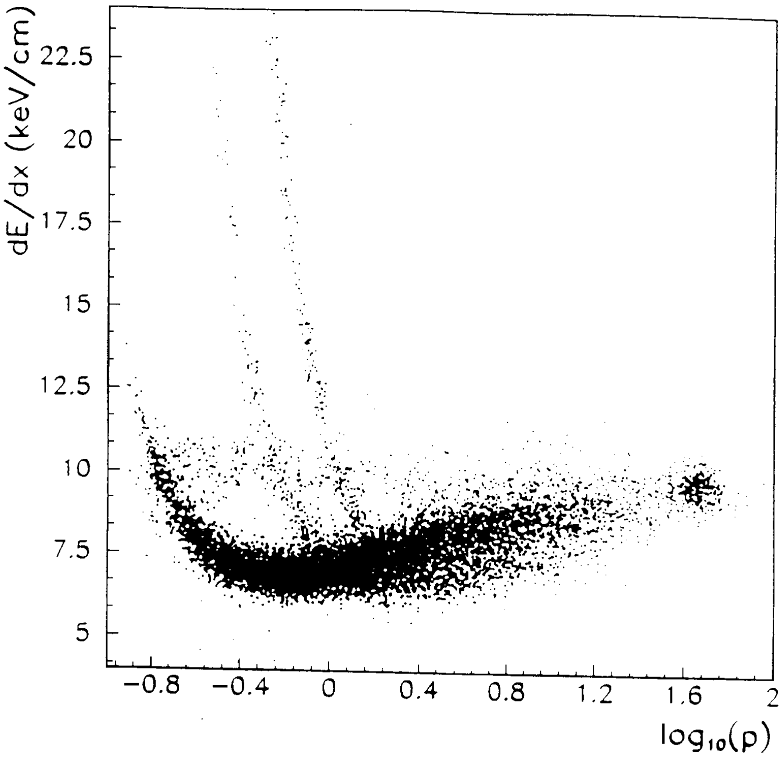

Figure 3.13: The ionization losses measured by the jet chamber using multihadronic events and dimuon events.

Since this jet chamber is located inside the magnet which supplies the magnetic field of 0.435 T as described in 3.2.2, charged particles are bent by this magnetic field in the jet chamber. By measuring the curvature of the track, the momentum of charged particle can be measured. The measured distribution of $1/p$ of the tracks for dimuon events is shown in figure 3.14, where μ^+ and μ^- tracks are clearly separated. The obtained momentum resolution is $\sigma_p/p^2 \sim 2.2 \times 10^{-3}$ GeV^{-1}.

The mixed gas used in this jet chamber consists of argon (88.2%), methane (9.8%) and isobutane (2.0%) like the vertex detector. Since the oxygen has a large electron attachment coefficient, the oxygen is extracted as much as possible and the level of the oxygen is reduced down to a few ppm. But a little water vapor is intentionally contained in the mixed gas to extend the lifetime of this chamber. The level of the water vapor is ~500 ppm and is kept within ±50 ppm.

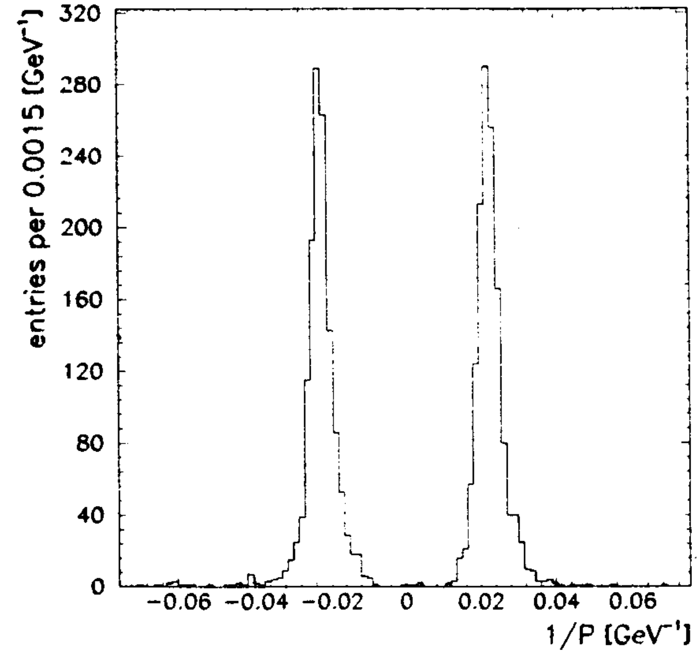

Figure 3.14: The $1/p$ distribution of the tracks for dimuon events.

The calibrations on the drift time and the charge division are performed by illuminating the Nb-Yag laser light whose wavelength is 266 nm and pulse duration is 3 nsec at the fixed position. Due to the illumination of the laser, the molecules in the chamber are excited and electrons are emitted from the molecules. Since the position where the molecules are excited is known precisely, the calibration on the drift time and the z position can be performed.

In table 3.7, the properties on the jet chamber are summarized.

d) Z-Chamber

Z-chamber is located outside the central jet chamber in order to measure the z coordinates of tracks precisely and to improve the invariant mass resolution. This subdetector consists of the 24 drift chambers, each of which is 4 m long, 50 cm wide and 5.9 cm thick. The schematic views of z-chamber in both the ϕ-z and r-ϕ plane are shown in figure 3.15.

Each chamber is divided into 8 cells along the z direction; each cell is a square with a side of 50 cm. There are gaps between chambers and this subdetector covers 94% of the azimuth angle. The coverage in the z direction is $44^\circ \leq \theta \leq 136^\circ$ corresponding to $|\cos\theta| < 0.72$. The cross section along the z direction of the z-chamber cell is shown in figure 3.16.

Six sense wires are strung at the center of each cell perpendicular to the beam axis as illustrated in figure 3.16. The maximum drift length is about 25 cm which corresponds to the drift time of 5 μsec. These wires are strung at alternating right and left side of the center of the anode plane to avoid the left-right ambiguity of the track as in the jet chamber. This stagger, which is a gap between each anode wire and the center of the anode plane, is ± 250 μm. And the spacing between each anode wire is 0.4 cm.

The z coordinate of a track is obtained by measuring the drift time precisely. The spatial resolution in the z direction is 100–350 μm, which depends on drift length. On the other hand, the position measurement in the r-ϕ plane is performed by using the charge division technique

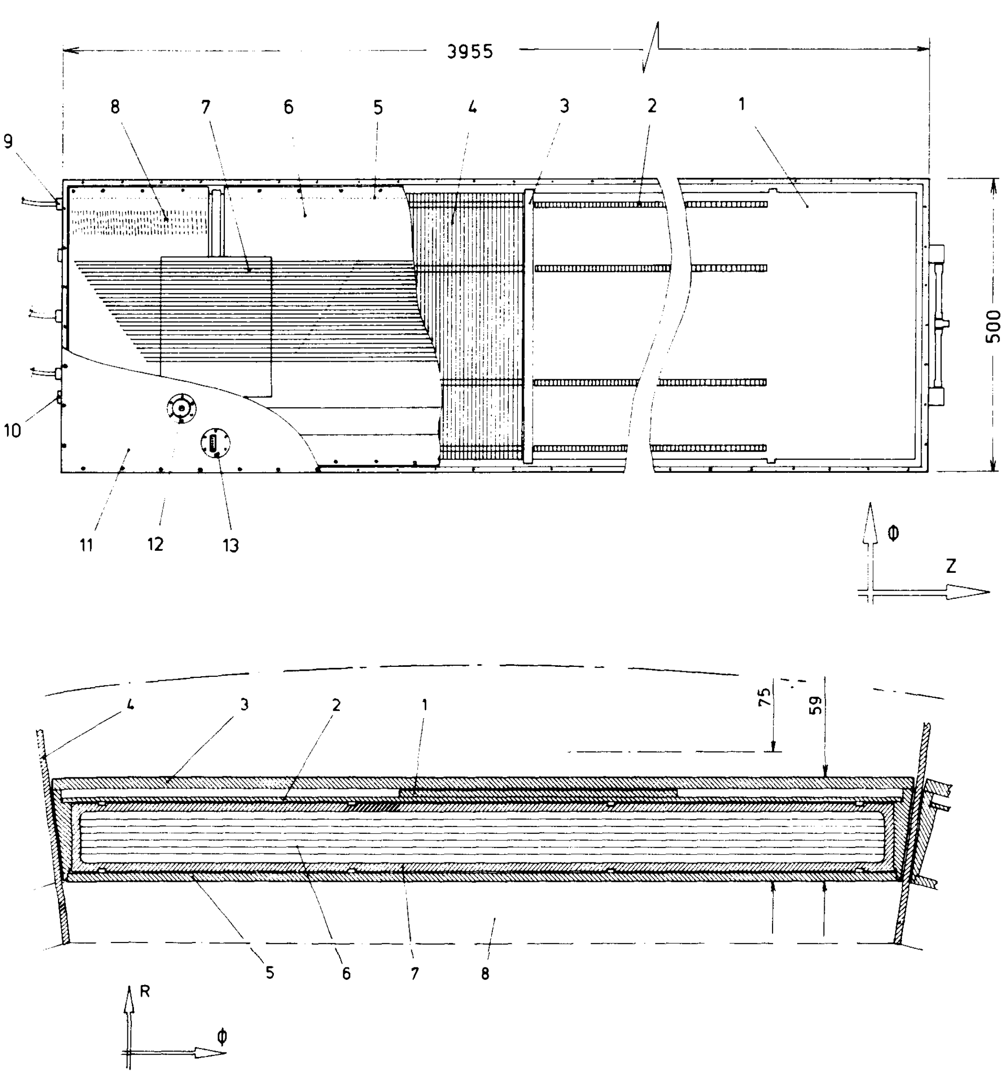

Figure 3.15: The schematic view of the z-chamber in ϕ-z plane (top) and in r-ϕ plane (bottom). For the top figure, the numbers indicate the Lexan box (1), electrode spacer combs (2), anode module (3), drift field electrodes (4), electrode HT connections (5), HT distribution board (6), HT bridging board across anode module (7), resistors of HT divider chain (8), HT cables for drift field (9), gas exhaust (10), Lexan cover (11), pressure relief valve (12) and anode wire signal connector (13). And for the bottom figure, HT bridging board (1), HT distribution board (2), Lexan cover (3), structural rib (4), Lexan box (5), anode wires (6), drift field electrode (7) and structural member of jet chamber (8). All dimensions are in mm.

Wire organization	24 sectors axial – 159 wires/sector
Wire spacing	1.0 cm
Wire stagger	$\pm 100\ \mu$m
maximum drift distance	25 cm
Maximum drift time	5 μsec
Gas	argon (88.2%), methane (9.8%), isobutane (2.0%)
Gas gain	10^4
Angular coverage	$43^\circ \leq \theta \leq 137^\circ$ for 159 wires $11^\circ \leq \theta \leq 169^\circ$ for at least 8 wires
Coordinate determination	drift time in the ϕ direction charge division in the z direction
Spatial resolution	135 μm in the ϕ direction 6 cm in the z direction
Double hit resolution	2.5 mm
Energy loss, dE/dx	3.0% (159 samples)
Trigger z/r	3 groups of 12 wires per sector

Table 3.7: The summary of characters for the jet chamber.

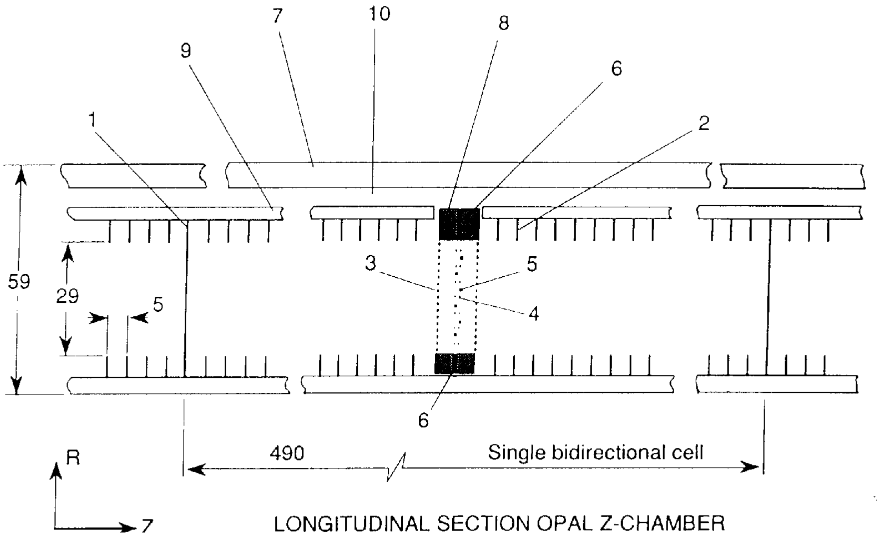

Figure 3.16: The cross section along the z direction of the z-chamber. The numbers indicate cathode (1), drift field electrodes (2), grid wires (3), guard wires (4), anode wires (the stagger has been exaggerated for graphic purposes) (5), inner electrode for wire 1 and 6 gain control (6), Lexan box and cover (7), G-10 (glass-epoxy composite) anode module (8), HT distribution board (9) and space for the HT resistor chain, HT bridging board and anode module cabling. Al dimensions are in mm.

like a z coordinate measurement in the jet chamber. This spatial resolution is 15 mm.

The mixed gas which is used in the z-chamber is the same as the other inner gas chambers; the components of the mixed gas are argon (88.2%), methane (9.8%) and isobutane (2.0%).

In table 3.8, the properties on the jet chamber are summarized.

Wire organization	24 chambers – 8 cells/chamber – 6 wires/cell
Wire spacing	0.4 cm
Wire stagger	± 250 μm
maximum drift distance	25 cm
Maximum drift time	5 μsec
Gas	argon (88.2%), methane (9.8%), isobutane (2.0%)
Gas gain	2–5$\times 10^4$
Angular coverage	$44° \leq \theta \leq 136°$ (94% in ϕ)
Coordinate determination	charge division in the ϕ direction drift time in the z direction
Spatial resolution	15 mm in the ϕ direction 100 – 350 μm in the z direction
Double hit resolution	2.5 mm

Table 3.8: The summary of characters for the z-chamber.

3.2.4 Time of Flight System

Time of flight counters are located at the mean radius of 2.36 m surrounding the magnet. The aim of this subdetector is to identify particles with low momentum (0.6 – 2.5 GeV/c), to provide the fast trigger information and to reject the backgrounds due to cosmic rays.

Time of flight counter consists of the 160 scintillation counters, NE110 [46]. Each scintillation counter is 6.84 m long and 4.9 cm thick and its cross section is a trapezoid with sides of 8.9 cm and 9.1 cm. Each scintillation counter is covered with aluminized mylar and furthermore wrapped by the black PVC sheet. By this wrapping, each scintillation counter is optically independent each other. These scintillation counters are set parallel to the beam axis. This subdetector covers the region of $|\cos\theta| < 0.82$. But there are gaps between adjacent counters in the ϕ direction and the maximum gap width is 2.6 mm.

The scintillation light is emitted when a charged particle passes through this subdetector. The emitted light is collected by the photomultiplier [47] which is located at both ends of each counter via the 30 cm light guide with a cross section of a circle. These parts are glued to other parts.

The calibration of these counters is performed by illuminating the nitrogen laser which makes a pulse similar to the real signal.

The timing resolution of this subdetector is 280 psec at the center of the counter and 350 psec at the edge of the counter. The spatial resolution in the z direction is 5.5 cm. By using information on the z coordinate obtained from other subdetector, the timing resolution at the edge of the counter is improved to be 220 psec although the timing resolution at the center of the counter is not improved.

3.2.5 Electromagnetic Calorimeter System

This system provides information on the energy of electrons (positrons) and photons and covers the solid angle of nearly 4π. This system is divided into two parts; the barrel region with $|\cos\theta| <\sim 0.8$, and the endcap region with $|\cos\theta| >\sim 0.8$. At the region of $|\cos\theta| \sim 0.8$, the electromagnetic barrel calorimeter and the electromagnetic endcap calorimeter are superposed to avoid the leakage of the electromagnetic shower behind this system. There is an important difference between two systems. The calorimeter system in the barrel region is located outside the magnet and the calorimeter system in the endcap region is in the magnetic field. In order to be operated in the magnetic field, the system in the endcap region is designed so as not to be affected by the high magnetic field.

In figure 3.17, the radiation lengths in front of and inside the electromagnetic calorimeters are shown as a function of $\cos\theta$. The radiation length in front of the calorimeter is long in the region $\sim 0.70 < |\cos\theta| <\sim 0.80$. This is due to the wall of the pressure vessel which keeps the pressure high in the central tracking detector.

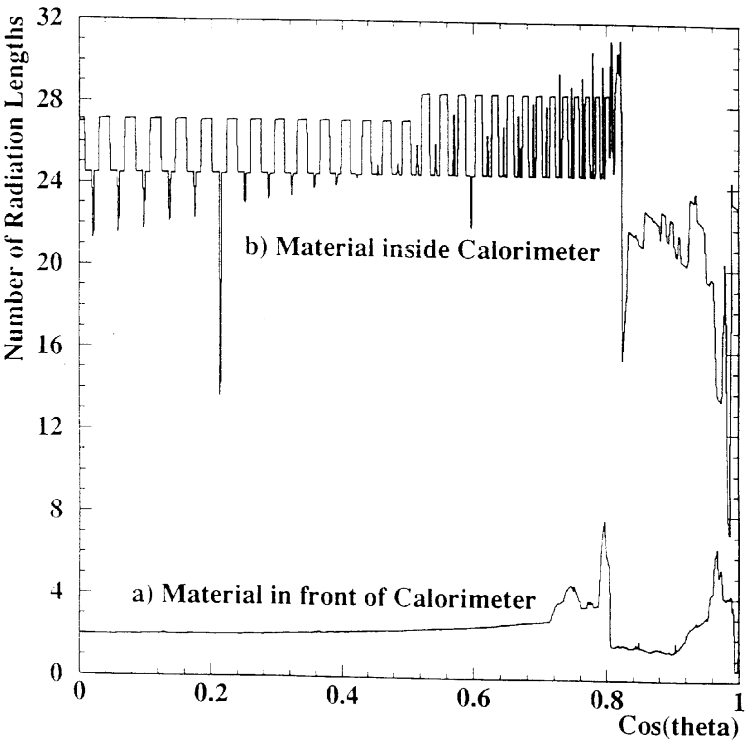

Figure 3.17: The radiation length in front of and inside the electromagnetic calorimeters as a function of $\cos\theta$

The electromagnetic calorimeter is a main part to measure the energy of electrons (positrons) and photons with an excellent accuracy. Due to the existence of the magnet and the pressure vessel in front of this system, particles have to pass through the large materials ($\sim 2X_0$) and most of them initiate the electromagnetic shower in the magnet or the pressure vessel. As a result, the spatial resolution measured by the electromagnetic calorimeter alone becomes bad.

To improve the spatial resolution, the presampler is installed in front of the electromagnetic calorimeter.

a) Electromagnetic Barrel Presampler

Electromagnetic barrel presampler [48, 49] is located at the mean radius of 2.388 m and installed between the time of flight counter and the barrel electromagnetic calorimeter to improve the spatial resolution and the energy resolution. In particular, since the electromagnetic shower is initiated in the coil due to its large material, the contribution to the spatial resolution by this subdetector is very important.

This subdetector consists of 16 chambers with two layers. The chambers are 6.623 m long and 3.0 cm thick and this subdetector covers the region of $|\cos\theta| < 0.81$. These chambers consist of four PVC extrusions having 24 cells which are the limited streamer tubes and the cross section of each cell is the square of the side of $\sim$1 cm. The wall thickness to separate cells is 1 mm. The anode wire, which is a stainless steel with a diameter of 75 μm, is strung at the center of each cell parallel to the beam axis and the cathode strips are on the inner and outer side of the cell. The spacing between wires is 9.6 mm. The cathode strips are inclined about 45° with respect to the anode wires. Although there are gaps between adjacent cells, there is no inefficient region by shifting cells in each layer by a half size of the cell. The schematic view of the barrel presampler is shown in figure 3.18.

These chambers work in a limited streamer mode as described above. The high voltage at the cathode plane is 4.1 kV and the anode wires are grounded. The wall between cells have a large resistance of $\sim$1 MΩ/square. The mixed gas in the chamber consists of n-pentane (32%) and CO_2 (68%). This mixed gas is produced by bubbling CO_2 in the tank filled with n-pentane.

The measurement of the z coordinate is performed by the charge division technique like the jet chamber. The spatial resolution in the z direction behind the material of about 2.1 radiation lengths is about 10 cm in the case of a single charged particle. By taking into account information on the position obtained from the cathode strips, this spatial resolution is improved. And, since the energy of the particles deposited in the material in front of the barrel presampler linearly depends on the multiplicity of the hits observed by the barrel presampler, information obtained from this subdetector can be also used to improve of the energy resolution.

The properties of the barrel presampler are summarized in table 3.9.

Angular coverage, $\lvert\cos\theta\rvert$	< 0.81
Active detector	Limited streamer tubes
Number of anode (cathode) layers	2 (4)
Wire diameter and type	75 μm stainless steel
Wire spacing	9.6 mm
Cathode strip pitch	11 mm
Typical high voltage	4.1 kV
Gas	n-pentane (32%), CO_2 (68%)
Number of readout channels	21504
Intrinsic spatial resolution for mip	$\sim$2 mm

Table 3.9: The summary of the properties for the electromagnetic barrel presampler

b) Electromagnetic Barrel Calorimeter

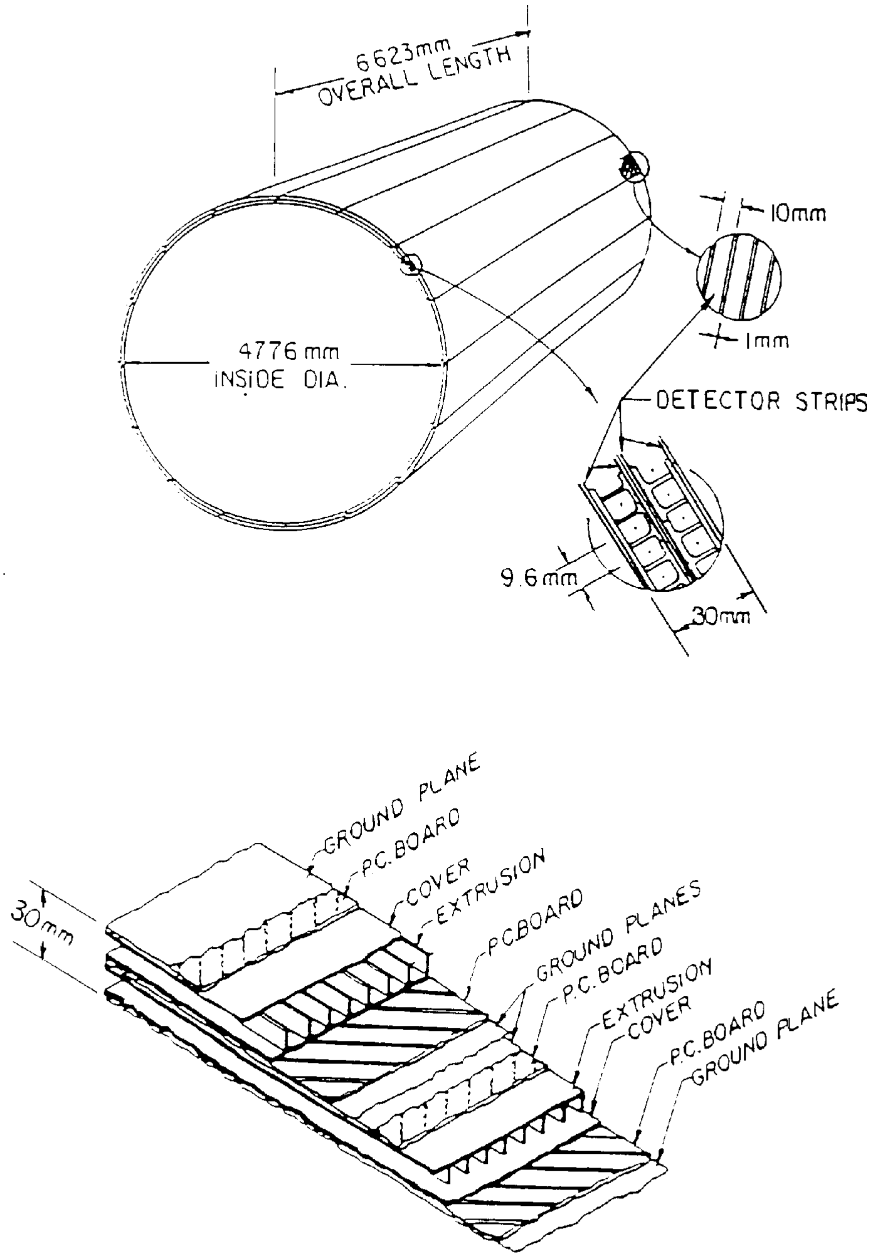

Figure 3.18: The schematic view of the barrel presampler.

The electromagnetic barrel calorimeter is one of the main components of the the OPAL detector. This subdetector is located at the radius of 2.455 m and about 7 m long in the z direction. The angular coverage of the subdetector is $|\cos\theta| < 0.82$.

This subdetector consists of 9440 lead glass counters, each of which has a cross section of $\sim$10 cm$\times$ $\sim$10 cm and 37.0 cm depth. To avoid the leakage of the energy of electrons (positrons) and photons behind the counters, the newly developed dense lead glass counters with a high refraction index, SF57 [50], are used. The radiation length of the counter is 1.50 cm and 37.0 cm depth corresponds to 24.6 radiation lengths ($24.6X_0$).

These lead glass counters are supported by the stainless flange to the support ring which is divided into two half rings with five sectors in the z direction. A total of 59 lead glass counters are arranged in the z direction and 160 lead glass counters are arranged in the ϕ direction. The block layout is shown in figure 3.19 for r-z plane and for r-ϕ plane. To keep the electromagnetic energy in as a small number of counters as possible, each counter is pointed to the interaction region. In order to reduce the leak energy through the gap between adjacent counters, each counter is tilted in order not to point perfectly to the interaction point. The counters point to the different position in the range of $|z| = 55.5 \sim 157.9$ mm and tilted by 0.574° with respect to the ϕ direction.

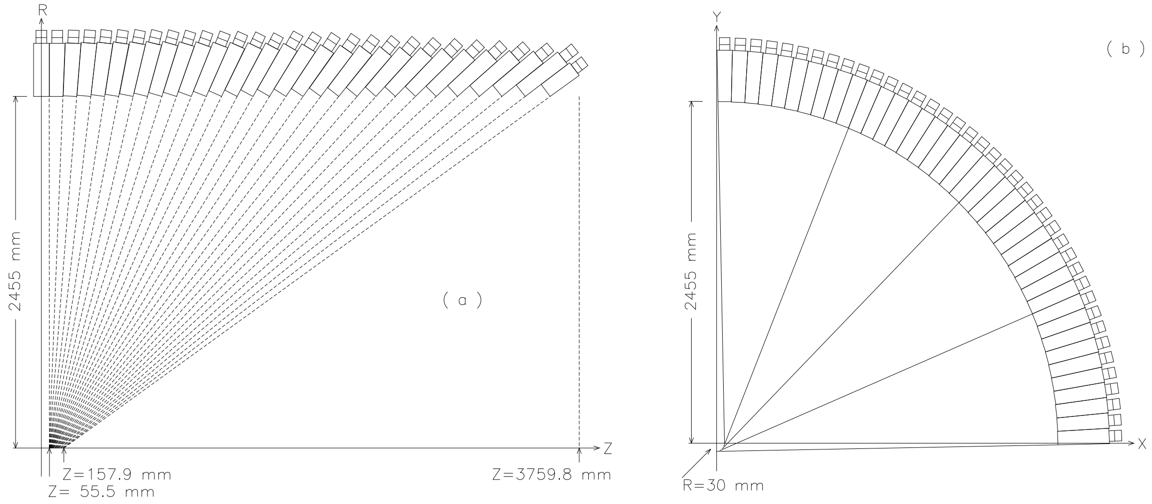

Figure 3.19: The block layout of the electromagnetic calorimeter in r-z plane (a) and in r-ϕ plane (b).

Each counter consists of the lead glass block, the light guide to transfer the Čerenkov light emitted in the lead glass block and the photomultiplier [51] which detects the light and convert it to the electric signal. These parts are connected by the optical glue [52]. The assembly of the lead glass counter with a light guide and the photomultiplier is shown in figure 3.20.

The Čerenkov light is emitted in the lead glass blocks due to the electromagnetic shower caused by the incident particles like electrons (positrons) and photons. To collect this Čerenkov light efficiently, all surfaces of each lead glass block are sufficiently polished and each block is covered with aluminized mylar. Still more, each block is covered with the black sheet which is not transparent for the light.

The light guide is installed to reduce of the effect on the stray magnetic field and made of

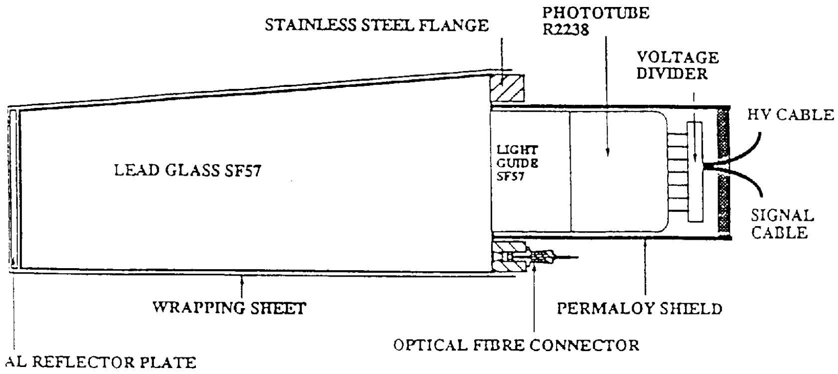

Figure 3.20: The assembly of the lead glass counter with a light guide and a photomultiplier.

the same material with the lead glass block. This light guide is 4 or 6 cm long and its cross section is a circle with a radius of 3 inches.

The photomultiplier, whose diameter is 3 inches, is specially developed for this experiment. Although the stray magnetic field is ~20 gauss, which is very small, each photomultiplier is shielded by a tube of the Permaloy metal [53]. The standard gain of this device is $\sim 1.0 \times 10^5$ at the normal condition (high voltage ~1 kV).

The relative calibration of these counter gains is performed by illuminating the xenon flash light. The spectrum of the light emitted from the xenon flash lamp is almost the same as the spectrum of the Čerenkov light. The light emitted from the xenon is transferred by the optical fiber and the lead glass block is illuminated from the bottom toward the top of the block to avoid the direct illumination onto the photomultiplier cathode. The diffuser which is a white painted board is installed at the top of the block. By reflecting and diffusing the light at the diffuser, the realistic situation is simulated when the particles deposit its energy in the block.

The energy resolution is $\sigma_E/E = 0.2 + 6.3/\sqrt{E}$ % (E in GeV) without the material in front of the barrel electromagnetic calorimeter. In the case of the existence of the material of $2.08X_0$ in front, the energy resolution becomes worse by a factor ~2 compared with the case of no material in front. And the intrinsic spatial resolution of this subdetector is about 11 mm at 6 GeV.

In table 3.10, the properties of the electromagnetic barrel calorimeter are summarized.

c) Electromagnetic Endcap Presampler

The electromagnetic endcap presampler [54] is installed between the pressure vessel and the endcap electromagnetic calorimeter at $z = \pm \sim 2.2$ m. The angular coverage is $0.83 < |\cos\theta| < 0.95$ and the azimuthal angle is fully covered. In figure 3.21, the three dimensional view of the endcap presampler is shown with the electromagnetic endcap calorimeter which is described later.

As shown in figure 3.21, this subdetector is of the umbrella shaped structure as a whole and contains 16 sectors which consist of the large chambers and small chambers. The cross section of these chambers is a trapezoid. The large chambers are inclined by 18° with respect to r-ϕ plane and the small chambers are perpendicular to the beam axis. Since these sectors

Angular coverage, $\lvert\cos\theta\rvert$	< 0.82
Material	SF57, $X_0 = 1.50$ cm
Block geometry	Quasi-pointing
Typical block dimensions	$\sim 10 \times \sim 10 \times 37.0$ cm^3
Depth (for photons from origin)	$24.6X_0$
Number of blocks	9440
Čerenkov light detector	Field tolerant phototube
Typical magnetic field at detector	0.002 T
Detector gain	$\sim 1.0 \times 10^5$
Detector high voltage	~ 1.0 kV
Channel equivalent noise	~ 2 MeV
Intrinsic energy resolution	$\sigma_E/E = 0.2 + 6.3/\sqrt{E}$ %
Intrinsic spatial resolution at 6 GeV	~ 11 mm
Trigger E >1 GeV	24ϕ bins $\times$ 5θ bins

Table 3.10: The summary of properties for the electromagnetic barrel calorimeter.

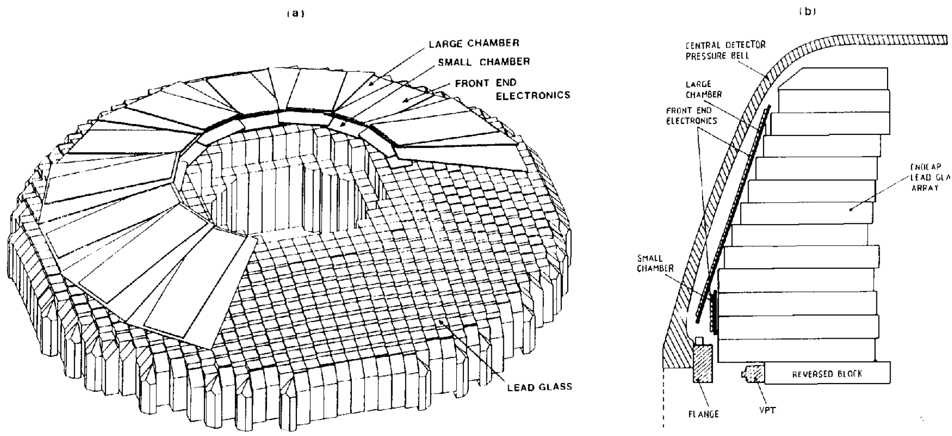

Figure 3.21: The three dimensional view of the endcap electromagnetic calorimeter system including the endcap presampler and the endcap electromagnetic calorimeter. (a) is the schematic view of this system and (b) is the cross section in the r-z plane.

are superposed on each other, there are no gaps between adjacent cells, in other word, there are no inefficient region in the ϕ direction.

The mixed gas which is used in this subdetector is the composite of the n-pentane (45%) and the CO_2 (55%) which is not the same as the gas which is used in the electromagnetic barrel presampler described before.

The properties of the electromagnetic endcap presampler are summarized in table 3.11.

Angular coverage, $\lvert\cos\theta\rvert$	0.83 – 0.95
Active detector	Thin high gain MWPCs
Number of anode (cathode) layers	1 (2)
Wire diameter and type	55 μm gold plated tungsten
Wire spacing	4×2.0 mm
Cathode strip pitch	18 mm
Typical high voltage	3.5 kV
Gas	n-pentane (45%), CO_2 (55%)
Number of readout channels	6080
Intrinsic spatial resolution for mip	2 – 4 mm

Table 3.11: The summary of properties for the electromagnetic endcap presampler

d) Electromagnetic Endcap Calorimeter

The electromagnetic endcap calorimeter [55, 56] is installed between the endcap electromagnetic presampler and the hadron pole tip calorimeter at both sides of the OPAL detector. The three dimensional view is shown in figure 3.21 with the electromagnetic endcap presampler. The angular coverage of this subdetector is full azimuth angle and $0.81 < \lvert\cos\theta\rvert < 0.98$ in the θ direction.

This subdetector at each side consists of the 2264 lead glass counters. These counters consist of the lead glass block to generate the Čerenkov light due to the electromagnetic shower by electrons (positrons) and photons, and the optical device to detect the light. Unlike the electromagnetic barrel calorimeter, the lead glass block and the optical device are connected directly by the optical glue, which is an epoxy resin. Due to the spatial constraint of the installation region, three types of the blocks, whose radiation lengths are 380, 420 and 520 mm respectively, are produced and the average radiation length is about $22X_0$. The blocks of these counters are mounted parallel to the beam axis. The assembly of one of these counters is shown in figure 3.22.

The lead glass block used in this subdetector is CEREN-25 [57], whose radiation length is 2.51 cm. Each surface of the block is optically polished and each block is wrapped with aluminum foil to collect the Čerenkov light with a good efficiency. Still more, the block is covered with a brass can with a wall thickness of 0.45 mm. As a result, the counter is optically independent to each other.

The different point compared with the electromagnetic barrel calorimeter is that the electromagnetic endcap calorimeter is installed in the magnetic field of 0.435 T. Thus the photomultiplier as used in the barrel calorimeter can not be used. For this subdetector the vacuum photo triode (VPT) [58], which is a single stage multiplier, is adopted so as to work in the magnetic field of ~0.4 T. The typical gain is about 12.3 at the high voltage of 1.0 kV with a low noise.

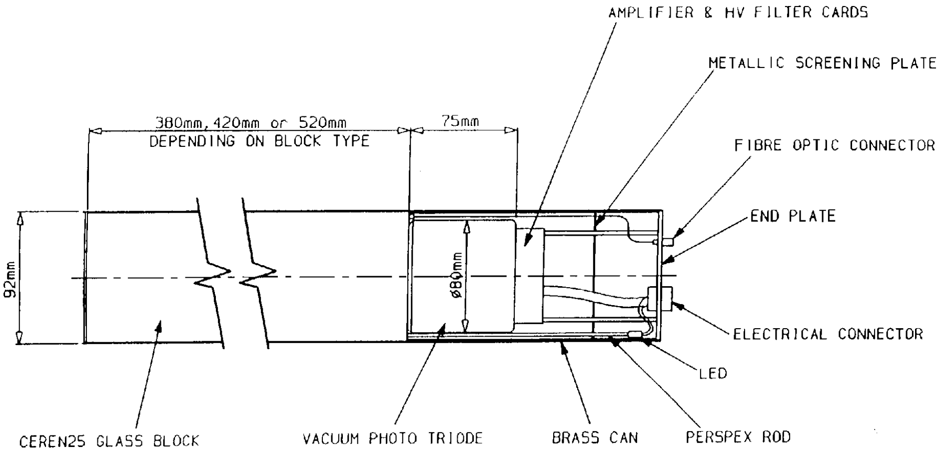

Figure 3.22: The assembly of the lead glass counter with a vacuum photo triode.

This subdetector has two calibration systems. One of them is by the scintillation light and the other is by the LED light. For the former, the light pulse is generated by illuminating the nitrogen pulse laser to the liquid scintillator. The generated light is transferred by the optical fiber to the end of the block. By illuminating the light to the blocks and measuring the signal, the calibration constants can be obtained. For the latter, the LED which is installed at the end of the block emits a green light to the block and the gain of each block is calibrated.

The energy resolution of this subdetector was measured to be $\sigma_E/E = 5/\sqrt{E}$ % at low energy.

In table 3.12, the properties of the electromagnetic endcap calorimeter are summarized.

Angular coverage, $\lvert\cos\theta\rvert$	0.81 – 0.98
Material	CEREN 25, $X_0 = 2.51$ cm
Block geometry	Coaxial with beam line
Typical block dimensions	$9.2 \times 9.2 \times 52.0$ cm^3
Depth (for photons from origin)	$\sim 22X_0$
Number of blocks	2264
Čerenkov light detector	Vacuum photo triode
Typical magnetic field at detector	0.45 T
Detector gain	~12.3
Detector high voltage	~1.0 kV
Channel equivalent noise	~14 MeV
Intrinsic energy resolution	$\sigma_E/E = 5/\sqrt{E}$ % at low energy
Intrinsic spatial resolution at 6 GeV	~11 mm
Trigger E >1 GeV	24ϕ bins $\times$ 2θ bins

Table 3.12: The summary of properties for the electromagnetic endcap calorimeter.

In table 3.13, the properties on the electromagnetic calorimeter system, the electromagnetic calorimeter and the electromagnetic presamplers for the barrel and endcap region, are shown.

	Barrel	Endcap
Typical material in front of lead glass	$\sim 2X_0$	$\sim 2X_0$
Typical material to back of lead glass	$\sim 26.5X_0$	$\sim 23.5X_0$
Typical λ_{int} to back of lead glass	~ 2	~ 2
Spatial resolution for EM shower	~ 5 mm	2 – 5 mm
Electron - Hadron separation	$\sim 10^{-3}$	$\sim 10^{-3}$

Table 3.13: The summary of properties for the electromagnetic calorimeter system combined the calorimeter and the presampler for the barrel and the endcap region

3.2.6 Hadron Calorimeter System

Hadron calorimeter system is installed between the electromagnetic calorimeter system and the muon chamber system. This hadron calorimeter system, in general, consists of many layers of absorbers and gas chambers. The aim of this system is not only to measure the energy of the hadrons like pions and kaons but also to help the muon identification as an absorber.

This system is divided into three parts, the hadron barrel calorimeter in the barrel region, the hadron endcap calorimeter and the hadron pole tip calorimeter in the endcap region. The components of the hadron barrel calorimeter and the hadron endcap calorimeter are very similar.

In front of this system, the electromagnetic calorimeter system with a large material is installed as described before. So, the hadron energy which is measured by this hadron calorimeter system has to be corrected by using information obtained from the electromagnetic calorimeter system.

a) Barrel and Endcap Hadron Calorimeters

The barrel hadron calorimeter is located between the radii from 3.4 m to 4.4 m. The endcap hadron calorimeter is installed at both sides of the OPAL detector at the radii from 1.9 m to 3.3 m. The positions where these subdetectors are installed are shown in figure 3.3 and 3.4. The barrel hadron calorimeter covers the region of $|\cos\theta| < 0.81$ and the endcap calorimeter covers the region of $0.81 < |\cos\theta| < 0.91$.

The hadron barrel calorimeter and the hadron endcap calorimeter are very similar. In general, these calorimeters consist of several slabs and wire chambers between them. In figure 3.23, the layouts of these hadron calorimeters are shown.

The hadron barrel calorimeter has eight layers of slabs and nine layers of active detectors alternatively. Each slab, which is made of iron, is about 10 m long and 0.1 m thick corresponding to 0.6 interaction lengths ($0.6\lambda_0$). On the other hand, the hadron endcap calorimeter has seven layers of slabs and eight layers of active detectors alternatively. Due to large material of these slabs, most of hadrons generate the hadronic shower and deposit their energy in the slabs in the hadron calorimeter.

Particles in the hadronic shower are detected by the active detectors between layers of iron slab. These active detectors are the limited streamer tubes. For the hadron barrel calorimeter, this streamer tube is 10 m long and its cross section is 9 mm × 9 mm. The anode wire, whose diameter is 100 μm, is strung in each cell parallel to the beam axis and the spacing between anode wires is 10 mm. For the hadron endcap calorimeter, the layers of limited streamer tubes form a circle with a hole at the center and are superposed in the z direction. The diameter of

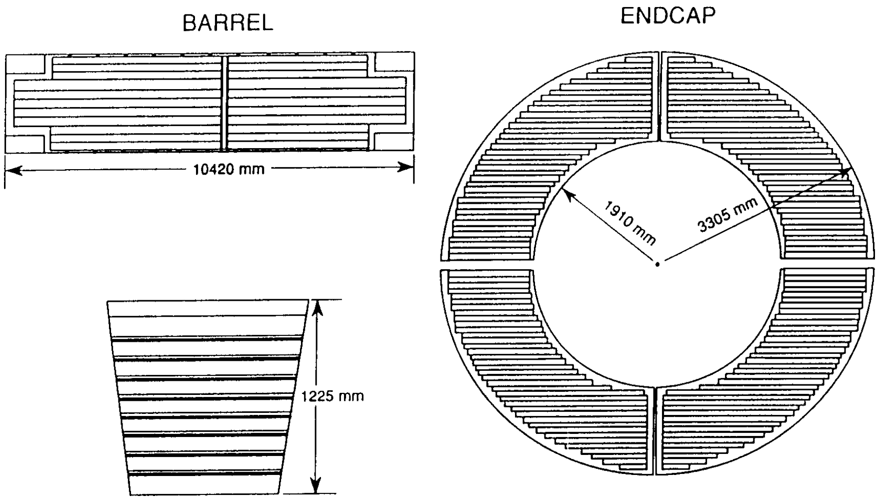

Figure 3.23: The layouts of the barrel barrel calorimeter and the endcap calorimeter. The figure at the left side is for the hadron barrel calorimeter and the figure at the right side is for the hadron endcap calorimeter. For the hadron barrel calorimeter the top figure is for the r-z view and the bottom figure is for the cross section of one module in r-ϕ plane.

the wire and the wire spacing are the same as those in the barrel part. But the wires in the hadron endcap calorimeter are strung horizontally. At both upper and lower sides of the active detector, pads are installed. The outer pads are divided, typically 500 mm×500 mm by the cell wall. Some of pads at the outer sides of the streamer tubes are grouped. These groups are called 'tower'. This hadron calorimeter system is divided into 48 bins in the ϕ direction ($\sim$7.5° each) and 21 bins in the θ direction. The pads at the other side have no cell wall. But, pads have the gas envelope with 4 mm wide aluminum strip for full length of the cell. The strips are put on the center of the wire.

The mixed gas used in these tubes has a composition of isobutane (75%) and argon (25%), which is mixed at the ground and transferred to this subdetector in the underground.

The energy resolution of these subdetectors was investigated by the beam test. The obtained energy resolution is $120\%/\sqrt{E}$ for both subdetectors.

In table 3.14, the properties of the hadron barrel calorimeter and the hadron endcap calorimeter are summarized.

b) Hadron Pole Tip Calorimeters

The hadron pole tip calorimeter is located behind the electromagnetic endcap calorimeter at both endcap regions. The angular coverage of this subdetector is $0.91 < |\cos\theta| < 0.99$. One module has 11 layers of iron slabs and 10 active chambers between each slab. In figure 3.24, the layout of the hadron pole tip calorimeter is shown. And the cross section of a cell of this subdetector is shown in figure 3.25.

The active chambers in this subdetector are the thin high gain multiwire chambers. The wires whose diameter is 50 μm are spread along the radial direction and the wire spacing is 2 mm. The used mixed gas consists of 45% n-pentane and 55% CO_2. The applied the high voltage is 3.5 kV and these chambers are operating in a high gain mode. Each chamber has

		Barrel	Endcap
Angular coverage,$\lvert\cos\theta\rvert$		< 0.81	0.81 – 0.91
Active detector		Limited streamer tubes, cells 9 mm × 9 mm every 10 mm 1.4 – 10 m long	
Number of layers of detector		9	8
High voltage		4.65 – 4.85 kV	
Gas		isobutane (75%), argon (25%)	
Wire spacing		10 mm	
Wire diameter		100 μm	
Readout	tower	pulse height	
	strips	digital	
Absorber (between layers)		100 mm iron	
Gap in iron		25 mm	35 mm
Dimensions	radius	3.4 – 4.4 m	1.9 – 3.3 m
	length	10 m	1.0 m
	thickness of iron	0.8 m	0.7 m
Energy resolution		$120\%/\sqrt{E}$	$120\%/\sqrt{E}$
Strips		axial	horizontal
Towers (pointing to vertex)		$\delta\phi \sim 7.5^\circ$	$\delta\phi \sim 7.5^\circ$
		$\delta\theta \sim 5^\circ$	$\delta\theta \sim 5^\circ$
Trigger		92 analogue signals from groups of 4×4 towers	

Table 3.14: The summary of properties of the hadron barrel calorimeter and the hadron endcap calorimeter

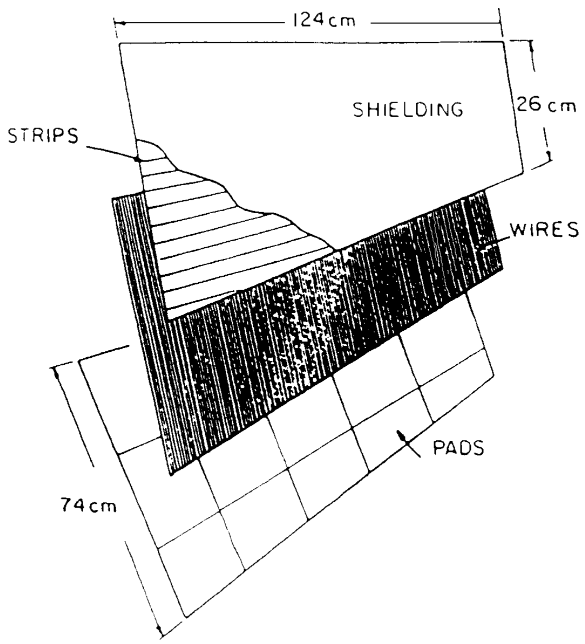

Figure 3.24: The layout of the hadron pole tip calorimeter.

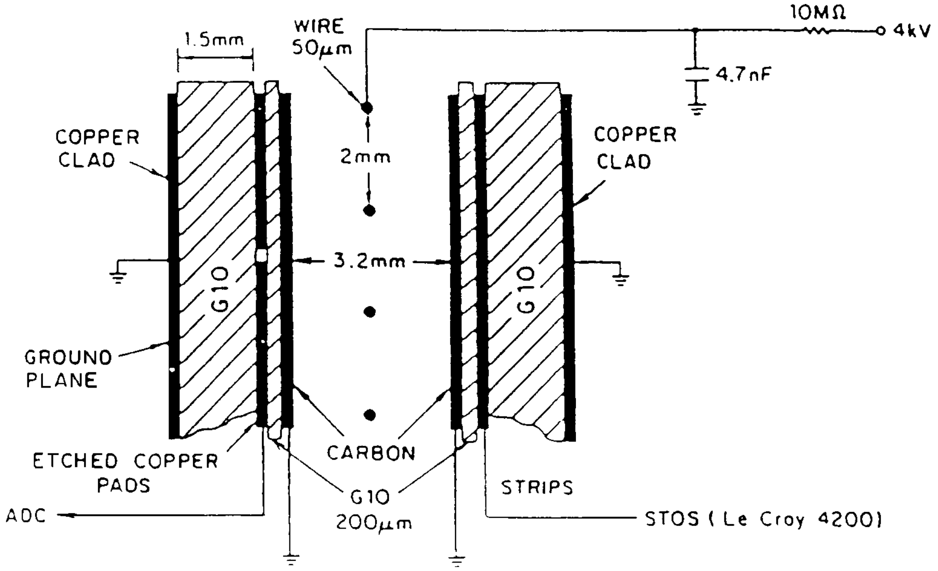

Figure 3.25: The cross section of a cell of the hadron pole tip calorimeter.

pads on one side and strips on the other side. The pad size is typically 500 cm^2. The two sizes of the chamber are adopted, one is 0.61 m^2 with 13 pads and 32 strips and the other is 0.47 m^2 with 8 pads and 28 strips.

The energy resolution was investigated using 6-50 GeV hadron beams at CERN. The obtained energy resolution is $100\%/\sqrt{E}$, where E is in GeV, in the case of no material in front of this subdetector for $E <\sim 15$ GeV. For higher energy region , the energy resolution is $120\%/\sqrt{E}$ due to the leakage of particles from the back of this subdetector.

In table 3.15, the properties of the hadron pole tip calorimeter are summarized.

Angular coverage,$\lvert\cos\theta\rvert$		0.91 – 0.99
Active detector		Thin high gain multiwire chambers
Number of layers of detector		10
High voltage		3.5 kV
Gas		n-pentane (45%), CO_2 (55%)
Wire spacing		2 mm
Wire diameter		50 μm
Readout	tower	pulse height
	strips	digital
Absorber (between layers)		80 mm iron
Gap in iron		10 mm
Dimensions	radius	0.6 – 1.8 m
	length	0.81 m
	thickness of iron	0.72 m
Energy resolution		$120\%/\sqrt{E}$
Strips		radial
Towers (pointing to vertex)		$\delta\phi \sim 11^\circ$
		$\delta\theta \sim 4^\circ$
Trigger		92 analogue signals from groups of 4×4 towers

Table 3.15: The summary of properties of the hadron pole tip calorimeter

3.2.7 Muon Chamber System

The muon chamber system is installed at the most outside of the OPAL detector to identify muons penetrating through the hadron calorimeter systems. This absorber is 1.3 m thick iron corresponding to over 7 interaction lengths for pions. The absorption length in front of the muon chamber system is shown as a function of $\cos\theta$ in figure 3.26. Since the probability of pions penetrating this absorber is very small, muons can be detected very clearly. This system covers 93% of 4π. The geometrical acceptance as a function of $\cos\theta$ is shown in figure 3.27. This system has a very good acceptance over all the geometrical regions.

Basically, muons are identified by the matching between the hits in the muon chamber and the extrapolation of the track measured in the central jet chamber. Details are described in 4.3.2

a) Barrel Muon Chamber

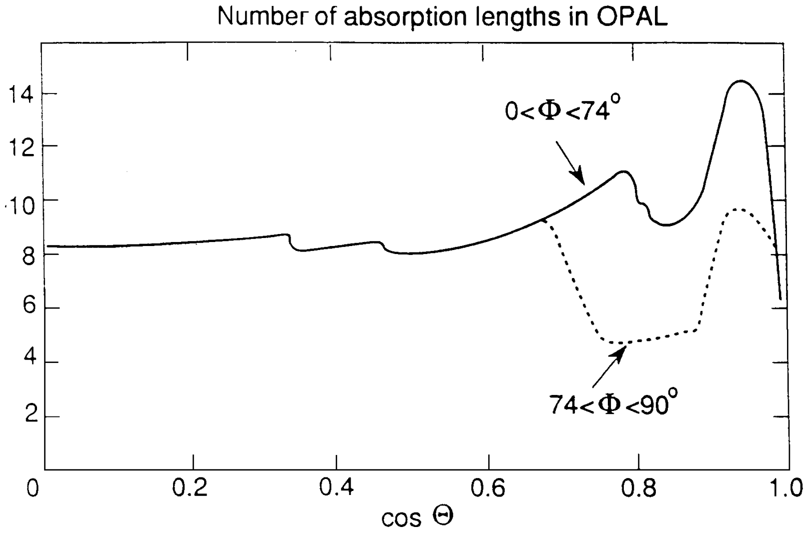

Figure 3.26: The absorption length in front of the muon chamber system as a function of $\cos\theta$.

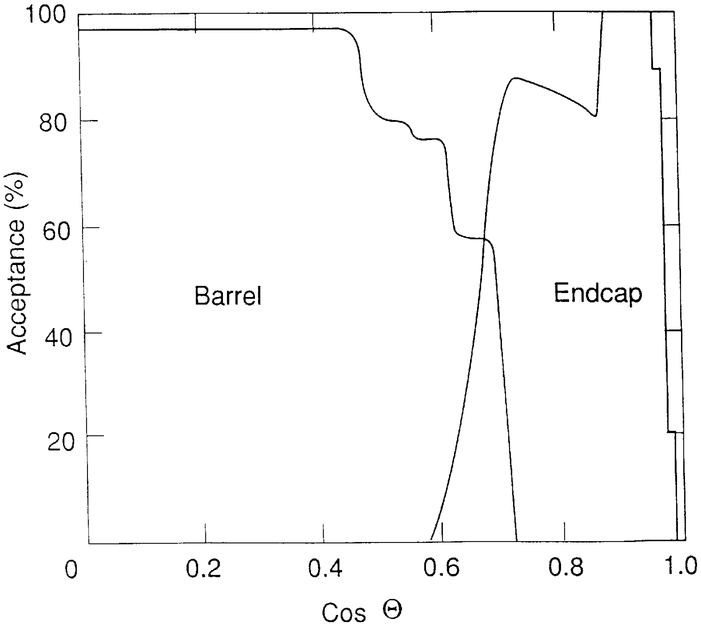

Figure 3.27: The geometrical acceptance for muon chamber system as a function of $\cos\theta$.

The barrel muon chamber is located at about 5 m from the beam pipe and at both top and bottom of the OPAL detector. This subdetector has four layers of drift chambers, each of which is 1.2 m wide and 90 mm thick. These layers are staggered by typically 50 mm in the ϕ direction to remove the left-right ambiguity. In figure 3.28, the layout of the barrel muon chamber is shown.

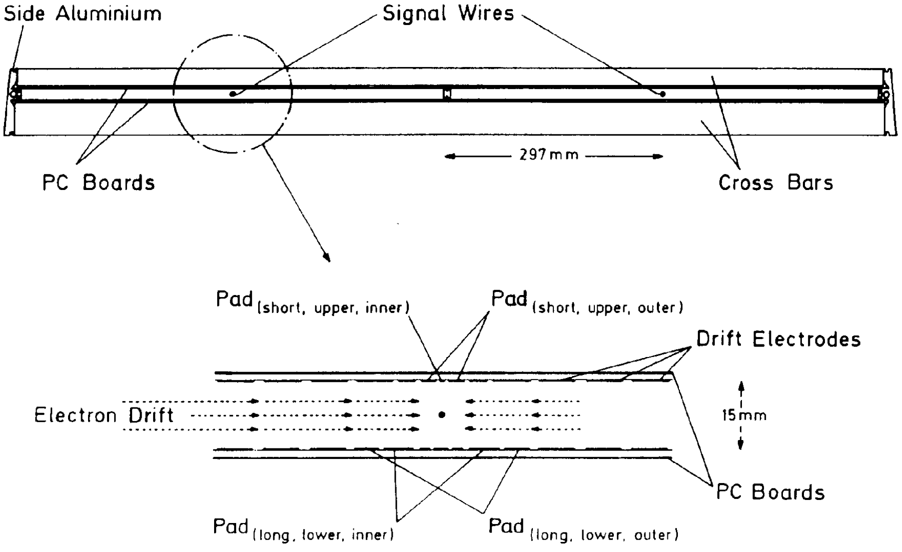

Figure 3.28: The layout of the barrel muon chamber.

Each muon chamber has two sense wires. The sense wire, whose radius is 50 μm, is strung along the z direction and is kept ground. The maximum drift length is 297 mm. By measuring the drift time, the position in the ϕ direction is measured. The spatial resolution in the ϕ direction is 1.5 mm. On the other hand, 'diamond-shaped' cathode pad [59], which is shown in figure 3.29, is used to measure the z position. There are two types of shapes, one has an iteration length of 171 mm and the other 1710 mm. These cycles are used to determine the z coordinate. From this configuration, three kinds of the z coordinate, fine z, medium z and coarse z, are obtained. By using the shorter cycle pad, the fine z coordinates are measured locally. The spatial resolution in z direction from this measurement is 2.0 mm which is 0.02% of 10 m. The medium z coordinate are obtained by using the longer pad and its spatial resolution is 30 mm. And the coarse z coordinate are measured by information of the pulse heights and the timing obtained from both ends of the wire. Information obtained from medium and coarse z measurements remove the periodic ambiguity of z-coordinate measurement obtained from fine z measurement [59, 60]. The fine z is used to calibrate the medium z coordinate and the medium z coordinate is used to calibrate the coarse z coordinate.

The gas in this subdetector is a mixture of ethane (10%) and argon (90%) and is flown by 200 mℓ per one minute. They are controlled by the computer system which is specially developed for this subdetector.

In table 3.16, the properties of the barrel muon chamber are summarized.

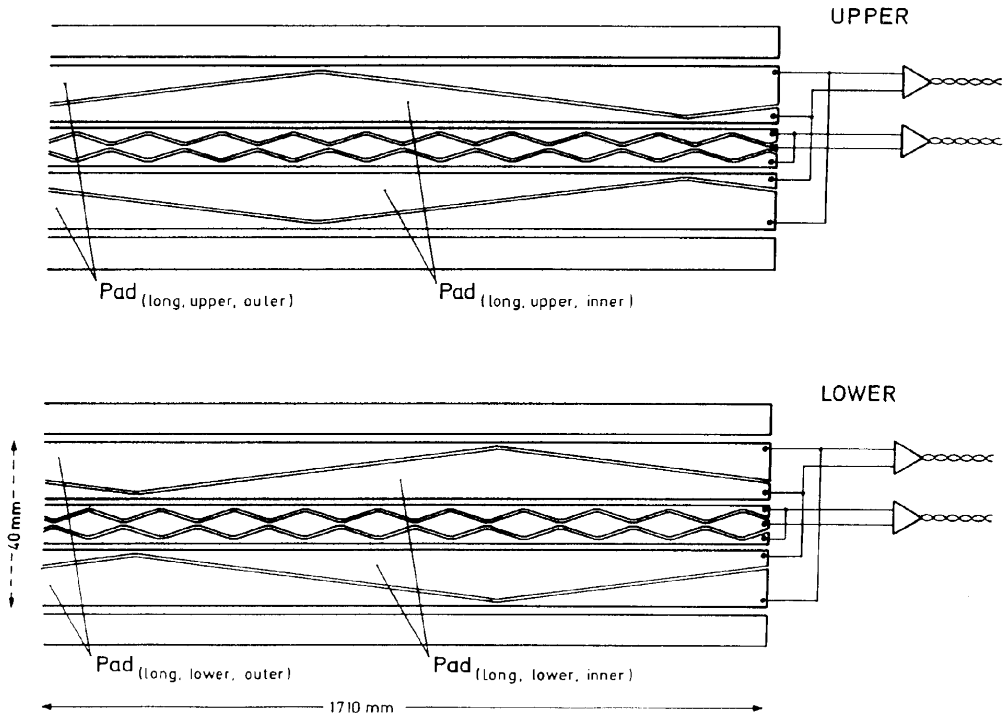

Figure 3.29: The 'diamond-shaped' cathode pad in the barrel muon chamber. The top figure is for the cathode pad at the upper side and the bottom figure is for one at the lower side.

Angular coverage, $\lvert\cos\theta\rvert$	$<$0.72 for $\geq$1 layer $<$0.68 for 4 layers
Absorber, $\lambda_{\rm int}$	$\sim$8
Active detector	110 drift chambers, 1.2 m wide, with 2 wires per chamber drift distance: 0.3 m length: 10.4, 8.4, 6.0 m
Wire direction	along z
Wire diameter	50 μm
Number of layers	4
Spacing	equally spaced over 0.6 m
Area covered	cylinder: 10 m long, 5 m radius
Resolution – position	$\sim$1.5 mm by drift time (ϕ) $\sim$2 mm by cathode pads (z)
Resolution – direction	5 mrad
High voltage	drift: 4.0 kV drift + signal: 5.85 kV
Gas	ethane (10%), argon (90%)
Readout	6 FADCs per wire: both ends of a wire and 4 cathode pads
Trigger	24 ϕ sector signal (any 3 of 4 layer)

Table 3.16: The summary of properties for the barrel muon chamber.

b) Endcap Muon Chamber

The endcap muon chamber is located at both sides of the OPAL detector and its angular coverage is $\sim 0.67 < \lvert\cos\theta\rvert < \sim 0.985$. This subdetector for each side consists of two sets of planes, each of which is constructed by four large square chambers (6 m × 6 m) and two patch chambers (3 m × 2.5 m). The patch chambers are needed due to the existence of the beam pipe, magnet supplies and the cables which are connected to other subdetectors. Each chamber has two layers of limited streamer tubes. The distance between two layers in one chamber is 19 mm and the distance between two planes is 670 mm. In figure 3.30, the layout of the endcap muon chamber is shown.

The basic limited streamer tube, whose schematic view is shown in figure 3.31, is the square tube and the inner cross section is 9 mm × 9 mm. One sense wire, whose diameter is 100 μm, is strung in the center of each tube, so that a wire spacing is 10 mm. The wires are strung horizontally in one layer and vertically in the other layer. By information obtained from each layer, the x and y coordinates can be given. The cathode pads with 8 mm width are put on the inner wall of the tube. The gap between each pad is 2 mm due to the wall of the tubes. The gas which is filled in the tube is the mixture of isobutane (75%) and argon (25%). Since there are two planes with two layers of the limited streamer tubes, the inefficiency due to the wall of the tubes can be removed.

The strips perpendicular and parallel to wires give the spatial resolution of 1 mm and 3 mm respectively.

In table 3.17, the properties of the endcap muon chamber are summarized.

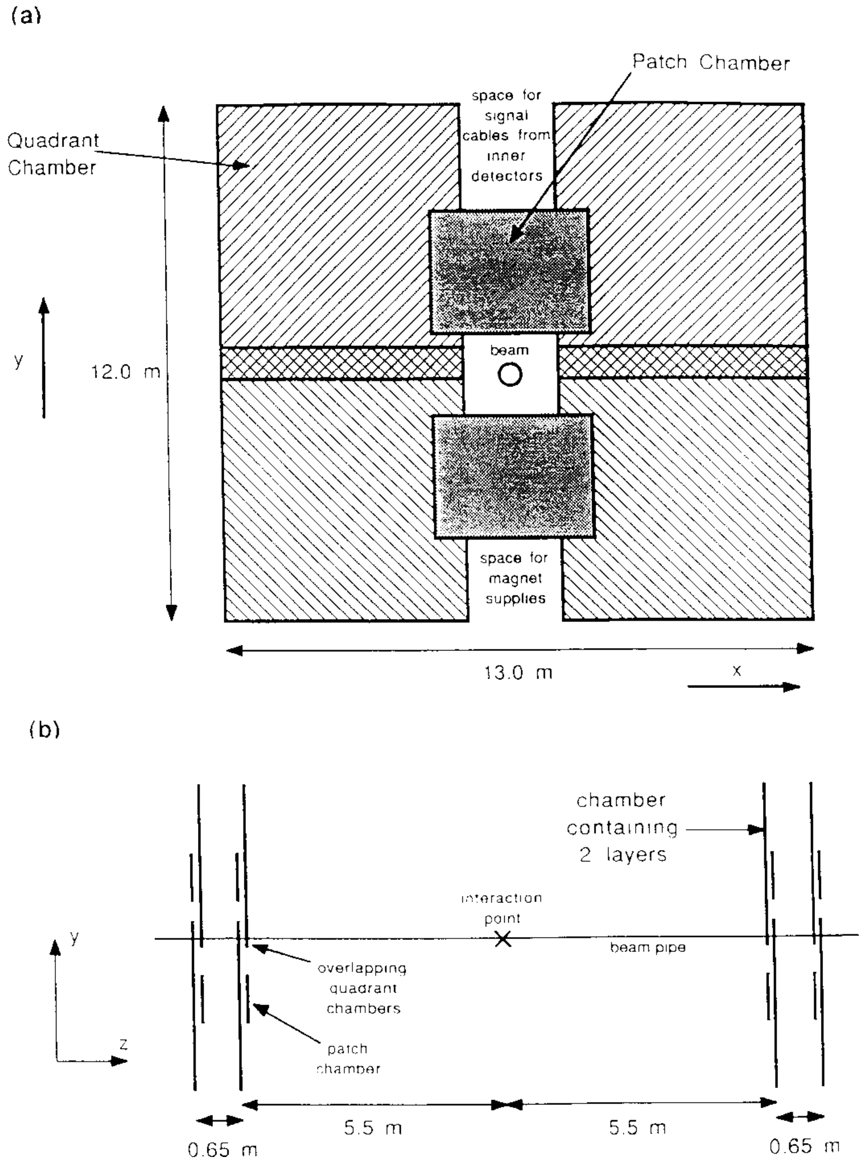

Figure 3.30: The layout of the endcap muon chamber. (a) is a r-ϕ view and (b) is a schematic layout for the endcap muon chamber.

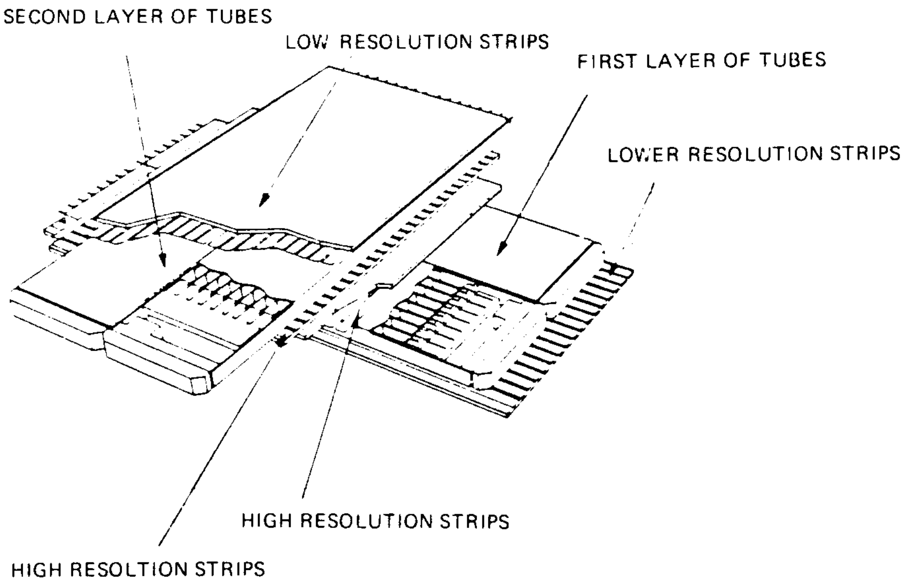

Figure 3.31: The schematic view of the limited streamer tube in the endcap muon chamber.

Angular coverage, $\lvert\cos\theta\rvert$	0.67 – 0.98
Absorber, λ_{int}	8 – 14
Active detector	Limited streamer tubes, with 9 mm × 9 mm cells every 10 mm length: 6, 3 m
Wire direction	along x and y
Wire diameter	100 μm
Number of layers	4
Spacing	19.670, 19 mm
Area covered	12 m × 12 m at each end
Resolution – position	$\sim$1 mm $x(y)$ by $\perp$ strips $\sim$3 mm $y(x)$ by $\parallel$ strips
Resolution – direction	5 mrad
High voltage	4.3 kV
Gas	isobutane (75%), argon (25%)
Readout	pulse height from orthogonal strip (10 mm repeat) from both sides of 4 layers
Trigger	θ – ϕ bins (any 2 of 4 layer)

Table 3.17: The summary of properties for the endcap muon chamber.

3.2.8 Luminosity Monitoring System

The luminosity monitoring system is installed to measure the absolute LEP machine luminosity, where the cross section of elastic scattering $e^+e^- \rightarrow e^+e^-$ is measured at very small angle regions. It is very important to know this value very precisely, because this value is needed when the cross sections of Z^0 decays and the Z^0 line shape are studied. At the first stage, the OPAL detector has only one subdetector, the forward detector, as a luminosity monitor. Now, about two million multihadronic events have been recorded using the OPAL detector and the systematic error is a dominant error on the measurement of the Z^0 line shape. This systematic error includes the uncertainty of the luminosity measurement. The uncertainty of the incident position of scattered electrons and positrons by small angle Bhabha events contributes to the systematic error on the luminosity measurement. Thus, in order to improve the luminosity measurement, the silicon tungsten luminosity monitor was installed during the shutdown between 1992 and 1993. By this subdetector, the Z^0 line shape can be measured with the precision of 0.1%.

And, this system is used not only for the measurement of the machine luminosity but also for the tagging or rejecting electrons from the $\gamma\gamma$ reaction. Therefore this subdetector is very useful also for the study of the two-photon physics.

a) Forward Detector

The forward detector is installed in both endcap regions at inner side of the endcap electromagnetic calorimeter, between 2 m and 3 m from the interaction point along the beam pipe. This subdetector is made of 7 components; i.e., calorimeter and presampler, tube chamber, drift chamber, fine luminosity monitor, gamma catcher and far forward detector. These components cover from 47 mrad to 120 mrad in the θ direction. In figure 3.32, the cross section of the forward detector is shown. But the silicon tungsten luminosity monitor is not drawn in figure 3.32. And the schematic view of this subdetector is shown in figure 3.33.

a-1) Main Calorimeter and Presampler

The calorimeter as a part of the forward detector is installed at the center of the forward detector to measure the energy of the incident electron or positron from small angle Bhabha scattering. This calorimeter consists of 35 layers of lead-scintillator sandwiches, which corresponds to 24 radiation lengths ($24X_0$). In front of this calorimeter, the presampler with 4 radiation lengths ($4X_0$) is installed. These components are divided into 16 segments each. The energy resolution was investigated by using well-contained Bhabha events. The obtained energy resolution is $17\%/\sqrt{E}$ (E in GeV). The cross section of Bhabha scattering for this acceptance region is about 57 nb.

a-2) Tube Chamber

The tube chamber [61] is installed between the presampler and the main calorimeter. The aim of this component is the position measurement of the incident electron (positron). The position resolution is investigated by using information from the drift chamber in front of the calorimeter. The measured shower position resolution is 3 mm.

a-3) Drift Chamber

Two layers of drift chambers [62] are installed in front of the calorimeter to measure the incident position of the electron (positron) from small angle Bhabha scattering. The wires are strung along the radial direction. And a 'diamond shape' pad [59] is adopted as a cathode pad. The decision of the coordinate in the r direction is performed by the measurement of

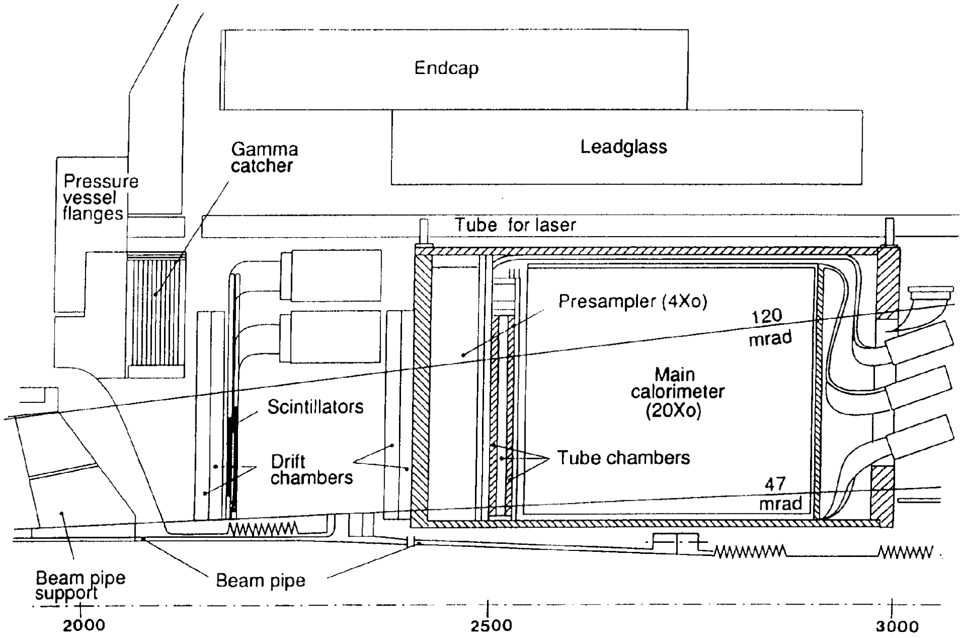

Figure 3.32: The cross section of the forward detector. (N.B. The silicon tungsten luminosity monitor is not drawn in this figure.)

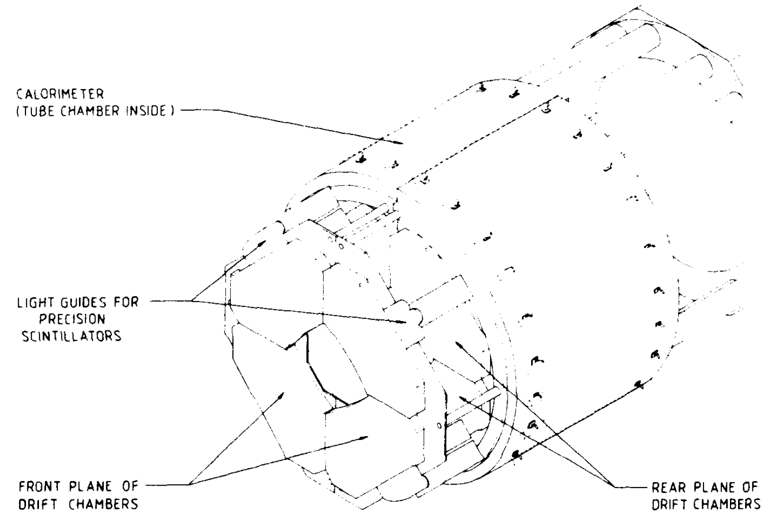

Figure 3.33: The schematic view of the forward detector.

the drift time. For the decision of the position along a wire, the charge division technique is adopted. The spatial resolution is studied by using the test beam and the cosmic rays. The spatial resolution in the r direction is 300 μm and 1 mm in the azimuth direction is combining information from sense wires and pads.

a-4) Fine Luminosity Monitor

The fine luminosity monitor is installed behind the first layer of the drift chamber. This component is made of four pairs of 6 mm thick scintillators, which cover 36% of the acceptable azimuth region. The schematic view of the fine luminosity monitor is shown in figure 3.34. These parts are supported by a honeycomb plate. The cross section of Bhabha scattering for this acceptable region is about 7 nb at Z^0 pole.

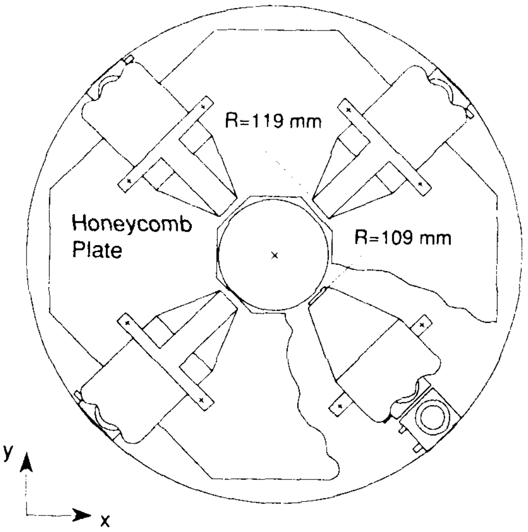

Figure 3.34: The schematic view of the fine luminosity monitor.

a-5) Gamma Catcher

The gamma catcher is installed in front of the calorimeter and outside of the drift chamber. This component has a ring structure and this detector is constructed by the lead-scintillator sandwich with 7 radiation lengths ($7X_0$). This component can tag the electrons and photons with energies greater than 2 GeV. Therefore, this detector can be used to tag the photon from the initial state radiation like $e^+e^- \rightarrow Z^0\gamma$ events.

a-6) Far Forward Detector

The far forward detector is installed at 7.87 m from the interaction point along the beam pipe. This component is made of lead-scintillator sandwich (50 mm × 150 mm) with 20 radiation lengths ($20X_0$). This component provides information on the energy of the electrons (positrons) from very small Bhabha scattering between 5 and 10 mrad. The effective cross section of Bhabha events for this component is about 460 nb.

b) Silicon Tungsten Luminosity Monitor

The silicon tungsten luminosity monitor was installed in the period of the shutdown during 1992 and 1993 to improve the measurement of the machine luminosity as described before.

This subdetector is made of the calorimeter, which has 19 layers of active silicon detectors and 18 tungsten layers. Inner 14 tungsten layers are put on every one radiation lengths (3.8 mm) and outer 4 tungsten layers are put on every two radiation lengths (7.6 mm). The first layer is useful to measure the r coordinate for the incident electrons and photons. Information on the ϕ coordinate is obtained by using information from latter layers.

The calorimeters are installed at ± 238.94 cm along the beam axis from the interaction point and cover the range of $\sim$25 to $\sim$50 mrad. The fiducial region is from 30 to 55 mrad. Each calorimeter is divided into 16 wedges in the ϕ direction. The layout of a wedge is shown in figure 3.35. The detector wedge is a 300 μm thick of silicon and the sensitive region is from 6.2005 cm to 14.2005 cm in the r direction. This wedge is glued to the 275 μm thick ceramic piece which is slightly larger than a silicon wedge. There are four readout electronics including the Amplex$^{\mathrm{TM}}$ chips on this ceramic piece. One wedge has 64 pads (32 segments in the r direction and 2 segments in the ϕ direction).

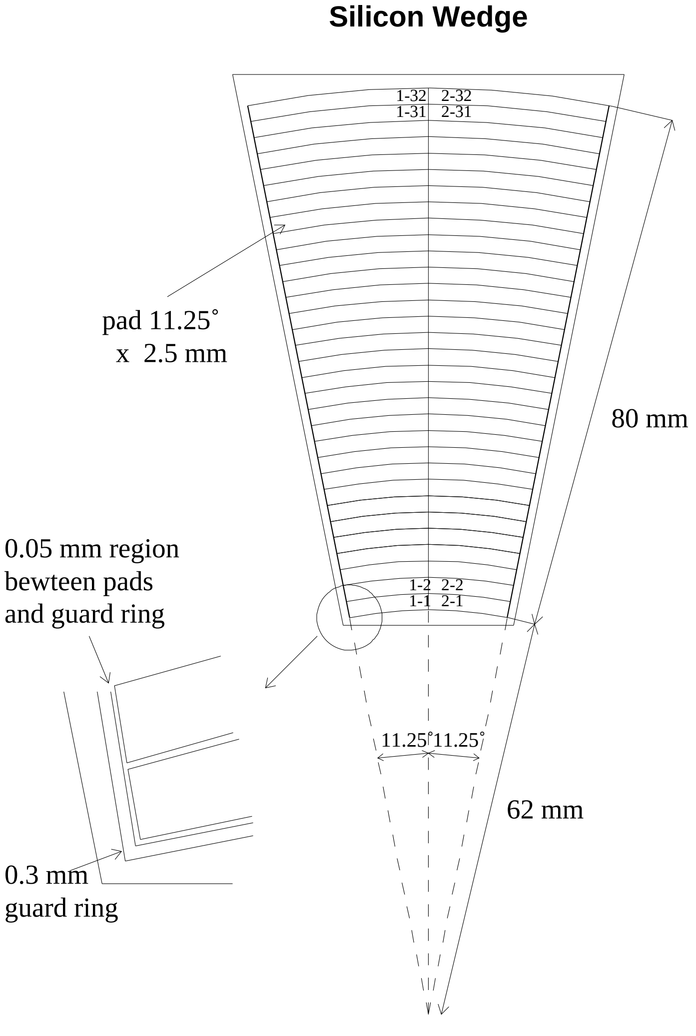
Silicon Wedge

Figure 3.35: The layout of a wedge for the silicon tungsten luminosity monitor.

The cross section of Bhabha scatterings in the small angle region has a dependence of $\sim \theta^{-3}$. The systematic uncertainty of the inner layer is $\sim$25 μm. This means that the precision of the luminosity measurement is expected to be 0.1%.

3.2.9 The Trigger System

The trigger system [63] of the OPAL detector is constructed so as to take data with a high efficiency and a high background rejection power for all event types. The electron and positron bunches collide every 22.2 μsec for four bunches, corresponding to about 45 kHz. The beam collision time can be known by using the pickup signal, which is offered by the instrument mounted around the beam pipe at both sides of the OPAL detector. The event rate should be reduced to the level (1–5 Hz), at which the data taking can be performed without significant deadtime.

The trigger system is needed in order to initiate the data recording. This system has to provide a good efficiency for all physical events and reject the background events like beam-wall interaction, beam-gas interaction and cosmic ray events. And this system have to be constructed so as to provide the trigger signals redundantly. This requirement allows the study on the trigger efficiency and keeps the high trigger efficiency.

In order to make trigger signals, the whole solid angle covered by the OPAL detector is divided into 144 overlapped bins, which are 6 bins in the θ direction and 24 bins in the ϕ direction, as summarized in table 3.18. Tracks and clusters are assigned to the corresponding bins and the signals are digitized in each bin. By digitizing in this small bin the threshold on the energy trigger can be set much lower. On the other hand, the 'stand-alone' trigger information like an energy sum and a number of tracks is also provided from the subdetector trigger. The trigger signals from each subdetector, which are clustered in the ϕ direction as shown in table 3.19, are sent to the central logic system and combined there. The overview of the θ-ϕ matrix on the trigger system is shown in figure 3.36. Finally, several trigger signals are provided by combining some of them.

Theta bin	$\cos\theta$ range			Phi bin	ϕ range [deg]		
1	-0.980	–	-0.596	1	0	–	30
2	-0.823	–	-0.213	2	15	–	45
3	-0.596	–	0.213	3	30	–	60
4	-0.213	–	0.596	-		–	
5	0.213	–	0.823	23	330	–	360
6	0.596	–	0.980	24	345	–	15

Table 3.18: The segmentation for OPAL trigger system.

The Track Trigger is provided by the vertex chamber and the jet chamber. The tracks are recognized in r-z plane. First, four rings with 12 adjacent wires are used to make this trigger signal. One of them is constructed by the axial wires in the vertex detector and the others are constructed by the wires in the jet chamber and the radius of these rings can be varied. The inner, middle and outer rings in the jet chamber cover $|\cos\theta| < 0.97$, $|\cos\theta| < 0.93$ and $|\cos\theta| < 0.82$ respectively. For each wire in each ring the value of z/r is calculated, where z is the z-coordinate obtained from these tracking detectors and r is the radius of the wire position. For each ring, these values are filled into a histogram with 32 bins. In case the number of entries in one bin is greater than the given threshold number, the existence of a track is recognized.

The track trigger is available for the region, $|\cos\theta| < 0.95$. The 'barrel track' is defined as a track contained well in the third ring, corresponding to the region, $|\cos\theta| < 0.82$. This track trigger logic provides the 144 θ-ϕ signals and the 6 stand-alone signals, which are $\geq$ 1,2,3 barrel

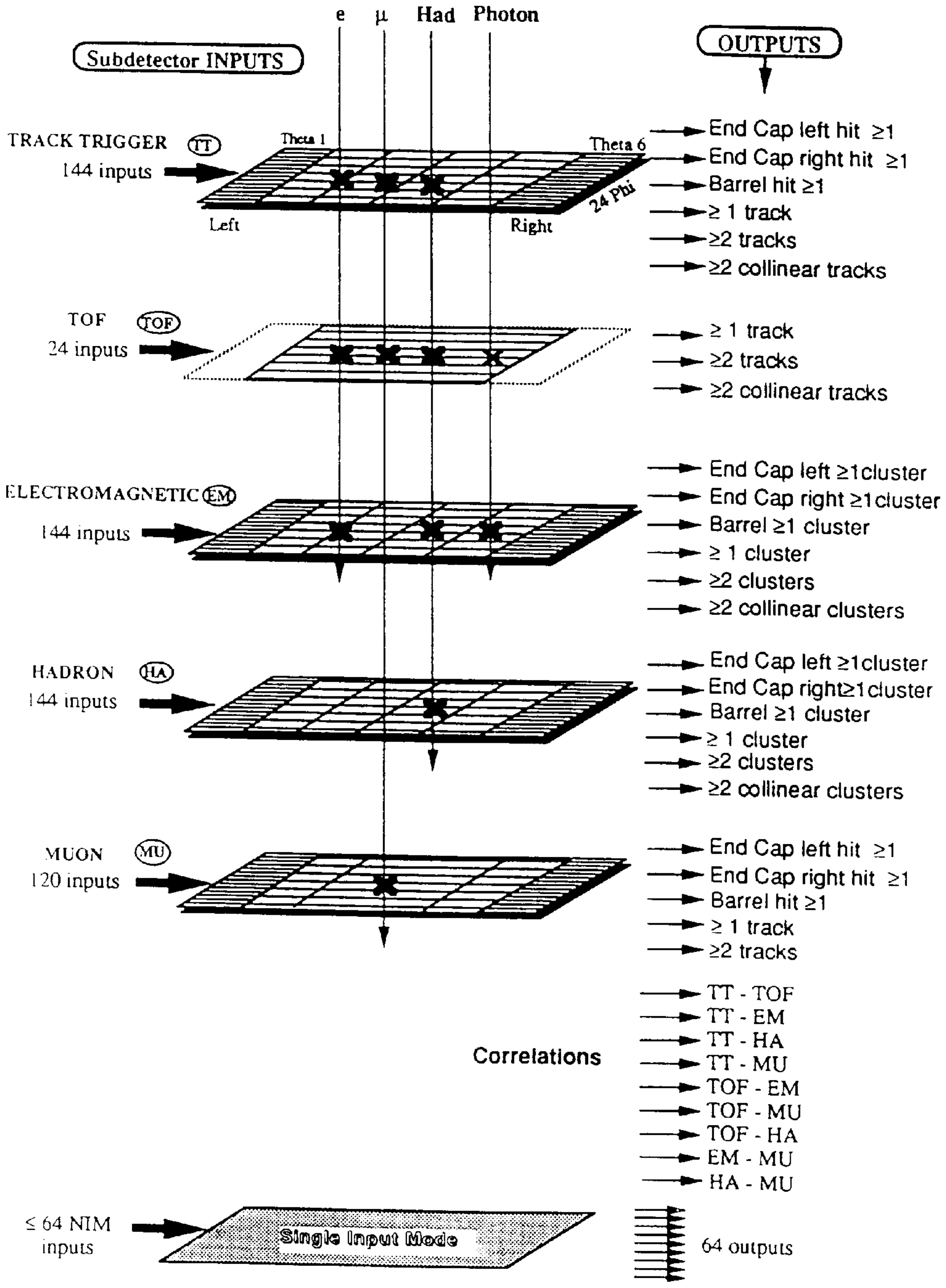

Figure 3.36: The overview of the θ-ϕ matrix on the trigger system.

Subdetector	ϕ_0	ϕ width	Number of bins
Track trigger	0°	30°	12
	15°	30°	12
Time-of-flight	0°	36°	1
and	9°	36°	1
Electromagnetic barrel	27°	36°	1
	The above pattern is repeated 7 more times, at 45°, 90°, 135°, 180°, 225°, 270° and 315°		
Electromagnetic endcap [left]	+2°	30°	12
	+17°	30°	12
Electromagnetic endcap [right]	-2°	30°	12
	+13°	30°	12
Hadron barrel	0°	30°	12
Hadron endcap and pole tip	0°	45°	8
Muon barrel	$\sim -3.5^\circ$	$\sim 22^{\circ *}$	24
Muon endcap	$\sim -0^\circ$	$\sim 25^{\circ *}$	24
	*) bins are partially overlapping		

Table 3.19: The segmentation for subdetectors, where ϕ_0 denotes the start point of the ϕ segment.

track(s) and $\geq$ 1,2,3 track(s) in the whole region. The efficiency of this track trigger system is about 98% for the track coming from the interaction region.

The Time-Of-Flight Trigger is provided from the time-of-flight counter. This trigger is based on the coincidence of the signals obtained from each end of the counter within ±50 nsec from the beam collision time. A total of 160 counters are sub-divided into 24 overlapped ϕ sectors each covering 36°. The trigger signal requires that at least 6 sectors have signals or the multiplicity of the time-of-flight counters exceeds the threshold between 2 and 5. The trigger efficiency for minimum ionizing particles is >90% taking into account the geometrical acceptance.

The Electromagnetic Calorimeter Trigger is based on the energy sum measured by the electromagnetic barrel and/or endcap calorimeters. The counters are clustered every about 48 counters and 200 and 24 analogue signals are provided as overlapped θ-ϕ signals for the electromagnetic barrel and each endcap calorimeter respectively. And the total energy is also provided.

For the total energy trigger signal, two kinds of thresholds are imposed. One is the 'high threshold' and the other is the 'low threshold', which are $\geq$5.0 GeV and $\geq$1.8 GeV for the barrel calorimeter and $\geq$2.4 GeV and $\geq$1.6 GeV for the endcap calorimeter respectively. And for the θ-ϕ trigger signal, the threshold is $\geq$1.8 GeV and $\geq$1.6 GeV for the barrel and endcap calorimeter respectively.

The Hadron Calorimeter Trigger is based on the signals obtained from 976 hadron calorimeter towers. These signals are clustered into 12 or 16 groups and 92 trigger signals are generated. These signals are arranged in 9 rings. Two of them are the ring on the hadron endcap calorimeter and the hadron pole tip calorimeter for one endcap region and the others are rings for the hadron barrel calorimeter. These rings are divided into two half rings vertically.

Three threshold levels, E1, E2 and E3, are imposed for trigger signals obtained from each segment, where E1 (= 1 GeV) < E2 < E3. And the signals which exceed the lowest threshold are converted to the 6×24 θ-ϕ signals.

The Muon Chamber Trigger is provided by the muon barrel and endcap detector separately.

For the muon barrel detector, a whole acceptable region is divided into 24ϕ sectors whose width is about 22° with no segmentation along the z direction. In case there are at least three hits out of four layers in one segment, the trigger signal is generated. The trigger efficiency is 95% per track.

The trigger signals from the muon endcap detector are based on information of the summed charge between 64 and 128 adjacent strips. Whole acceptable region is divided into 4×24 θ-ϕ segments. In particular, the segment along the θ direction is divided into two at $|\cos\theta| = 0.823$. If there are at least two hits out of four strips and the track is coming from around interaction point, the trigger signal is provided from the muon endcap detector. The trigger efficiency is about 95% for a single track muon.

The Forward Detector Trigger is based on the energy measured by this subdetector for each side. The trigger signals are provided if the total energy sum from the presampler and the main calorimeter is greater than 15 GeV or the energy summed over three adjacent ϕ segments is greater than 13 GeV. And information from the fine luminosity monitor can be used to create the trigger signals. Combining these signals, the trigger signals satisfying the requirements, like a total energy sum and a back-to-back topology, are provided at the central trigger logic.

In order to study the accidental coincidence, the signal obtained from one side is artificially delayed by four bunch crossings and coincided with that from the other side. The events triggered by this signal provide information on the background due to off-momentum particles and the background contribution to the real data can be estimated. The trigger signals obtained from only one side of this subdetector as described above are provided so as to be able to study the $\gamma\gamma$ physics. The trigger efficiency provided by this subdetector is about 99%.

The trigger efficiencies for several event types are summarized in table 3.20.

Physics channel	$\lvert\cos\theta\rvert$	Efficiency (%)
$e^+e^- \to$ hadrons	<1.0	100
$e^+e^- \to \mu^+\mu^-$	<0.95	99.9 ±0.1
$e^+e^- \to \tau^+\tau^-$	<0.90	99.9 ±0.1
$e^+e^- \to e^+e^-$	<0.85	100
$e^+e^- \to \gamma\gamma$	<0.90	>99.9
Small angle Bhabha	0.989 – 0.999	>99.9

Table 3.20: The summary of trigger efficiencies for several event types.

3.2.10 The Pretrigger System

The electron and positron bunches cross every 22.2 μsec in the case of 4+4 bunches in LEP. To improve the machine luminosity, a number of bunches for electrons and positrons was increased to 8+8 bunches in LEP, so the beam collision frequency became to about 90 kHz. The pretrigger system, which is almost deadtime-free, is needed in this new experimental condition. The pretrigger system was adopted in 1992 and the OPAL detector has a two-stage trigger system. In figure 3.37, the overview of the two-stage trigger system is illustrated.

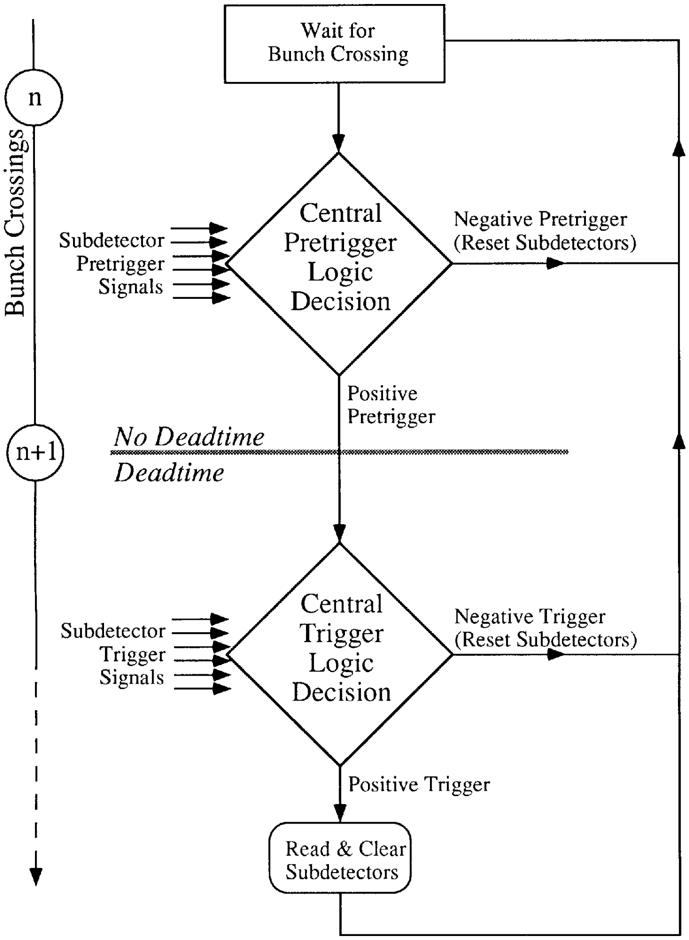

Figure 3.37: The overview of the OPAL two-stage trigger system.

This pretrigger system is designed so as to improve the efficiency and acceptance for all the event types, and this system should be operational even for a single track event. But the pretrigger rate should be kept low because the high pretrigger rate prevents progress on the 'main' trigger system. The pretrigger signals are provided from the vertex chamber, the jet chamber, the time-of-flight counter, both electromagnetic barrel and endcap calorimeters and the muon endcap chamber. The forward detector also provides the pretrigger signal. The hadron calorimeters and the muon barrel calorimeter do not provide the pretrigger signal because the drift time is long. The pretrigger signals, however, are provided in a solid angle of nearly 4π. The subdetectors which provide the pretrigger signals are divided into 12 segments with overlapping, each having about 60° coverage in the ϕ direction. This segmentation for the pretrigger system is summarized in table 3.21. And the overview of the ϕ matrix on the OPAL pretrigger system is illustrated in figure 3.38. In order to avoid generating the pretrigger signal due to backgrounds like a synchrotron radiation, the pretrigger signals from each subdetector are coincided in the same ϕ region.

Bin	CV	CJ	TB	EB	EE	ME
1	10– 50	0– 60	0– 54	0– 54	0– 60	0– 60
2	40– 80	30– 90	36– 90	36– 90	30– 90	30– 90
3	70–110	60–120	63–117	54–126	60–120	60–120
4	100–140	90–150	90–144	90–144	90–150	90–150
5	130–170	120–180	126–180	126–180	120–180	120–180
6	160–200	150–210	153–207	144–216	150–210	150–210
7	190–230	180–240	180–234	180–234	180–240	180–240
8	220–260	210–270	216–270	216–270	210–270	210–270
9	250–290	240–300	243–297	234–297	240–300	240–300
10	280–320	270–330	270–324	270–324	270–330	270–330
11	310–350	300–360	306–360	306–360	300–360	300–360
12	340– 20	330– 30	333– 27	324– 27	330– 30	330– 30

Table 3.21: The segmentation for the pretrigger system, where CV, CJ, TB, EB, EE and ME mean the vertex chamber, the jet chamber, the time-of-flight counter, the electromagnetic barrel calorimeter, the electromagnetic endcap calorimeter and the muon endcap detector.

The trigger system of each subdetector was modified in order to accommodate to the pretrigger signals. The upgrades of the muon endcap detector and the time-of-flight counter are very straightforward because the signals obtained from these subdetectors are fast enough to provide the pretrigger signals. The signals from these two subdetectors are reassigned into 12 ϕ bins. The other subdetectors; i.e., the vertex detector, the jet chamber and the electromagnetic calorimeters, were modified as described below.

The pretrigger signal from the vertex chamber is based on the number of hits in a ϕ sector. Four kinds of thresholds (4, 6, 8 or 10 out of 12) are adopted. These thresholds can be changed programably so as to be suitable for the background condition. Thirty-six ϕ sectors are reassigned into 12 segments and each segment provides the pretrigger signal.

The pretrigger signal from the jet chamber is based on a number of hits in the inner ring with 12 adjacent wires, whose definition is described in 3.2.9, in 24 ϕ sectors. As an option, the middle ring is also used. The outer ring is not used because the signals are slow due to

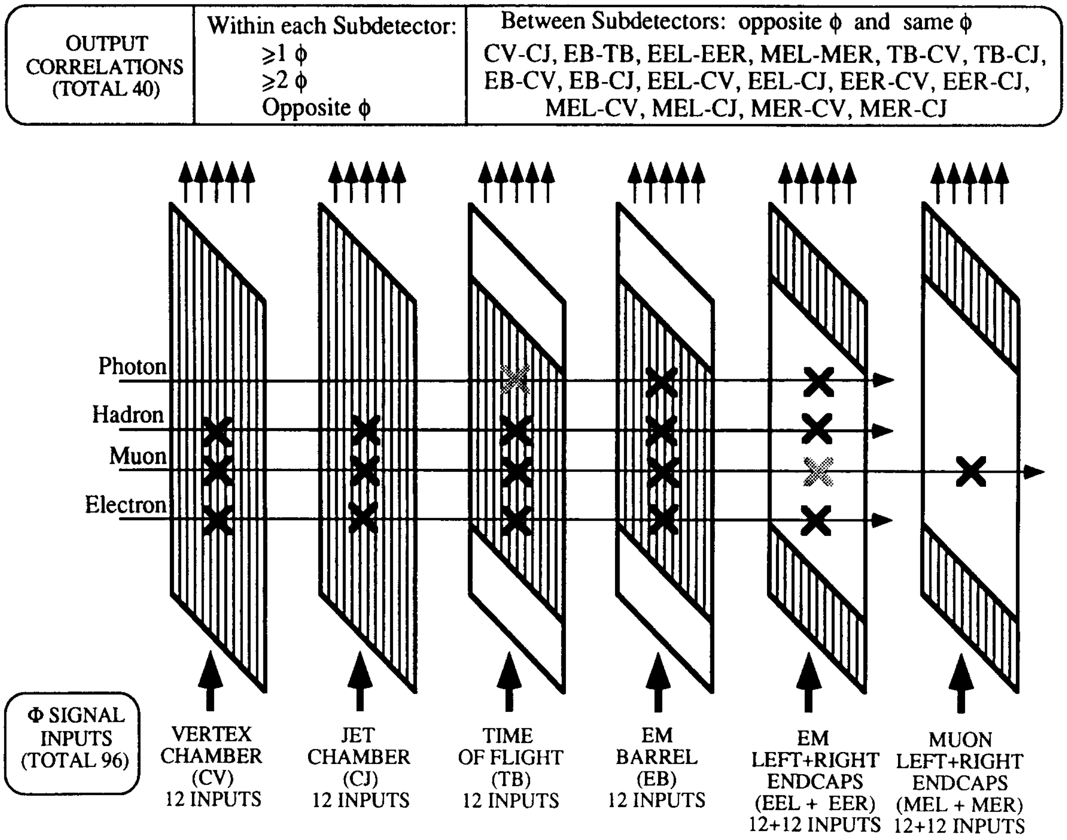

Figure 3.38: The overview of the ϕ matrix on the OPAL pretrigger system.

its long drift time. The pretrigger signal is provided if a number of hits exceeds the adjustable threshold, typically 8 out of 12 wires.

The pretrigger signal from the electromagnetic calorimeter is based on the measured energy summed over 96 adjacent lead glass blocks. This energy summing is performed via two steps. First, the analogue sum for 12 adjacent blocks is performed and this signal is digitized. Next, after imposing the cut for the noise suppression, the digitized energys are summed for 48 and then 96 adjacent lead glass blocks. In the barrel region, the pretrigger signal is provided in case this energy sum exceeds the nominal threshold, 320 MeV.

The pretrigger efficiencies for several event types are summarized in table 3.22. The pretrigger condition in this table has the following meaning;
CV1: Central Vertex chamber ≥ 1 ϕ bins
CV2: Central Vertex chamber ≥ 2 non-adjacent ϕ bins
CJ1: Central Jet chamber ≥ 1 ϕ bin
TB1: Time-of-Flight ≥ 1 ϕ bin
EE1: Electromagnetic Endcap calorimeter ≥ 1 ϕ bin in at least one side of the endcap region
EB1: Electromagnetic Barrel calorimeter ≥ 1 ϕ bins
EB2: Electromagnetic Barrel calorimeter ≥ 2 non-adjacent ϕ bins
EBPHI: Electromagnetic Energy in the barrel region ≥ 320 MeV
ME1: Muon Endcap chamber ≥ 1 ϕ bin in at least one side of the endcap region.

Pretrigger Condition	Acceptance $\lvert\cos\theta\rvert$	Efficiency (%) $(Z^0 \rightarrow q\bar{q})$	$(Z^0 \rightarrow e^+e^-)$	$(Z^0 \rightarrow \mu^+\mu^-)$	$(Z^0 \rightarrow \tau^+\tau^-)$
CJ1	<0.97	100	100	100	100
TB1	<0.82	100	100	98.4 ± 0.2	99.9 ± 0.1
EE1	0.81–0.98	100	100	71.4 ± 1.5	87.5 ± 1.5
ME1	~0.67–~0.98	11.6 ± 0.2	0	92.8 ± 0.1	30.5 ± 2.1
CV2	<0.97	100	100	100	99.9 ± 0.1
EB2	<0.82	100	100	98.4 ± 0.2	99.5 ± 0.1
EBPHI	<0.82	100	100	97.6 ± 0.3	99.9 ± 0.1
CV1.AND.EB1	<0.82	100	100	99.9 ± 0.1	99.9 ± 0.1

Table 3.22: The summary of the pretrigger efficiency for several event types.

3.2.11 Data Acquisition System and Dataflow

The main function of the data acquisition (DAQ) system [64] is taking and storing raw data from the OPAL detector. In figure 3.39, the scheme of this online system is shown. The microprocessors used in the system are of a 68020/68030 type [65] and they are running under the OS9 operating system [66] through the VME bus based system [67]. The signals collected from each subdetector are digitized and sent to "event builder" VME system, where the signals from each subdetector are collected and merged and the events are reconstructed. By checking information at the filter, unphysical events (background processes) are rejected. Meaningful events are transferred to the VME system on the ground and stored on the optical disk.

The lowest layer of the OPAL online system consists of many computers which work for collecting data and making trigger signals at each subdetector in parallel. VME system is adopted

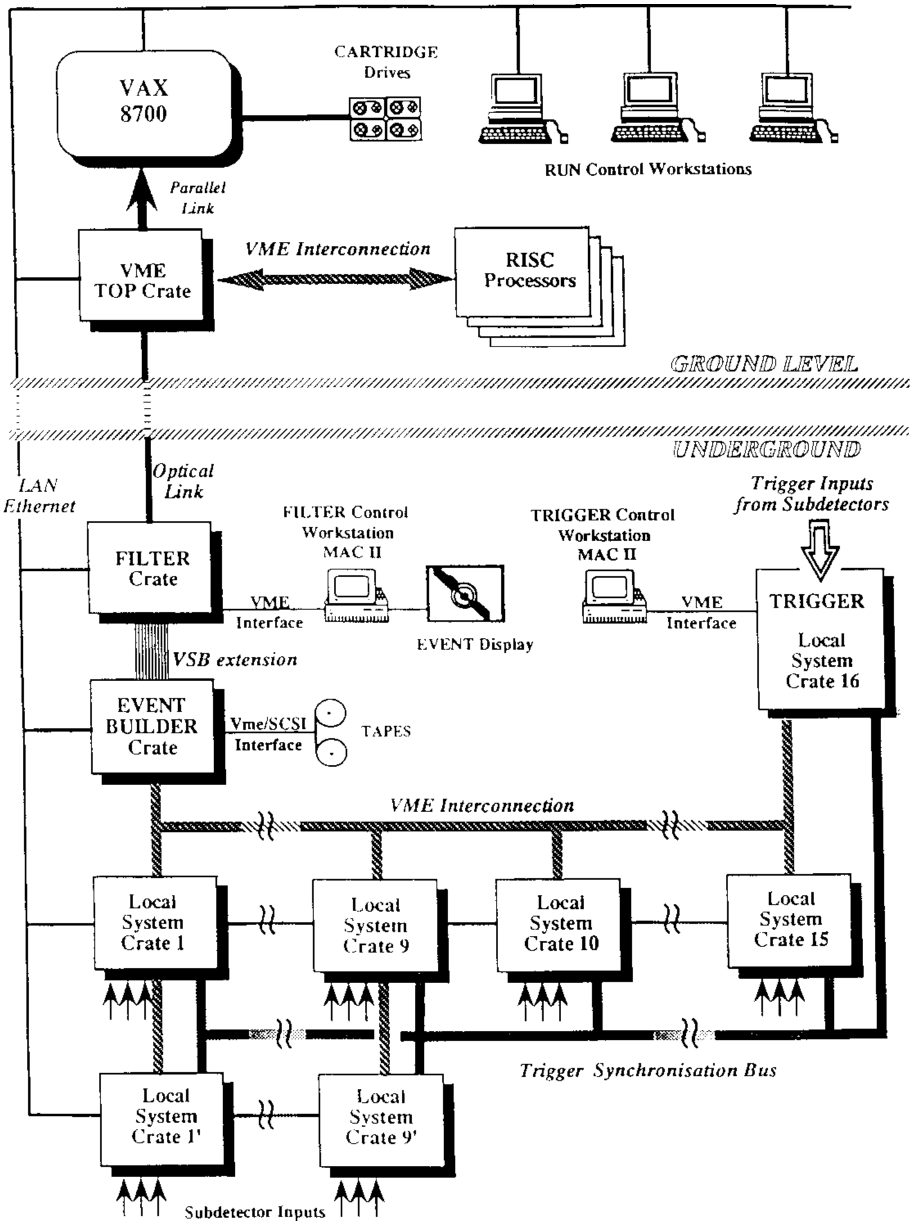

Figure 3.39: The scheme of the OPAL online system.

for these purposes and this system is called the local system crate (LSC). LSC component has at least one single board computer, the hard disk and VME module. VME module is the interface to Ethernet, VICbus and the trigger bus. Each subdetector uses the readout electronics which are suitable for data taking, like VME, FASTBUS, CAMAC and private-designed systems. The signals collected by each electronics described above can be read via VME module in each LSC component. These LSCs work under the OS9 operating system. FORTRAN and C are used as programming languages.

The data collected by LSCs are sent to the event builder. The event builder gathers data and trigger signals, merges them into a full event and transfers the merged data to the 'filter', which is described below. The event builder has a large buffer memory because the data and trigger signals from each LSC can not be sent to the event builder at the same time. This system is controlled by a single OS9 processor. The programming is performed by the object oriented language, C++.

The filter is made of several systems. The main purpose of the filter is to reject the background events such as off-momentum electron collisions with a beam pipe, cosmic ray events and detector noises, accepted by the trigger system in each subdetector. This means that the filter acts as a 'second-level trigger', compared with 'first-level trigger' which is the trigger signal from each subdetector. The events selected by the filter are stored in a large event buffer disk. And the filter provides monitoring and the data processing capability and supports the event display. In order to perform these functions, HP Apollo DN10000 RISC-based workstation is used.

All LSCs, the event builder and the filter are controlled by the central DAQ control system. This central DAQ control system is made of VAX cluster. This system not only controls all DAQ subsystems but also recovers the hardware and software troubles which occasionally happen.

The events stored in the buffer disk are sent to the event reconstruction system. This system converts the raw data into the physical quantities, such as momenta and energies. These data are stored into the optical disk. The advantage of the usage of optical disks is to preserve random access to events. As a bank system of data format, ZEBRA [68] is adopted as a standard format. ZEBRA is developed at CERN to enable to support accessing to data structures. The reconstructed events are available within a few hours after data taking.

Chapter 4

Analysis

4.1 Selection of Multihadronic Events

To extract $Z^0 \rightarrow q\bar{q}$ events efficiently from a lot of collected data, the preselection of multihadronic events was performed. The cuts for selecting them are based on the characteristics of the multihadronic events. The characteristics of $Z^0 \rightarrow q\bar{q}$ events are;

(1) A charged track multiplicity is large.

(2) A number of electromagnetic clusters is large.

(3) A summed momentum of an event along the beam axis is balanced.

The characteristics (1) and (2) are the specific ones for $Z^0 \rightarrow q\bar{q}$ events. A number of charged tracks of $Z^0 \rightarrow e^+e^-, \mu^+\mu^-$ events is typically only two. For $Z^0 \rightarrow \tau^+\tau^-$ events, the charged track multiplicity is relatively low. A number of electromagnetic clusters generated by the $Z^0 \rightarrow \ell^+\ell^-$ events is not so large. Then, if the requirements (1) and (2) are imposed to the data, most of $Z^0 \rightarrow \ell^+\ell^-$ events are rejected and most of $Z^0 \rightarrow q\bar{q}$ events are selected. Some background events, however, are not rejected by these criteria. The main background source passing through the above criteria is the $\gamma\gamma$ collision, so-called two photon process. These $\gamma\gamma \rightarrow q\bar{q}$ events look like $Z^0 \rightarrow q\bar{q}$ events in r-ϕ plane. But the momentum balance along the beam axis is lost because momenta of two photons emitted from an electron and a positron in the initial state are not the same, while $Z^0 \rightarrow q\bar{q}$ events have no large missing energy along the beam axis. And the events such as beam-wall interactions and beam-gas interactions also lose the momentum balance along the beam axis. Thus the background events described above can be rejected by requiring (3). The selection criteria of $Z^0 \rightarrow q\bar{q}$ decays [69] are described below in detail.

At first, 'good' charged tracks and 'good' electromagnetic clusters were defined. 'Good' charged tracks were required to have more than or equal to 20 spatial points in the central jet chamber and the transverse momentum with respect to the beam axis greater than 0.15 GeV/c in order to guarantee a good tracking and a good dE/dx measurement. To remove cosmic rays and unphysical tracks, the momenta of tracks were required to be less than 65.0 GeV/c. In table 4.1, the definitions of the 'good' charged track are summarized.

'Good' electromagnetic clusters were required to have the raw energy, E_{raw}, greater than 0.05 GeV. And the corrected energy was required to be greater than 0.10 GeV with at least one block for the barrel region and 0.20 GeV with at least two blocks for the endcap region. In table 4.2, the definitions of the 'good' electromagnetic clusters are summarized.

Number of hits in the jet chamber	≥ 20
Transverse momentum with respect to the beam axis	> 0.150 GeV/c
$\tan\lambda$ ($= \cot\theta$)	< 100.0
z_0	< 200.0 cm
Momentum	< 65.0 GeV/c
d_0 with respect to the beamspot	< 5.0 cm
χ^2 from the x-y fit	< 100.0

Table 4.1: The definitions for the good charged tracks.

	Barrel	Endcap
Raw Energy	> 0.05 GeV	
Corrected energy	> 0.10 GeV	> 0.20 GeV
Number of blocks	≥ 1	≥ 2

Table 4.2: The definitions for the good electromagnetic clusters

To select multihadron events, it was required that the silicon microvertex detector, the vertex chamber, the jet chamber, the electromagnetic calorimeter and the muon chamber were in good operation. This guarantees a good quality of the data. To reject $Z^0 \to \ell^+\ell^-$ events, the events were required to have more than five good charged tracks and more than seven good clusters. To reject two photon processes, the events were required to satisfy $R_{vis} \geq 0.10$ and $R_{bal} \leq 0.65$. The parameters R_{vis} and R_{bal} are defined as $R_{vis} = E_{shw}/\sqrt{s}$ and $R_{bal} = E_{bal}/E_{shw}$ respectively, where E_{shw} is an energy sum for all good clusters and E_{bal} is a sum of $E_{raw}\cos\theta$ for all good clusters, whose angle θ is defined as the angle between z axis and the electromagnetic cluster. In table 4.3, the selection cuts for the $Z^0 \to q\bar{q}$ events are summarized.

Number of good tracks	> 5
Number of good clusters	> 7
R_{vis}	≥ 0.10
R_{bal}	≤ 0.65

Table 4.3: The summary on the cuts for the $Z^0 \to q\bar{q}$ event selection

These cuts can not perfectly reject $Z^0 \to \tau^+\tau^-$ events in case both τ's decay into three charged particles with some neutral pions. Thus in order to reject τ pair events completely, at least seven charged tracks were required for multihadronic events.

4.2 Monte Carlo Simulation

The Monte Carlo simulation can be divided into two parts; the event generation and the detector simulation. The event generation is the part where physical events are generated according to the theoretical calculations, and the detector simulation is the part where the performances of the OPAL detector are simulated. For the event generator, several generators for $e^+e^- \rightarrow q\bar{q}$ process are available such as JETSET Monte Carlo, HERWIG Monte Carlo and EURODEC Monte Carlo. In this analysis, the JETSET 7.3 [70, 71] is used as an event generator and the GEANT3 is used to simulate the detector responses [72].

The event generator, JETSET 7.3, contains the process $e^+e^- \rightarrow \gamma^*/Z^0 \rightarrow q\bar{q}$, where '*' denotes that the photon is off-mass shell. The $q\bar{q}$ pairs, where q is u, d, s, c, b or t quark, are generated according to the relative coupling. The angular distribution of generated $q\bar{q}$ pairs is also taken into account.

JETSET program includes the initial and final state radiation processes due to higher order QED and QCD. These processes are very important at the high energy region because the event topology is changed due to the photon and/or gluon emissions. Two techniques, matrix element method and parton shower method, are used to calculate the effects due to these processes.

The matrix element method is based on the calculation of the Feynman diagrams including some higher order contributions. This method has a demerit in that it is more difficult to calculate the matrix elements for more higher order processes. Therefore, matrix elements for higher order processes, for example the one loop correction, are not calculated except for the easy case which can be calculated explicitly. For the initial-state QED radiation, the first order process is included in this program and the energy of the emitted photon obeys the non-exponential distribution. For the final-state QCD radiation, the parton shower method, which is described below, is normally used.

The parton shower method is based on the branching processes of $e \rightarrow e\gamma$, $q \rightarrow qg$, $q \rightarrow q\gamma$, $g \rightarrow gg$ and $g \rightarrow q\bar{q}$, which depend on the energy fraction that the daughter particle has. The upper limit on a number of emitted photons/gluons are not actually put because the matrix elements are not calculated. The kinematic parameters and the helicity amplitudes are approximately matched. Therefore, the detail information on the subjet structure and so on is needed for this method.

The fragmentation process is hardly understood yet. There are three types of models on this process; the string fragmentation, the independent fragmentation and the cluster fragmentation. This JETSET program adopts the string fragmentation, which is simulated in the LUND generator.

The 'string' is strung between the quark and the antiquark which are generated by the e^+e^- annihilation process. The energy is stored in this string depending on the distance between the quark and the antiquark. When they separate from each other about 1 fm, which is a typical hadron size, the new quark-antiquark pair is created by the stored energy in this string according to the idea on the quantum tunneling effect and this process is lasted till the stored energy becomes less than the cut-off energy. By this idea, the production ratio of each quark along the string is $u : d : s : c \sim 1 : 1 : 0.3 : 10^{-11}$. The generation of heavy quark pairs is not expected in this process. But the heavy quark pair production process is included in $g \rightarrow q\bar{q}$ process.

This fragmentation is simulated according to the Peterson fragmentation function with a single parameter, ϵ_q [73]. The fragmentation rate to the hadron with x from a quark, q, is written by

$$f(\epsilon_q, x) = \frac{1}{x(1 - \frac{1}{x} - \frac{\epsilon_q}{1-x})^2},$$

where $x = E_{hadron}/E_{available}$ and E_{hadron} is an energy of hadron and $E_{available}$ is an energy available for the fragmentation process after the parton shower. In this Monte Carlo generator,

$\epsilon_b = 0.0057$ and $\epsilon_c = 0.046$ are used, corresponding to the mean energy fraction $\langle x_E \rangle_b = 0.697 \pm 0.013$ for b hadrons [74] and $\langle x_E \rangle_c = 0.51 \pm 0.02$ for charm hadrons [75].

The standard model is used to estimate the partial decay widths of $Z^0 \to q\bar{q}$ [76]. The masses adopted in this Monte Carlo generator are 5.48 GeV/c^2 for B_s mesons and 5.62 GeV/c^2 for Λ_b baryons. The lifetime for all b-flavored hadrons included in this Monte Carlo is ordinarily fixed to 1.4 psec^{-1}. Several experiments report the lifetime measurements on b-flavored hadrons. The lifetimes for each b-flavored hadron are accordingly corrected in order to describe the observed proper time distribution. The corrections are based on the LEP measurements [77] and CDF measurements [78]. The ratios of $\tau_{B^+}/\tau_{B_d} = 1.01 \pm 0.11$, $\tau_{B_s}/\tau_{B_d} = 0.99 \pm 0.18$ and $\tau_{\Lambda_b}/\tau_{B_d} = 0.69 \pm 0.12$ are used. And the average b-flavored hadron lifetime $\langle \tau \rangle = 1.56 \pm 0.02$ psec is used. The b-flavored hadrons are generated according to the fraction, $B^+ : B_d : B_s : \Lambda_b = 39.5 : 39.5 : 12 : 9$. This production fraction is a value from JETSET [79]. The Monte Carlo data used in this analysis include no B mixing. Then the mixing effect is calculated by hand using information on the true proper time of B hadrons.

In table 4.4, these parameters are summarized.

Quantity	Value
$\langle x_E \rangle_b$	0.697 ± 0.013 [82]
$\langle x_E \rangle_c$	0.51 ± 0.02 [81]
$B(b \to \ell)$	$10.5 \pm 0.6 \pm 0.5\%$ [82]
$B(b \to c \to \ell)$	$7.7 \pm 0.4 \pm 0.7\%$ [82]
$B(b \to \bar{c} \to \ell)$	$1.3 \pm 0.5\%$ [70, 71, 82]
$M(B_s)$	5.48 GeV/c^2
$M(\Lambda_b)$	5.62 GeV/c^2
τ_{B^+}/τ_{B_d}	1.01 ± 0.11 [77, 78]
$\tau_{\Lambda_b}/\tau_{B_d}$	0.69 ± 0.12 [77, 78]
τ_{B_s}/τ_{B_d}	0.99 ± 0.18 [77, 78]
$\langle \tau_b \rangle$	1.56 ± 0.02 psec [77]

Table 4.4: The parameters used for the Monte Carlo simulation.

The generated events are passed through the detector simulation and the obtained signals form this simulator are stored in magnetic tapes with the same format as the real data. This detector simulation is based on the program package, GEANT3.

4.2.1 b Quark and Charge Tagging

In order to investigate B^0-$\bar{B}^0$ mixing, $Z^0 \to b\bar{b}$ decays have to be selected from many multi-hadronic decays of Z^0. And the charge of b quark in B hadron has to be known. Two techniques are very popular to tag b quark jets; (1) by tagging the leptons generated by the semileptonic decay of b quark and (2) by reconstructing the secondary vertex of b decays.

By the former technique, the charge of a b quark in B hadron can be known from the charge of the tagged lepton. By semileptonic decay of B hadron, b quark decays into a c quark and a virtual W boson, and the W boson subsequently decays into a lepton and a neutrino. Since a b quark ($\bar{b}$ quark) has a negative (positive) charge, the final lepton has a negative (positive) charge necessarily.

It is easy, in principle, to tag leptons which are generated by the semileptonic decays of b quark. Because b quark has a very large mass (about 5 GeV/c^2) compared with other quarks, the emitted lepton has a high momentum, p, and a high transverse momentum, p_T, with respect to the direction of b quark. In figure 4.1, the predicted momentum distribution and the predicted transverse momentum distribution of leptons coming from b quark decay are shown together with those in c quark decays, which are the main background for this technique. If $p > 2.0$ GeV/c and $p_T > 0.8$ GeV/c are required, most of leptons coming from semileptonic c decays can be rejected and the leptons generated by semileptonic decays of b quark can be obtained with a high purity. The cascade decay of b quark, $b \to c \to \ell$, can not be a main background to the b quark tagging, but can be a serious background in the present oscillation study. If cascade decay leptons are tagged, the sign of the tagged lepton is not the same as that of a b quark in B meson and the cascade decay can fake the B^0-$\bar{B}^0$ oscillation.

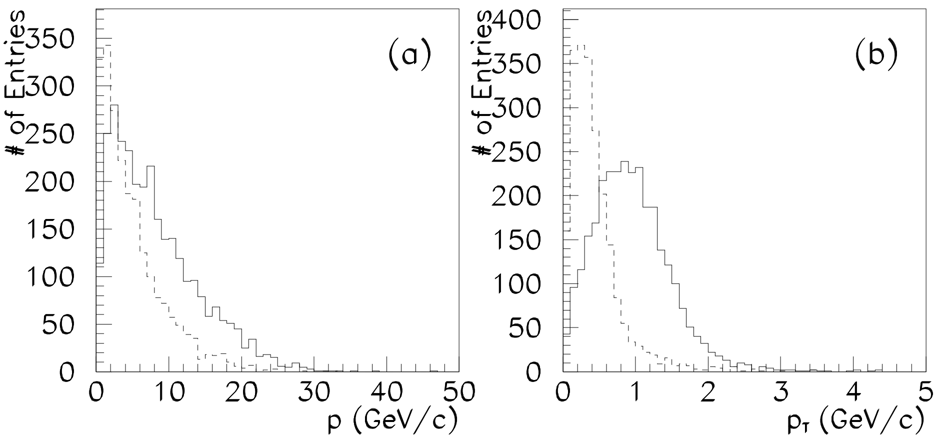

Figure 4.1: The predicted momentum distribution (a) and the predicted transverse momentum distribution (b) of leptons in $Z^0 \to q\bar{q}$ events. A solid line and a dashed line indicate semileptonic decays of b and c quarks, respectively.

The disadvantage of this technique is that the tagging efficiency of the lepton is very small. The branching ratio of the semileptonic decays of b quark is small; $B(b \to \ell) = (10.5 \pm 0.6 \pm 0.5)\%$ [39]. Furthermore, the efficiency that leptons generated by semileptonic decays are tagged is approximately 10% if the kinematical cuts described above are imposed to both leptons coming from b and $\bar{b}$ decays.

As described above, the cascade decay process, $b \to c \to \ell^+$, is a background process for B^0-$\bar{B}^0$ mixing analysis. In order to reduce this process in a sample of selected leptons, the parameter, p_{comb}, is adopted. This parameter is defined as $p_{comb} = \sqrt{p_T^2 + (p/10)^2}$. In figure 4.2, the scatter plots of p versus p_T for $b \to \ell$, $b \to c \to \ell$ and $c \to \ell$ decays are shown. If $p_{comb} > 1.1$ is imposed, most of cascade decay leptons can be rejected.

In this analysis, it is important to develop a technique to reject cascade decay leptons more powerfully compared with the parameter p_{comb}. Because the uncertainty of the contamination of the cascade leptons in the tagged lepton sample is a main source of systematic error for this analysis. In order to reduce $b \to c \to \ell$ decays, a novel technique has been developed for this analysis. This technique is based on the artificial neural network.

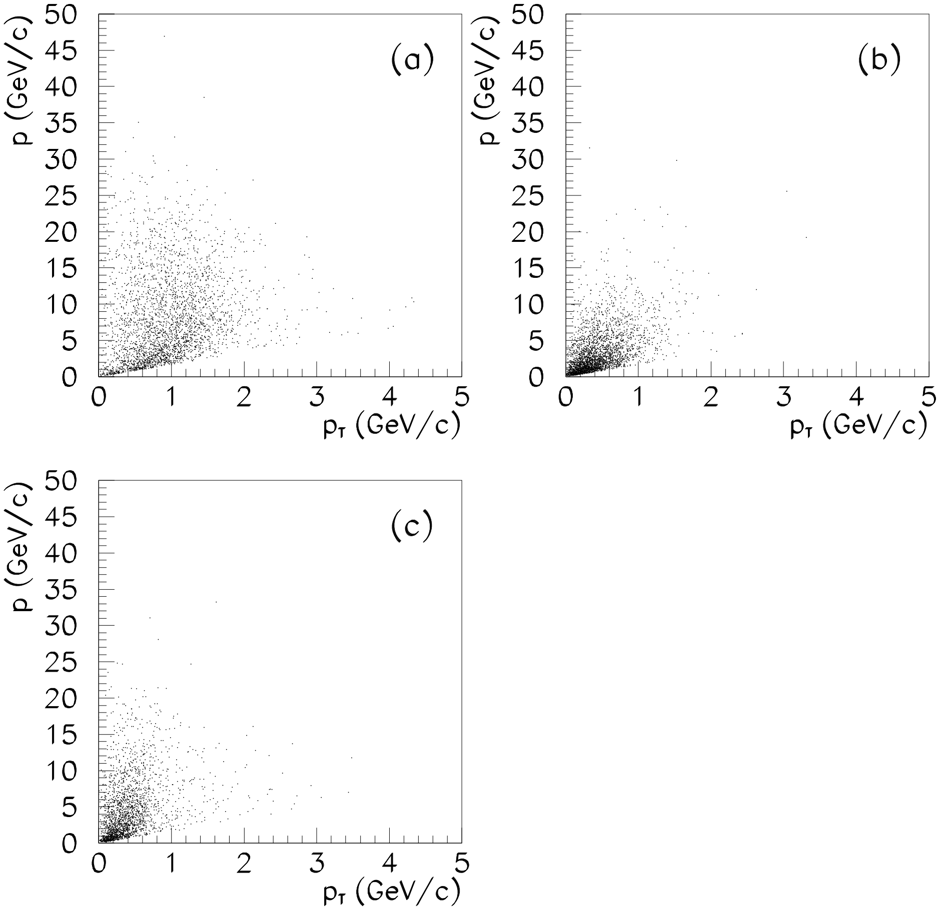

Figure 4.2: The scatter plot of the predicted momentum versus and the predicted transverse momentum for (a) b → ℓ, (b) b → c → ℓ and (c) c → ℓ decays.

This network has six neurons with one hidden layer. As input parameters, p, p_T and ω are chosen, where p is a momentum and p_T is a transverse momentum with respect to the jet axis for each lepton candidate. The third parameter, ω, is a subjet energy around the lepton track. The definition of ω is described below in more detail.

At first, the jet including the lepton track was divided into two subjets; one is the lepton track itself and called "lepton subjet" and the other is the remainder of the jet and called "non-lepton subjet". Next, the particle in the non-lepton subjet was examined whether it was closer to the lepton subjet axis or to the non-lepton subjet axis. If it was closer to the lepton subjet axis, it was removed from the non-lepton subjet and grouped into the lepton subjet. And the jet axes were re-defined for both subjets. This process was repeated until no further particle was transfered from one subjet to the other subjet or the invariant mass of the lepton subjet exceeded 2.5 GeV/c^2. Finally, the parameter ω was defined as the lepton subjet energy minus the lepton energy. The distributions of ω for $\mathrm{b} \to \ell$, $\mathrm{b} \to \mathrm{c} \to \ell$ and $\mathrm{c} \to \ell$ decays are shown in figure 4.3. This parameter can distinguish $\mathrm{b} \to \ell$ decay from other decays and is independent of p and p_T.

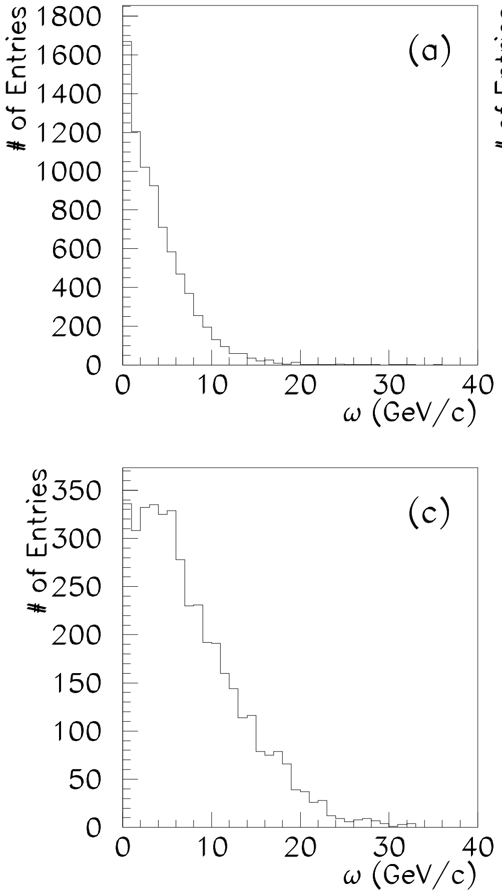

Figure 4.3: The distributions of ω for (a) $\mathrm{b} \to \ell$, (b) $\mathrm{b} \to \mathrm{c} \to \ell$ and (c) $\mathrm{c} \to \ell$ decays.

In figure 4.4, the purity as a function of the selection efficiency for $\mathrm{b} \to \ell$ decays for p_T cut alone, p_{comb} cut alone and this neural network are shown. The purity is defined as the ratio of $\mathrm{b} \to \ell$ decays to the sum of $\mathrm{b} \to \ell$ decays and $\mathrm{b} \to \mathrm{c} \to \ell$ decays. The neural network gives higher purity than other techniques.

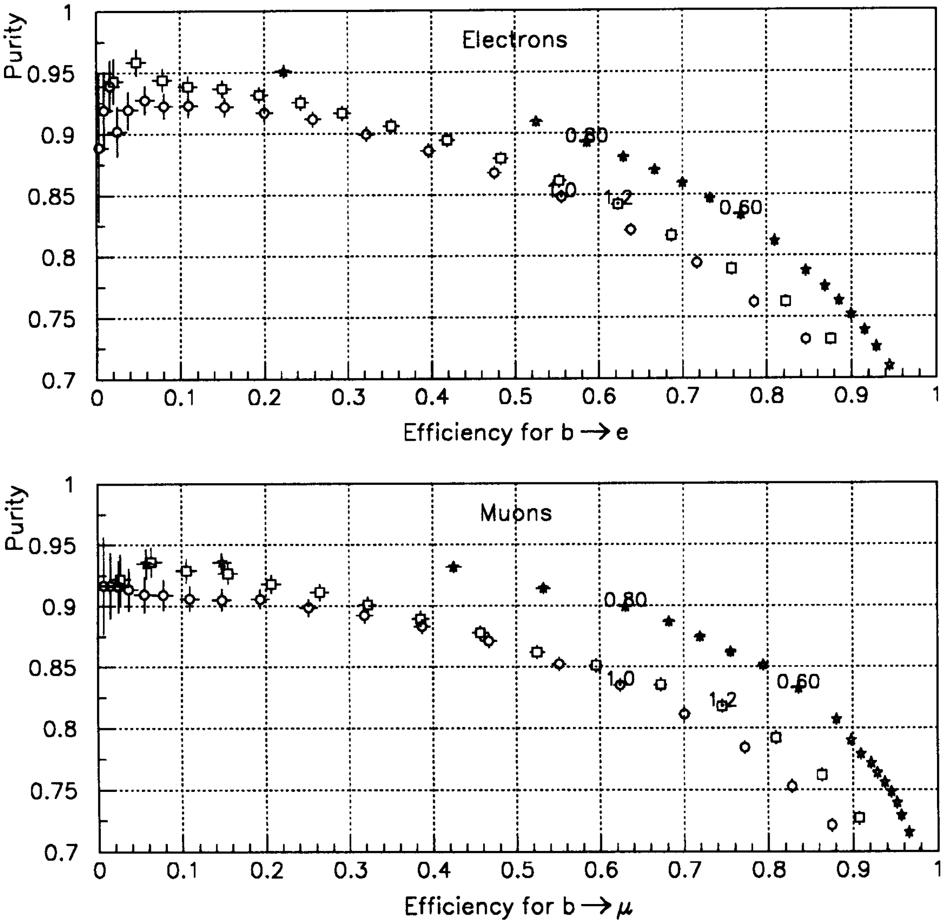

Figure 4.4: The purity as a function of the efficiency for b $\rightarrow \ell$ decays for p_T cut (circles), p_{comb} cut (squares) and this neural network output cut (stars) are shown. The top figure is for electrons, and the bottom figure is for muons.

By requiring that an event has at least two leptons, so-called dilepton event, only about 1% of the $Z^0 \rightarrow b\bar{b}$ decays can be chosen. But the purity of the $Z^0 \rightarrow b\bar{b}$ decay events in dilepton events are very high (~96%) because the fraction of the $c\bar{c} \rightarrow$ dilepton decays is very small. Thus the cascade decay from b quark decays can be substantially suppressed by this technique, and $Z^0 \rightarrow b\bar{b}$ events can be tagged and the sign of the parent b quark can be safely estimated although the remaining contribution from the cascade decay should be nevertheless taken into account.

4.3 Lepton Identification

4.3.1 Electron Identification

The electron identification is usually performed using two parameters, i.e. an ionization loss dE/dx and the energy of the electromagnetic cluster (E) divided by the momentum of the track (p) associated with the cluster, E/p. For electron tracks, dE/dx is about 10 keV/cm for $p > 2.0$ GeV/c and E/p is about unity. Identifying electrons using these parameters is very straightforward. But the disadvantage of this method is low efficiency (about 60%), and it is not useful for the overlap region of the barrel and endcap region since the energy resolution of the calorimeter is rather bad there. Due to a shortage of statistics of dilepton events of $Z^0 \rightarrow b\bar{b}$ decays, a new identification method with a high selection efficiency is needed.

In this analysis electrons were identified using 'artificial neural network' [80] which was trained by the Monte Carlo samples. This neural network with one hidden layer is made of fifteen neurons. Twelve of them are on an input layer, two on a hidden layer, and one an output layer as shown in figure 4.5. Input parameters are briefly described as follows;

- momentum of particle (GeV/c).
- $\cos\theta$ of track.
- dE/dx measured by the jet chamber.
- an error of dE/dx.
- E/p.
- a number of blocks in the electromagnetic cluster.
- E_{cone}/p.
- a number of blocks in the electromagnetic cluster where E_{cone} is defined.
- E_{cone}/E_{cone2}.
- absolute value of a distance between the electromagnetic cluster and the track in ϕ direction.
- absolute value of a distance between the electromagnetic cluster and the track in θ direction.
- a multiplicity of presampler hits in front of electromagnetic calorimeters.

where E is the associated electromagnetic energy to the charged track, and E_{cone} is a total energy within the cone with a half angle of 30 mrad. E_{cone2} is the energy defined as $E_{cone2} = E - E_{cone}$.

Using the Monte Carlo samples (~1M $Z^0 \rightarrow b\bar{b}$ events) with detector simulation, the neural network was trained.

By the Monte Carlo studies, the efficiency of electron tagging and the probability of hadron misidentifications are obtained. The 'efficiency' is defined as the probability that real electrons are tagged in multihadronic events. The 'probability of hadron misidentifications' is the probability that hadrons like pions are misidentified as electrons. These two values are correlated.

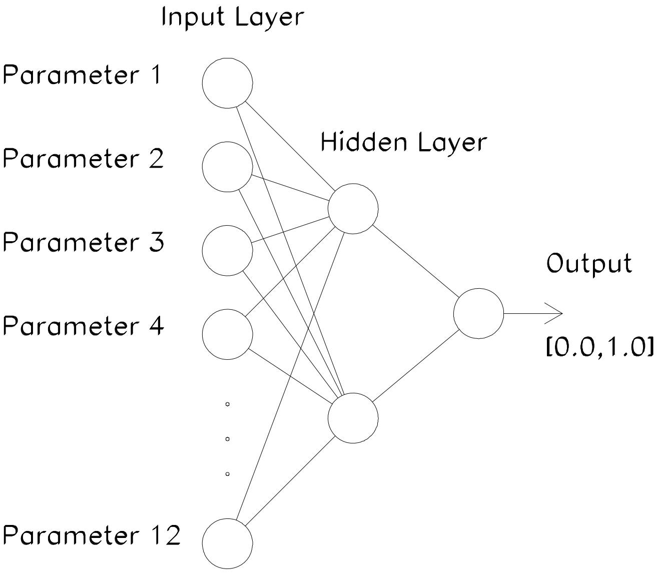

Figure 4.5: The scheme of the network for the electron identification.

The graph of the efficiency versus the probability of hadron misidentifications is shown in figure 4.6. If we use the 'standard electron identification' based on dE/dx and E/p described before, the efficiency and the probability of hadron misidentifications are about 55% and 0.17% respectively. The star mark in figure 4.6 shows the case for the standard electron identification. As can be seen, the neural network electron identification has the better efficiency than the standard electron identification. The plot on the e/hadron separation power is shown in figure 4.7. For the output value greater than 0.95, the e/hadron separation power of the neural network identification is very excellent. In fact, most of the tracks in the multihadronic events are pions, so the output value from the neural network was required to be more than 0.95 in this analysis.

In the identified electrons, the electrons generated by the photon conversion are also contained, which are removed in the following way [81].

To remove electrons generated by a photon conversion, the vertex of $\gamma \rightarrow e^+e^-$ in the r-ϕ plane was looked for. The partner track with an opposite charge was required to have $(dE/dx)_n > -2.5$. $(dE/dx)_n$ is defined as $((dE/dx)_{measured} - (dE/dx)_{theory})/\sigma_{measured}$ where $(dE/dx)_{measured}$ is a measured dE/dx, $\sigma_{measured}$ is an error of a measured dE/dx and $(dE/dx)_{theory}$ is a constant value (about 10 keV/cm). The angle between two tracks is very small for the photon conversion. So, it was required that the tracks are parallel at the closest point. And the distance between the interaction point and the conversion point was required to be greater than 2.0 cm to discard the Dalitz decays.

The differences between two tracks in the x-y plane and in the θ direction were defined as $\delta(x-y)$ and $\delta(\theta)$ respectively. To avoid some miscombinations, $\delta(x-y) < 5$ cm was required. The dimensionless parameter, Δ, was defined as

$$\Delta = \sqrt{(\frac{\delta(x-y)}{\delta^{90}(x-y)})^2 + (\frac{\delta(\theta)}{\delta^{90}(\theta)})^2},$$

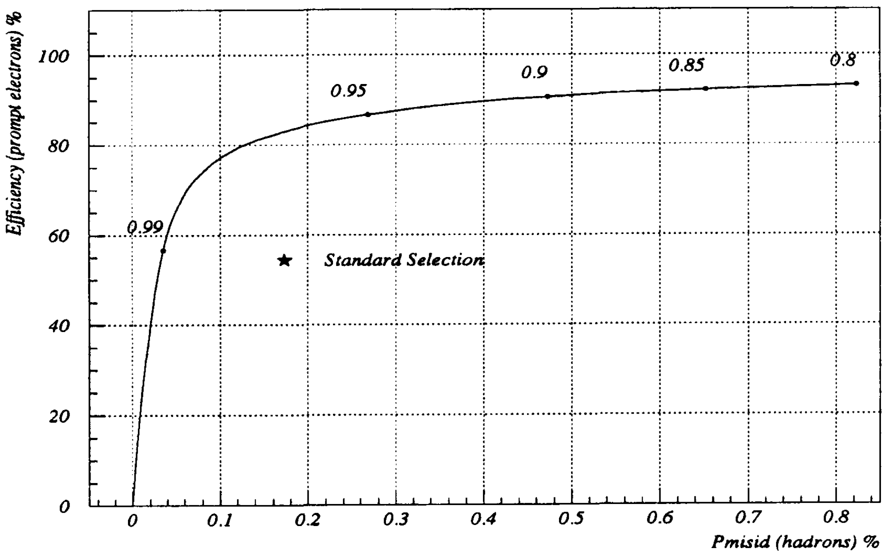

Figure 4.6: The relation of the efficiency and the hadron misidentification as a function of the threshold for output value from this neural network. The values on the figure show the threshold for the output from this network. The star mark shows the efficiency and purity in case of the usage of the standard electron identification.

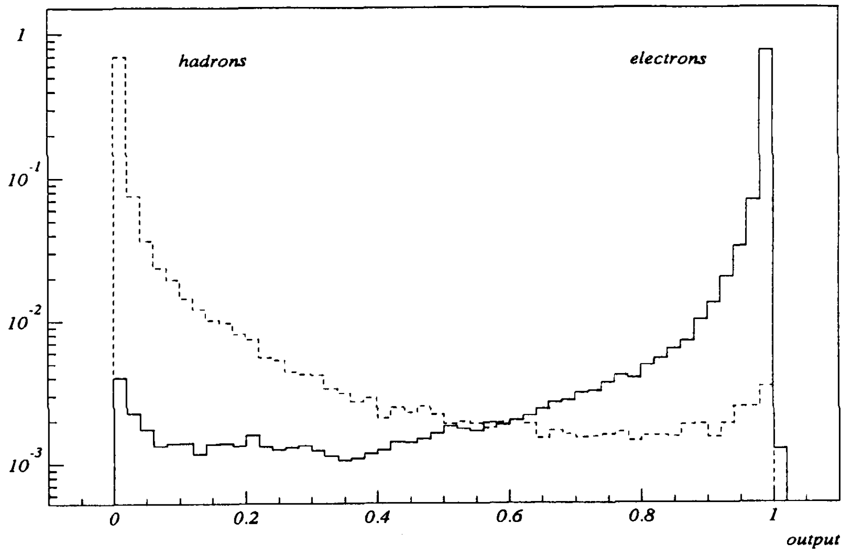

Figure 4.7: The e/hadron separation power as a function of the threshold for the neural network electron identification. The solid histogram is for electrons and the dashed histogram is for hadrons. The numbers of electrons and pions are same.

where $\delta^{90}(x-y)$ and $\delta^{90}(\theta)$ are the values where 90% of the conversions are contained in x-y plane and in the θ direction, respectively. In case the conversion radius is greater than 27 cm, only x-y information was used for this dimensionless parameter because of the poor measurement of the z direction (i.e., θ direction). The track pairs with $\Delta < 2.0$ were rejected as e^+e^- coming from a photon conversion.

4.3.2 Muon Identification

Muon identification is based on the penetration of a track through the hadron calorimeter which has a large material as an absorber for all region of the solid angle [82]. This strategy is very straightforward because most of pions and kaons are absorbed in the hadron calorimeter in front of the muon chamber.

A charged track which was measured in the central jet chamber was extrapolated toward the outside of the detector. The muon segment associated with this extrapolated track was looked for and the matching parameter between the track and the muon segment was investigated. This matching parameter was defined as

$$\chi = \sqrt{(\frac{\Delta(\phi)}{\sigma_{\Delta(\phi)}})^2 + (\frac{\Delta(\theta)}{\sigma_{\Delta(\theta)}})^2},$$

where $\Delta(\phi)$ and $\Delta(\theta)$ are the difference between the extrapolated track and the muon segment in the ϕ and θ direction respectively, and $\sigma_{\Delta(\phi)}$ and $\sigma_{\Delta(\theta)}$ are the error on each measurement. The distribution of this variable is shown in figure 4.8 for Monte Carlo muon sample. This variable was required to be less than 3.0 for muon candidates.

If there were more than one extrapolated muon tracks associated with one muon segment, the charged track with the smallest distance to the muon segment was considered as the candidate of the muon track for this segment. On the other hand, if there were more than one muon segments associated with one extrapolated charged track, the segment with the smallest χ was considered as the candidate of the segment for this track.

Furthermore, the ratio of the smallest χ to the second smallest χ was calculated and this candidate was considered as the muon track if this ratio was smaller than 0.5. This condition reduces the probability of associating the wrong central-detector track with a muon segment.

In the endcap region, unfortunately, there was a space which was not covered by the muon chamber as described in 3.2.7. To remove the efficiency bias depending on $\cos\theta$, the muon candidates were identified using the limited streamer tubes in the hadron calorimeter. There are seven layers of the limited streamer tubes described in 3.2.6. If there were hits along the extrapolated charged track in the most and/or second outer layer(s), this track was considered as the muon track.

Some kaon tracks are contaminated in selected muon tracks. In order to remove these kaon tracks, it was required that an ionization loss measured in the jet chamber was consistent with the theoretical value for muon.

The region of $|\cos\theta| < 0.6$ and the regions (1.28–1.35), (1.79–1.86), (4.42–4.49) or (4.93–5.50) in the ϕ direction were not used for the muon identification because there are small amounts of the material of the hadron calorimeter in this region and some pions and kaons can pass through the hadron calorimeter.

Sometimes there are many muon segments near the extrapolated charged track. This is mainly due to the leakage of the hadronic shower from the back of the hadron calorimeter, i.e., punchthrough. This track should not be recognized as the muon track. In order to reject this

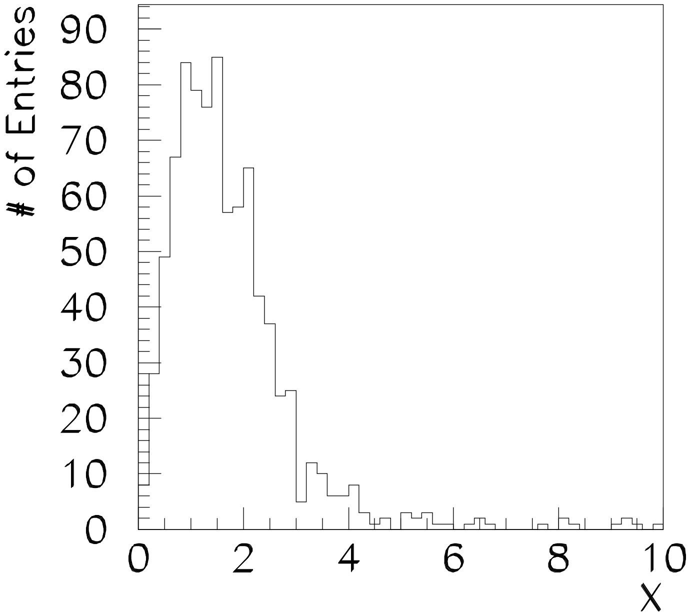

Figure 4.8: The distribution of the matching parameter, χ, for real muons (Monte Carlo sample).

track, the number of muon segments associated with one extrapolated track was required to be less than or equal to 20.

Using these muon identification criteria, the selection efficiency of 80% was achieved. The main background is due to the hadron tracks faking the muon track. This was estimated by the Monte Carlo study and the background contamination was estimated to be about 10%.

4.4 Jet Finding

The phenomenon that many particles are emitted to the same direction in the multihadronic events has been observed. This phenomenon is known as a 'jet'. Quarks generated by $Z^0 \rightarrow q\bar{q}$ decays fragment along the emitted direction and many hadrons are produced. Thus, $q\bar{q}$ events are observed as the events with two jets. These events are called '2-jet event' and each jet is called the 'quark jet'. When the hard gluon is emitted, the flux of particles is separated from the quark jet. These events are observed as the events with multi-jets. These events are called 'multi-jet event' and the jet whose source is the gluon is called 'gluon jet'. In general, the events of $Z^0 \rightarrow q\bar{q}$ always contain some jets. A number of jets for each multihadronic event have to be decided to assign particles to the jet.

Several algorithms to find jets in the event have been invented; 'JADE jet finder', 'Durham jet finder' and 'cone jet finder', which was used in this analysis. JADE jet finder is based on the invariant mass for all pairs of two particles in the event. The parameter, y_{ij}, was calculated for all pairs. y_{ij} is defined as $y_{ij} = 2E_iE_j(1-\cos\theta_{ij})/E_{vis}^2$, where $E_i(E_j)$ is an energy of a particle $i(j)$, θ_{ij} is the angle between two particles and E_{vis} is a visible energy of the event. The pair of particles with the smallest y_{ij} which is smaller than y_{cut}, which is a jet resolution parameter, are combined into a single particle and this procedure is iterated. On the other hand, Durham jet finder, which is similar to JADE jet finder, is based on the relative transverse momentum for each pair of particles; the parameter y_{ij} is modified as $2\min(E_i^2, E_j^2)(1-\cos\theta_{ij})/E_{vis}^2$.

These jet finders are very useful. But they have an weak point that low energy particles are sometimes assigned to the jet in the opposite hemisphere. Particles in the jet should be collimated. The more the energy of jet increases, the more these particles should be collimated. In the other words, these particles are contained within a narrow cone.

So, the cone jet finder [83] was used in this analysis. This jet finder has two parameters; R and ϵ. R is the half angle of the cone and ϵ is the minimum energy of the jet. This jet finder is based on looking for the groups of particles within the cone with a half angle R and with an energy greater than the minimum energy ϵ. For the present analysis, $R = 0.65$ radian and $\epsilon = 5.0$ GeV/c were adopted.

The strategy for this jet finder is described below.

For all particles, a cone with a half angle R was drawn in turn. The cone axis was defined as the direction of a momentum of each particle. A jet axis was calculated by summing up all momenta of particles in this cone. If the cone axis is equal to the calculated jet axis, this jet was defined as a 'proto-jet'. If not so, the calculated jet axis was redefined as the cone axis and this procedure was iterated until that the cone axis and the calculated jet axis become equal. The proto-jets whose energy is less than the cut off parameter, ϵ, were eliminated.

At this stage, some particles associate with several proto-jets. In order to remove this ambiguity, the following procedure was applied.

The energy of the overlapping tracks for the proto-jet i and j, where an energy of proto-jet i is greater than that of proto-jet j, was calculated and the fraction of this energy to the energy of proto-jet j was estimated. If this fraction is greater than 0.75, these tracks in the overlapping region were attached the proto-jet i. If not so, these were attached to the proto-jet j. But, in case the energy for the overlapping region is less than the cut off energy, ϵ, these tracks were attached to the nearest proto-jet.

4.5 Primary Vertex Finding

In order to measure the decay length, the positions of a primary vertex and a secondary vertex have to be known. These vertices are expected to be the production and the decay point of B hadrons, respectively. An interaction point of e^+e^- is not a 'point' and has a spread. This spread is about ± 300 μm in x direction and ± 20 μm in y direction. It is very important to determine a primary vertex precisely because a decay length of B hadrons is very short. So in this analysis a primary vertex was determined event by event.

A primary vertex was obtained by using all the good tracks and information on an average beam position. Information on an average beam position was introduced as two virtual tracks parallel to x- and y-coordinate which cross at the average beam position.

At first, a primary vertex was fitted as a common vertex for all the tracks in r-ϕ plane and χ^2 for each track were calculated. If there were tracks whose contribution to χ^2 was more than 4.0, the track with the largest χ^2 except for two tracks to constraint an average beam position was removed and a new primary vertex was refitted using residual tracks. When contribution to χ^2 from each residual good track was less than 4.0, this fitting procedure was completed. If a number of tracks used to determine a primary vertex was less than three including two tracks to constrain an average beam position, a primary vertex finding was failed and the average beam position was taken as the primary vertex.

4.6 Secondary Vertex Finding

To measure the decay length of b-flavored hadrons, the secondary vertex including the lepton track was reconstructed in the r-ϕ plane. The reason why these vertices were not reconstructed in three dimension is that the spatial resolution along the z direction is not so good. So far, information on the z coordinate provided by the silicon microvertex detector was not used although this information was available.

At first, lepton tracks were selected in a multihadronic event by requiring the lepton identification criteria. For the selected lepton track, the requirement was imposed that their impact parameter d_0 was less than 1.0 cm. This requirement rejects the background tracks like muons from the pion decay in flight and the hadrons misidentified as a lepton due to $\mathrm{K}_s^0 \rightarrow \pi^+\pi^-$ and $\Lambda \rightarrow \pi^-\mathrm{p}$ decays. And the lepton track was required that the error of d_0 was less than 0.1 cm to guarantee a significance of the track. Here, these requirements are classified as CUT1. The CUT1 criteria are listed in table 4.5.

Impact parameter, d_0	$<$1.0 cm
Error of the impact parameter, σ_{d_0}	$<$0.1 cm

Table 4.5: The summary on the cuts for the lepton tracks (CUT1).

Next, 'seed tracks' were selected in this events. It was required that the seed tracks were measured in the silicon microvertex detector and/or the central vertex chamber very precisely. And they were used to reconstruct a 'seed vertex', which was defined as the core of the secondary vertex. The lepton tracks satisfying the CUT1 were included in the selected seed tracks. In order to select seed tracks three cuts were imposed. The first cut is that a number of the axial wire hits measured in the central vertex chamber is more than 6. The second cut is that at least one hit measured in the silicon microvertex detector and/or at least one first hit measured in the central vertex detector are associated with the track. These cuts were required to reduce the error on the decay length measurement. The third cut is that the seed tracks should be significantly away from the primary vertex; $|d_0/\sigma_{d_0}|_{primary}$ is greater than 3.0 to reduce the tracks from the fragmentation process. Here, these requirements are classified as CUT2. The CUT2 criteria are listed in table 4.6.

Number of CV axial hits	$>$6
Number of SI hits and/or CV first hits	$\geq$1
Significance, $|d_0/\sigma_{d_0}|_{primary}$	> 3.0

Table 4.6: The summary on the cuts for the seed tracks (CUT2), where SI and CV denote the silicon microvertex detector and the central vertex chamber respectively.

If tracks satisfying the CUT1 were not found in one jet, the secondary vertex finding was not performed in this jet. If a number of tracks satisfying the CUT2 was less than three, tracks with the most, second and third largest significance $|d_0/\sigma_{d_0}|_{primary}$ in this jet were assigned as seed tracks even though they did not satisfy the significant cut. Of course, these three tracks must have at least one hit measured in the silicon microvertex detector and/or first hits measured in the central vertex chamber. After this step, if a number of seed tracks was less than two in this jet, the secondary vertex finding was given up in this jet.

If a number of seed tracks was only two in the jet, the seed vertex was reconstructed using only these two seed tracks to keep the efficiency on the secondary vertex finding high.

If a number of seed tracks was more than two in the jet, one seed track which was not the lepton track was selected and the seed vertex was reconstructed from this seed track and the lepton track. And another seed track was picked up and this seed vertex was refitted. At this stage, if a significance $|d_0/\sigma_{d_0}|_{primary}$ for a selected seed track was less than three, this seed track was rejected as long as $|d_0/\sigma_{d_0}|_{primary} < |d_0/\sigma_{d_0}|_{secondary}$. This requirement was needed to reduce the misreconstruction of the secondary vertex. The track with the large probability (> 0.01) of coming from the seed vertex was added to the seed vertex and the vertex was redefined including the added track. This procedure was iterated till no track was found. After that, the vertex using all tracks which were assigned to the vertex was refitted.

Using information on the position of the primary and secondary vertex, the decay length was measured. Here, the 'sign' was defined for the observed decay length. If the reconstructed secondary vertex was in a forward direction along with the jet, a sign of the decay length was 'positive'. Otherwise it was 'negative'. This definition is illustrated in figure 4.9. The positive decay length has information on the lifetime of long-lived particles convoluted with the resolution. In contrast, the negative decay length has information on only position resolution around the origin.

To clean up the bad secondary vertices, the several cuts were required to the reconstructed secondary vertex. The secondary vertices formed by only two tracks might include many backgrounds compared with the secondary vertices formed by more than two tracks. Then the cuts were imposed to the secondary vertices with only two tracks and those with more than two tracks separately.

For vertices with only two tracks, following requirements were imposed. The observed transverse decay length with respect to the jet axis, L^{2D}_{tran}, was required to be less than 3σ to reduce the secondary vertices reconstructed accidentally, where σ is the measured error of the secondary vertex. Two dimensional error in r-ϕ plane of the secondary vertex, $\sigma_{L^{2D}}$, was required to be less than 0.06 cm to keep the spatial resolution on this vertex finder good. The absolute value of the impact parameter of the lepton track divided by the two dimensional decay length, $|d_0^{lepton}/L^{2D}|$, was required to be lager than 0.04 to improve the reliability at the large decay length. The reconstructed secondary vertices with only two tracks suffer from the accidental background very severely. That the impact parameter of the lepton track is small means that the true decay length is not so long. So, the secondary vertices with the long decay length and the lepton track with small impact parameter were rejected. The invariant mass, M_{VTX}, was calculated using all the tracks associated with the secondary vertex. The mass cut, $M_{VTX} > 0.75$ GeV/c^2, was required because this vertex is due to the decay of a B hadron. Finally, for the vertices with the negative decay length, it was required that the negative decay length divided by the error on the secondary vertex, $L^{2D}/\sigma_{L^{2D}}$, was greater than -2. Although the vertices with the negative decay length are needed in order to study the resolution, many vertices reconstructed accidentally are included in the negative decay length region. By this cut the vertices reconstructed accidentally in the negative decay length region were rejected. In table 4.7, the cuts for the secondary vertex with only two tracks are summarized.

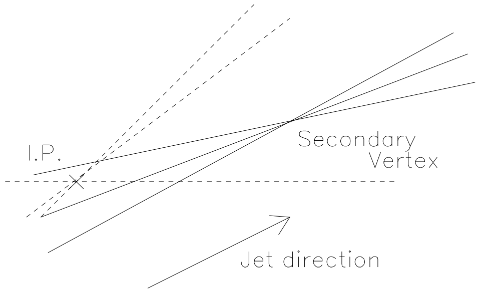

(a) Positive decay length

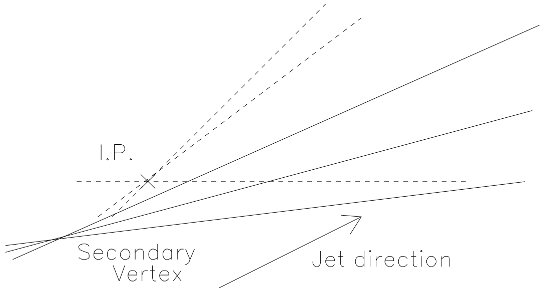

(b) Negative decay length

Figure 4.9: Definition of a 'positive' decay length (a) and a 'negative' decay length (b).

Transverse decay length, L^{2D}_{tran}	$<3\sigma$
Secondary vertex error, $\sigma_{L^{2D}}$	$<$0.06 cm
$\lvert d_0^{lepton}/L^{2D}\rvert$	$>$0.04
Mass of the secondary vertex, M_{VTX}	$>$0.75 GeV/c^2
Negative decay length, $L^{2D}/\sigma_{L^{2D}}$	> -2

Table 4.7: The summary on the cuts for reconstructed secondary vertices associated with only two tracks.

For vertices with more than two tracks, very similar cuts were imposed to them. The transverse decay length cut was the same as before. The cut on the secondary vertex error was loosen to less than 0.08 cm. In contrast, the invariant mass cut was tightened to be more than 1.0 GeV/c^2. The negative decay length cut was also loosen to $L^{2D}/\sigma_{L^{2D}} > -3$ because the probability is very small that the secondary vertices with at least three tracks are reconstructed accidentally. For the vertices including only two good tracks with significance $|d_0/\sigma_{d_0}|_{primary} > 3.0$, the $|d_0^{lepton}/L^{2D}|$ cut was required to be greater than 0.02. In table 4.8, the cuts for the reconstructed secondary vertex with more than two tracks are summarized.

Transverse decay length, L^{2D}_{tran}	$<3\sigma$
Secondary vertex error, $\sigma_{L^{2D}}$	<0.08 cm
Mass of the secondary vertex, M_{VTX}	>1.0 GeV/c^2
Negative decay length, $L^{2D}/\sigma_{L^{2D}}$	> -3
($\lvert d_0^{lepton}/L^{2D}\rvert$	>0.02)

Table 4.8: The summary on the cuts for reconstructed secondary vertices associated with more than two tracks.

To convert the observed two dimensional decay length, L^{2D}, to the three dimensional decay length, L^{3D}, information on the jet direction was used. The flight direction of B hadrons was assumed to be along the jet axis. When θ_{jet} is defined as the angle between the jet axis and the beam axis, the three dimensional decay length was obtained by $L^{3D} = L^{2D}/\sin\theta_{jet}$. After these procedures, secondary vertices including a lepton track were reconstructed successfully.

In figure 4.10, the observed decay length distribution and the distribution of the difference between the observed decay length and the true decay length for only b $\to \ell^-$ decays in the Monte Carlo events are shown. The latter distribution was fitted to the Gaussian distribution to obtain the spatial resolution around the primary vertex. The spatial resolution is (465 ± 7) μm neglecting longer tails on both sides.

The efficiency for this vertex finder was studied using Monte Carlo samples. This efficiency has a dependence on the parent quarks and the decay mode. In table 4.9, the efficiencies for several types of decay are listed.

u, d, s $\to \ell$	53.0 ± 0.6 %
c $\to \ell$	60.5 ± 0.7 %
b $\to$c$\to \ell$	73.6 ± 0.7 %
b $\to \ell$	74.5 ± 0.2 %

Table 4.9: The summary of the vertex reconstruction efficiencies for several event types.

The distribution of the multiplicity of the tracks associated with the reconstructed secondary vertex is shown in figure 4.11. Even if the reconstructed secondary vertex is one for the neutral B meson, there is a sizable probability that the secondary vertex has odd associated tracks, not even tracks. This is due to the fact that all tracks generated by the B hadron decay are not always measured as good tracks. In case the tracks are very close to other track, for example, there is a probability that the track is recognized as a bad track.

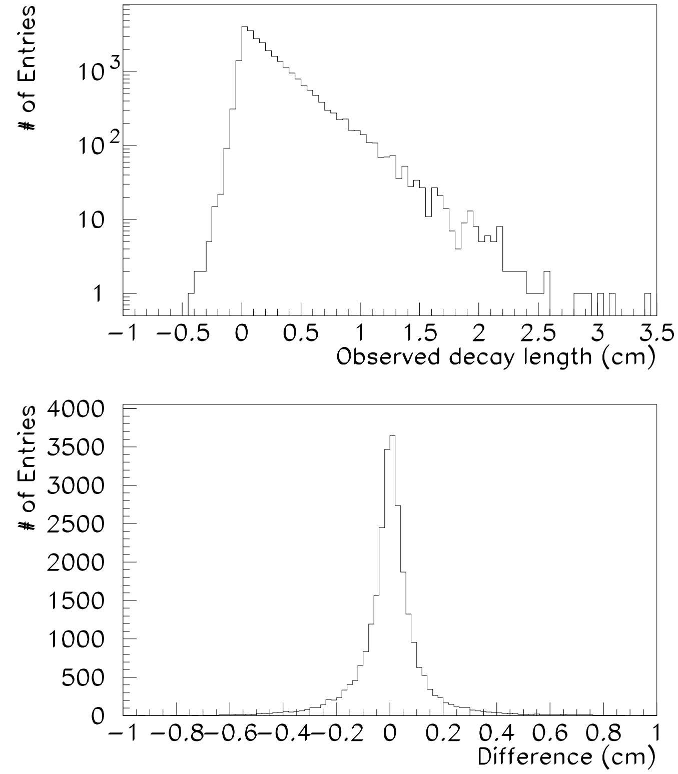

Figure 4.10: The observed decay length distribution (top) and the distribution of the difference between the observed decay length and the true decay length (bottom) for only $b \rightarrow \ell$ decays. Both are for the Monte Carlo events.

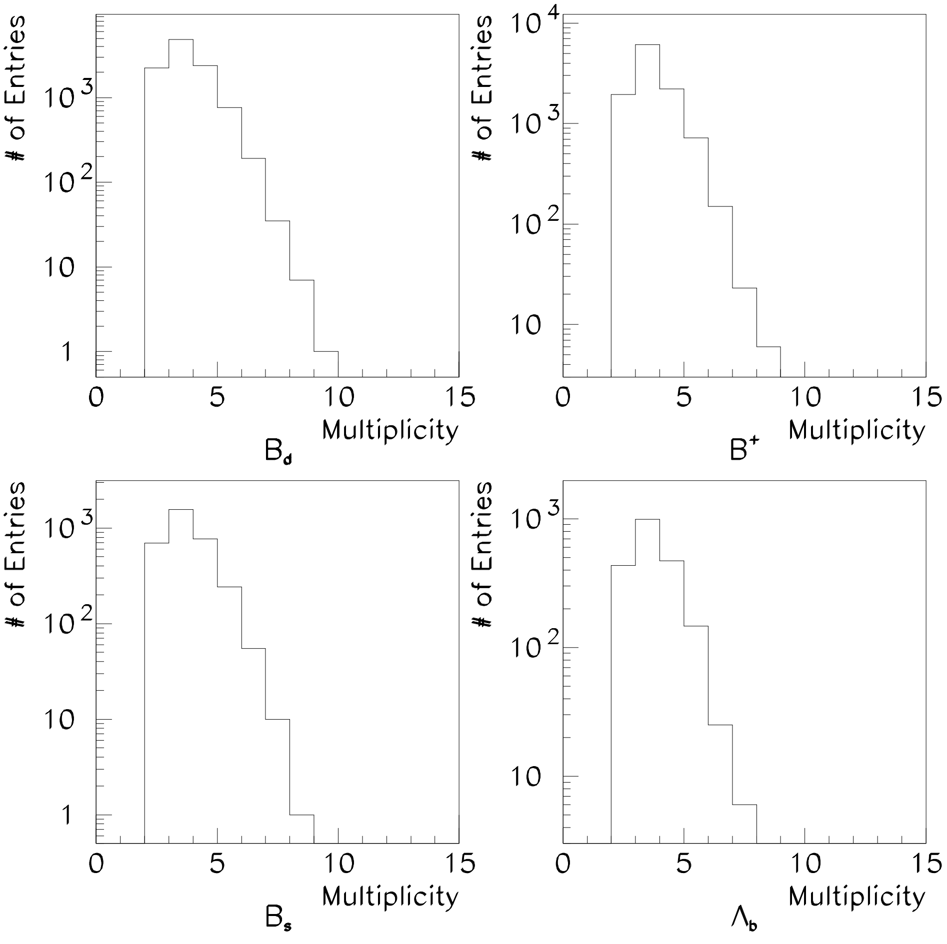

Figure 4.11: The distribution of the multiplicity of the tracks associated with the reconstructed secondary vertex for B_d, B^+, B_s and Λ_b.

4.7 Lorentz Boost Estimation

In order to convert the measured decay length to the proper decay time, the Lorentz boost factor, $\beta\gamma$, has to be estimated. The main problem is that the missing energy carried by the neutrino has to be estimated. But it is not easy to estimate this missing energy, because the initial energy of B hadrons generated by Z^0 decay can not be given. For this analysis the excellent method to estimate the Lorentz boost factor was developed. At first, the total energy of the jet including the missing energy carried by the neutrino was estimated. Next, the energy of the B hadron was estimated by subtracted the energy on the fragmentation process from the jet energy. By using this estimated B hadron energy, the Lorentz boost factor was estimated.

To estimate the jet energy including the missing energy carried by a neutrino, dilepton events were treated as a two-body decay of an object with the mass, M. First, the dilepton event was divided into the 'lepton jet' which contains the lepton track generated by the semileptonic b quark decay and others. Here, the energy, the momentum and the mass for each body are supposed to be E_i, p_i and m_i ($i = 1, 2$). In this section, the subscript i is defined as '1' for the lepton jet. By the energy conservation law, the following relation was given;

$$E_1 + E_2 = \sqrt{p_1^2 + m_1^2} + \sqrt{p_2^2 + m_2^2} = M.$$

The lepton jet and the rest of the event are emitted back-to-back because the energies of electrons and positrons are the same in LEP. That means $p_1 = -p_2 = p$, where p is the momentum of the lepton jet. By solving this equation, the energy of the lepton jet including a missing neutrino, E_1, can be obtained. That is

$$E_1 = \sqrt{p^2 + m_1^2} = \frac{M^2 + m_1^2 - m_2^2}{2M}.$$

For the mass of the lepton jet, m_1, B hadron mass was used but this value is not sensitive to the result. The mass of the rest of the event, m_2, was calculated by summing up all the good tracks and all the electromagnetic clusters not associated with the tracks in the jet 2. The charged tracks were supposed to be pions. The visible energy of this event, E_{vis} were calculated and m_2 was rescaled by the factor of $80.0/E_{vis}$. And the twice of the beam energy was used as the center-of-mass energy, M, which is approximately Z^0 mass. This method is very powerful to estimate the jet energy including the missing energy due to the neutrino emission for not only two jet events but also three or more than three jet events.

Next, charged tracks and electromagnetic clusters in the lepton jet were assigned to the B hadron decay products and the fragmentation products. B hadron decays into a lepton, neutrino and a charm hadron. So that, tracks and electromagnetic clusters associated with a charm hadron had to be identified. The other tracks and electromagnetic clusters were classed as fragmentation products.

It is easy to identify charged tracks associated with a charm hadron. The direction of a charm hadron was first estimated by the momentum sum of the tracks coming from the secondary vertex, except for the lepton track. The direction was re-calculated by summing up momenta weighted by the probability of each associated track, where the probability was estimated by the opening angle between each track and the charm hadron direction roughly estimated as above. The dependence of this probability on the opening angle was determined by the Monte Carlo study. The overall probability that the track was coming from the charm decay was also estimated by taking into account other factors; for example, whether it originated from the primary vertex or the secondary vertex. Finally, if the overall probability exceeded 75%, the track was assumed to come from charm hadron decay. If this probability was less than 25%, this track was assigned to be the fragmentation product. The others were weight according to the probability.

In contrast, it is not easy to identify electromagnetic clusters associated with a charm hadrons. In case the opening angle between the neutral cluster and the charm hadron direction determined as above was less than 13°, the cluster was assumed to come from the charm hadron decay. If this opening angle was greater than 32°, the cluster was assigned to the fragmentation product. The other clusters were given weight depending on their opening angles.

By the tracks and electromagnetic clusters classified as fragmentation products, the total energy of the fragmentation, E_{frag}, was calculated taking their weight into account. The energy of B hadron, E_B, was calculated by $E_B = E_1 - E_{frag}$.

Then the Lorentz boost factor $\beta\gamma$ was calculated by

$$\beta\gamma = \frac{p_B}{m_B} = \frac{\sqrt{E_B^2 - m_B^2}}{m_B}.$$

So, the proper decay time, t, was estimated as

$$t = \frac{m_B L^{3D}}{c\sqrt{E_B^2 - m_B^2}},$$

where m_B was supposed to be 5.3 GeV/c^2.

In figure 4.12, the scatter plot of the observed (reconstructed) proper time, t, versus the true proper time, t', is shown for Monte Carlo events. The proper time measurement is very good. The points around $t = 0$ away from the expected correlation are due to the misreconstruction of the secondary vertex. In figure 4.13, the observed proper time distribution is shown for real and Monte Carlo data. A nice agreement between the real data and the Monte Carlo data can be seen. And the efficiency of finding the secondary vertex is shown in figure 4.14 as a function of the true proper time for only b $\rightarrow \ell^-$ decays. The bias depending on the true proper time can not be found except for $t \sim 0$ psec^{-1}.

4.8 Likelihood Fitting

4.8.1 Likelihood function

The reconstructed secondary vertices are due to direct bottom quark decays, cascade decays, charm quark decays and the misreconstructed decays of light quarks. The cascade decay is the main background for this analysis. Because the cascade decay generates a lepton with opposite sign of a parent b quark, it can fake B meson mixing. And for both b quark direct and cascade decays, neutral B hadrons ($\mathrm{B_d}$ and $\mathrm{B_s}$) are influenced by the mixing effect but other B hadrons ($\mathrm{B^+}$ and Λ_b) are not influenced. Although charm quarks have an observable long decay proper time, they have nothing to do with the effect on $\mathrm{B^0}$-$\mathrm{\bar{B}^0}$ mixing. Many accidentally reconstructed secondary vertices are around the primary vertex. It is important to understand them in order to study the $\mathrm{B_s}$ mixing, since $\mathrm{B_s}$ oscillation starts to occur already around the primary vertex. So, the observed proper time distributions for several kinds of secondary vertex have to be known.

In order to study the observed proper time distribution, Monte Carlo samples, which do not take into account the $\mathrm{B^0}$-$\mathrm{\bar{B}^0}$ mixing, were used. At first, events with at least one secondary

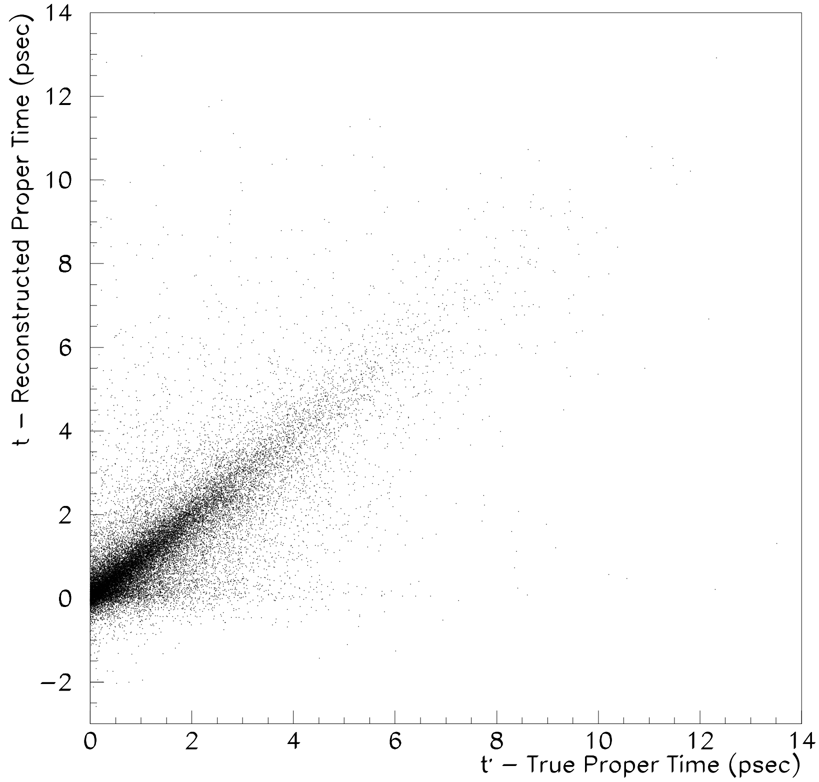

Figure 4.12: The scatter plot of the observed proper time versus the true proper time.

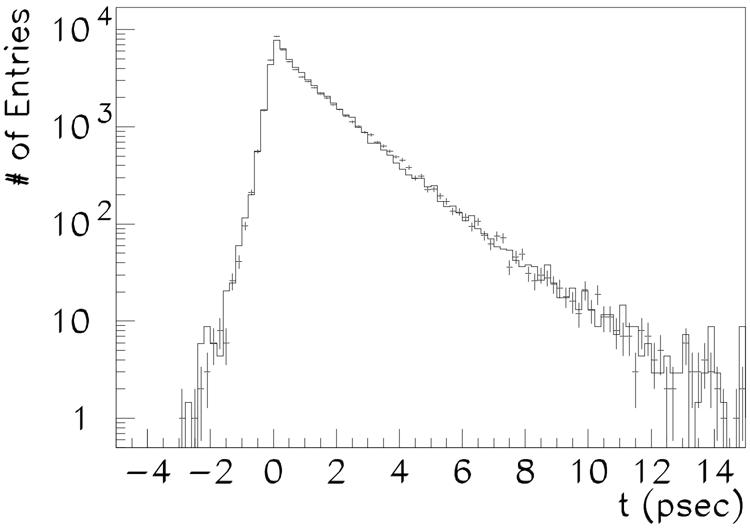

Figure 4.13: The observed proper time distribution, where the points with error bar are for real data and the histogram is for Monte Carlo data.

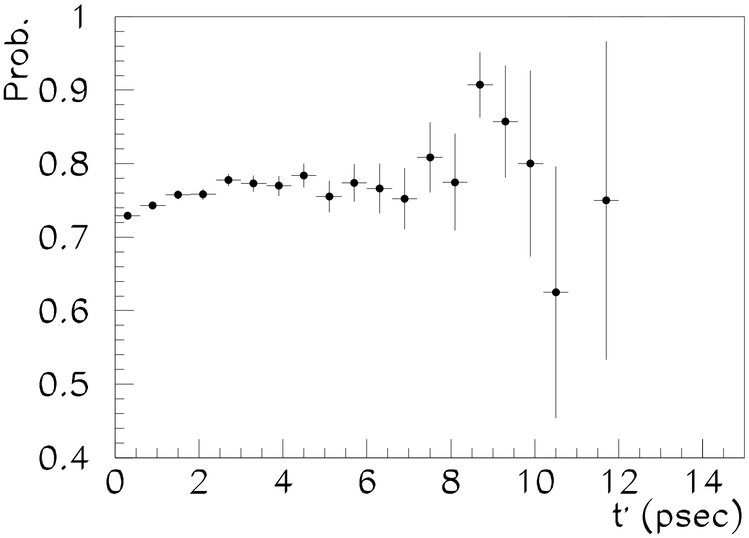

Figure 4.14: The efficiency of the secondary vertex finding as a function of the true proper time.

vertex were selected by imposing the same cuts as real data analysis. These vertices were categorized as follows;

Category (1) light quark pair events

Category (2) real leptons from charm quark decays

Category (3) fake leptons from charm quark decays

Category (4) real or fake negative leptons from $\mathrm{B_d}$ decays

Category (5) real or fake negative leptons from $\mathrm{B_s}$ decays

Category (6) real or fake negative leptons from B^+, $\bar{\Lambda}_b$ decays

Category (7) real or fake positive leptons from $\mathrm{B_d}$ decays

Category (8) real or fake positive leptons from $\mathrm{B_s}$ decays

Category (9) real or fake positive leptons from B^+, $\bar{\Lambda}_b$ decays

Category (10) real or fake leptons not coming from b decays in $\mathrm{b\bar{b}}$ events

where 'real leptons' mean an electron (a positron) or a muon and 'fake leptons' mean hadrons misidentified as an electron (a positron) or a muon.

Category (1) is due to accidental reconstruction in $\mathrm{Z^0 \to u\bar{u}, d\bar{d}, s\bar{s}}$ events. These vertices have no correlation between the sign of the tagged lepton and the sign of a parent quark. Category (2) and (3) are from $\mathrm{Z^0 \to c\bar{c}}$ decays. Although these vertices have no effect on the B mixing like category (1), they have a long lifetime which is observable. So Category (1) and Categories (2), (3) have to be treated separately. The sign of lepton from parent charm quark decay correlated with the sign of the parent charm quark. The $\mathrm{c} \to \ell^+$ decays were included in Category (2) and other decays in Category (3). The Categories (4) – (10) are from $\mathrm{Z^0 \to b\bar{b}}$ decays. These decays can be divided into 'direct' decays, 'cascade' decays and the accidental reconstructions for fragmentation particles and so on. The last of them was categorized into Category (10). Although the distributions for Category (1) and Category (10) must be very similar, they have to be treated separately due to the difference of a number of $\mathrm{Z^0 \to u\bar{u}, d\bar{d}, s\bar{s}}$ decays and $\mathrm{Z^0 \to b\bar{b}}$ decays in dilepton samples. For both direct and cascade decays, vertices were divided into the following types, $\mathrm{b \to \bar{B}_d}$, $\mathrm{b \to \bar{B}_s}$, which are influenced by the B mixing, and $\mathrm{b \to B^+}$ and Λ_b decays, which are not influenced by the B mixing. They were categorized into Categories (7), (8), (9) for direct decays and (4), (5), (6) for cascade decays.

In addition, for $\mathrm{Z^0 \to b\bar{b}}$ decays, if the sign of the tagged lepton charge is the same as the sign of the parent b quark charge, the lepton was categorized into (7)-(9). And if the sign of the tagged lepton charge is different from the sign of the parent b quark charge, the lepton was categorized into (4)-(6). For example, $\mathrm{b} \to J/\psi$ decays were categorized into (4)-(6) for $\mathrm{b} \to J/\psi \to \ell^+$ and (7)-(9) for $\mathrm{b} \to J/\psi \to \ell^-$. The $\mathrm{b} \to \cdots \to \gamma \to \mathrm{e}^+$ decays were categorized into (4)-(6) and $\mathrm{b} \to \cdots \to \mathrm{K^0_S} \to \pi^-$ decays were categorized into (7)-(9).

These distributions for b decays were fitted by following formula;

$$f_i(t) = \frac{1}{\tau_i}\int_0^\infty dt' e^{-\frac{t'}{\tau_i}}\left\{b_i u_i\left(\sigma(t'); t\right) + (1-b_i) v_i\left(\sigma'(t'); t'-t\right)\right\} \quad \text{for } i = 4,5,6,7,8,9.$$

where t is the measured proper time and t' is the true proper time, the correlation of which is provided from a Monte Carlo study. The lifetime τ_i was fixed to be 1.4 psec^{-1}. For real data, the correction factors described in table 4.4 are applied. The function u_i describes a misreconstruction of secondary vertices to the primary vertex and is written by

$$u_i\left(\sigma(t');t\right) = \sum_{j=1}^{3} y_{ij} G_A\left(t, \sigma_{ij}^{-}(t'), \sigma_{ij}^{+}(t')\right).$$

On the other hand, the function v_i described a b hadron decay with a lifetime τ and is written by

$$v_i\left(\sigma'(t');t'-t\right) = \sum_{j=1}^{3} y'_{ij} G_A\left(t'-t, \sigma_{ij}'^{-}(t'), \sigma_{ij}'^{+}(t')\right)$$

And $G_A(x, \sigma_+, \sigma_-)$ is an 'asymmetric Gaussian', which is described by

$$G_A(t, \sigma_-, \sigma_+) = \begin{cases} \frac{1}{\sqrt{2\pi}\bar{\sigma}} \exp(-\frac{t^2}{2\sigma_-^2}) & \text{for } t < 0 \\ \frac{1}{\sqrt{2\pi}\bar{\sigma}} \exp(-\frac{t^2}{2\sigma_+^2}) & \text{for } t > 0. \end{cases}$$

σ_+ and σ_- are an width for $t > 0$ and $t < 0$ respectively. $\bar{\sigma}$ is an average of σ_+ and σ_-; $\bar{\sigma} = (\sigma_+ + \sigma_-)/2$. This function is normalized to be one, i.e.,

$$\int_{-\infty}^{+\infty} dt G_A(t, \sigma_-, \sigma_+) = 1.$$

For above formulae y_{ij} and y'_{ij} are a fraction of an asymmetric Gaussian j for each category i, i.e., $\sum_j y_{ij} = \sum_j y'_{ij} = 1$.

Three asymmetric Gaussians describe the spatial resolutions for the secondary vertex reconstruction. The narrowest asymmetric Gaussian describes the intrinsic resolution corresponding to vertex resolution of b decays. On the other hand, the other wider asymmetric Gaussians are due to misreconstruction of vertex from the decay of pions and kaons in flight or hard multiple scattering. From figure 4.12, it can be seen that the measured proper time resolution is dependent on the true proper time. Then all the widths of the asymmetric Gaussians, $\sigma_{ij}^{\pm}$, have to be time dependent, i.e.,

$$\begin{aligned} \sigma_{ij}^{\pm}(t') &= \alpha_{ij}^{\pm} + \beta_{ij}^{\pm} t' \\ \sigma_{ij}'^{\pm}(t') &= \alpha_{ij}'^{\pm} + \beta_{ij}'^{\pm} t' \\ & \qquad \text{for } i = 4, 5, 6, 7, 8, 9 \end{aligned}$$

where $\alpha_{ij}^{\pm}$ and $\beta_{ij}^{\pm}$ are constants. The fact that $\sigma_{ij}^{\pm}$ is time dependent means the spatial resolution of the vertex finder becomes worse as the observed proper time becomes longer.

Many parameters which are included in above formulae were obtained by the following method.

At first, the vertices for b $\rightarrow$ ℓ decays from Monte Carlo analysis were divided into seven bins for the true proper time, $0.0 < t' < 0.5$ psec, $0.5 < t' < 1.0$ psec, $1.0 < t' < 2.0$ psec, $2.0 < t' < 3.0$ psec, $3.0 < t' < 4.0$ psec, $4.0 < t' < 5.0$ psec and $5.0 < t'$ psec. For each bin, the distributions of the discrepancy between the observed proper time and the true proper time, i.e., $t - t'$ distribution, were obtained. These discrepancy distributions are shown in figure 4.15. The time dependence of the resolution can be seen clearly. These distributions were fitted by

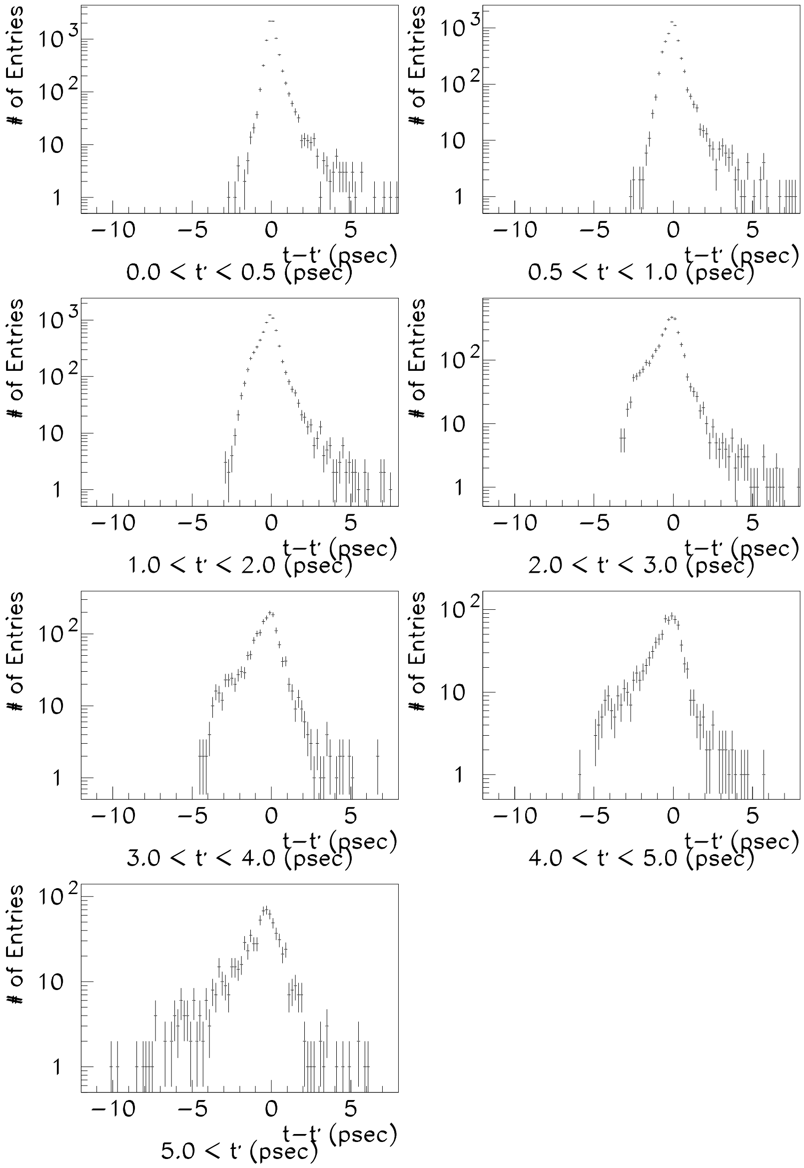

0.0 < t' < 0.5 (psec)

0.5 < t' < 1.0 (psec)

1.0 < t' < 2.0 (psec)

2.0 < t' < 3.0 (psec)

3.0 < t' < 4.0 (psec)

4.0 < t' < 5.0 (psec)

5.0 < t' (psec)

Figure 4.15: The distributions of the discrepancy between the observed proper time and the true proper time for each true proper time bin. (Monte Carlo)

a single asymmetric Gaussian in the region around the origin and the narrowest widths, $\sigma_{1j}^{\pm}$, were obtained. After these $\sigma_{1j}^{\pm}$ were fixed, the middle widths, $\sigma_{2j}^{\pm}$, were obtained by fitting the distribution in a little more wide range around the origin. At last, the widest widths, $\sigma_{3j}^{\pm}$, were obtained by fitting the distribution in the whole region of $t - t'$.

At the next step, the observed proper time distributions were calculated for each bin of true proper time by using the $\sigma_{1j}^{\pm}$ determined above. They are shown in figure 4.16. For the range where the observed and true proper time are almost the same, the calculated curve reproduces well the original Monte Carlo data. Of course, a discrepancy can be seen around $t = 0$ due to misreconstruction of the secondary vertex. In order to describe this discrepancy around $t = 0$, additional asymmetric Gaussians were introduced and the fraction of the misreconstruction was also fitted at the same time.

In figure 4.17, the observed proper time distributions with the calculated curves for each true proper time bin are shown as final fitting results to determine the parameters. The Monte Carlo prediction and the fitted curve agree very well.

The observed lifetime for $\mathrm{B_d}$ decays looks longer than those for B^+ and Λ_b decays. B^+ decays as $\mathrm{B}^+ \to \ell^+\nu\bar{\mathrm{D}}^0$ or $\ell^+\nu\bar{\mathrm{D}}^{*0}$. On the other hand, $\mathrm{B_d}$ decays as $\mathrm{B_d} \to \ell^+\nu\mathrm{D}^-$ or $\ell^+\nu\mathrm{D}^{*-}$. $\bar{\mathrm{D}}^{*0}$ and D^{*-} are unstable particles and immediately decay as $\bar{\mathrm{D}}^{*0} \to \bar{\mathrm{D}}^0\pi^0$ and $\mathrm{D}^{*-} \to \mathrm{D}^-\pi^0$ or $\bar{\mathrm{D}}^0\pi^-$ respectively. The lifetimes of $\bar{\mathrm{D}}^0$ and D^- are $\tau_{\bar{\mathrm{D}}^0} = 0.420 \pm 0.008$ psec and $\tau_{\mathrm{D}^-} = 1.066 \pm 0.023$ psec [10]. The lifetime of D^- is longer than one of $\bar{\mathrm{D}}^0$. Due to the difference of a lifetime between charm hadrons, the observed decay length for $\mathrm{B_d}$ decays becomes longer than those for B^+ and Λ_b decays since the charm decay products are included in the secondary vertex determination.

In order to remove the above lifetime bias, the correction factor, k_i, was introduced. This factor modified the distribution functions to be

$$f_i(t) = \frac{1}{k_i\tau_i}\int_0^\infty dt' e^{-\frac{t'}{k_i\tau_i}}\left\{b_i u_i\left(\sigma(t');t\right) + (1-b_i)v_i\left(\sigma'(t');t'-t\right)\right\}$$

$$\text{for } i = 4,5,6,7,8,9.$$

This factor was calculated for categories (4)-(9) form the Monte Carlo study. For categories (4)-(6), the correction factors also include the effect of a cascade decay.

On the other hand, for other proper time distributions the following function is used.

$$f_i(t) = \frac{1}{\tau_i}\int_0^\infty dt' e^{-\frac{t'}{\tau_i}}\left\{c_i\sum_{j=1}^{2} y_{ij}G(t;\sigma_{ij}) + (1-c_i)\sum_{j=1}^{2} y'_{ij}G(t;\sigma'_{ij}(t'))\right\}$$

$$\text{for } i = 1,2,3,10,$$

where $G(t;\sigma)$ denotes a 'standard' Gaussian, i.e., $G(t;\sigma) = \frac{1}{\sqrt{2\pi}\sigma}\exp(-\frac{t^2}{2\sigma^2})$. And $\sum_{j=1}^{2} y_{ij} = \sum_{j=1}^{2} y'_{ij} = 1$. The parameter $\sigma'_{ij}(t')$ is given by $\alpha_{ij} + \beta_{ij}t'$. The b_i, c_i, y_{ij} and y'_{ij} are parameters to be fixed using Monte Carlo samples. For $\mathrm{Z}^0 \to \mathrm{u\bar{u}}, \mathrm{d\bar{d}}, \mathrm{s\bar{s}}$ decays ($i = 1$) and an accidental reconstruction for $\mathrm{c\bar{c}}$ decays ($i = 3$) and $\mathrm{b\bar{b}}$ ($i = 10$), the first term in the function is dominant. But some vertices with a long decay time are observed due to $\mathrm{K_S^0}$ decays ($\mathrm{K_S^0} \to \pi^+\pi^-$) and Λ decays ($\Lambda \to \pi^- p$). In order to describe these decays the second term was introduced.

The fitted results are shown in figure 4.18 for the proper time distributions obtained from Monte Carlo samples with at least one reconstructed vertex in the event. The Monte Carlo prediction and the fitted curve for each category agree well.

Using the distribution functions the average B hadron lifetime was fitted using the events with at least one reconstructed secondary vertex to justify the parametrization. The fitted

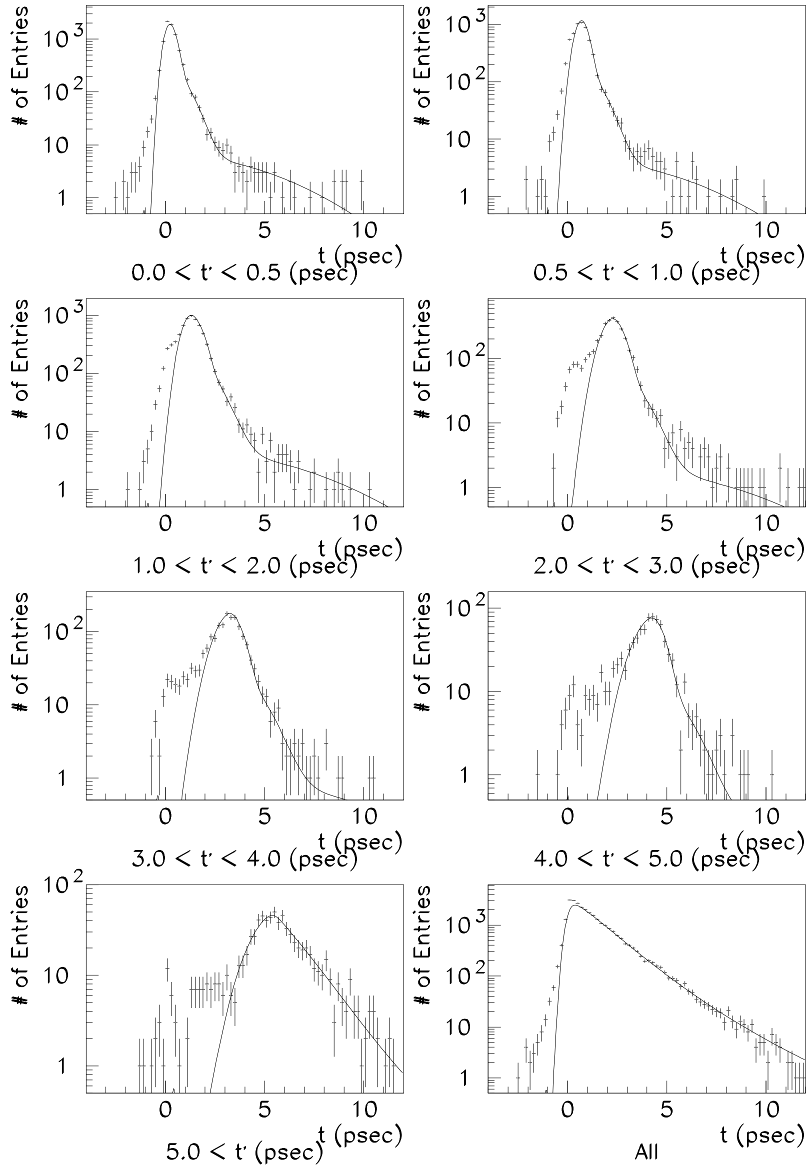

Figure 4.16: The observed proper time distribution with the calculated curve for each true proper time bin. The effect of the misreconstruction to the primary vertex is not taken into account yet. (Monte Carlo)

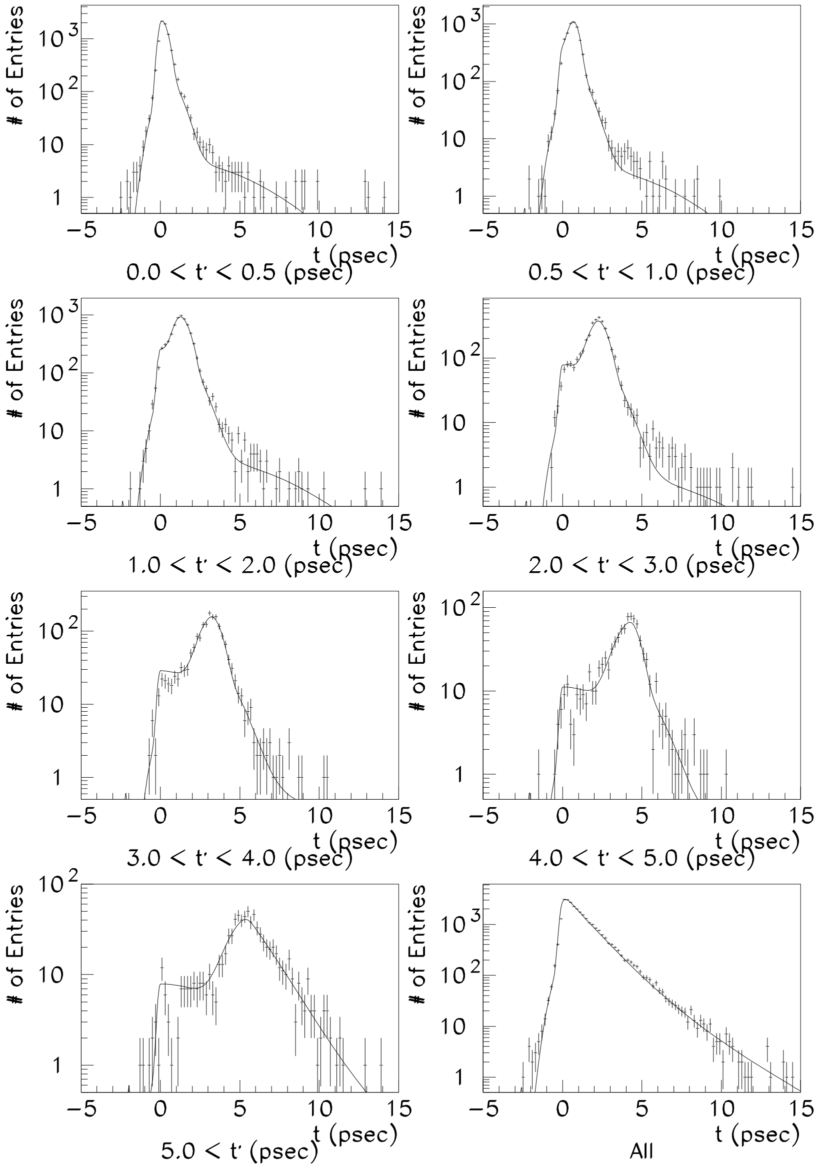

Figure 4.17: The observed proper time distribution with the calculated curve for each true proper time bin. (Monte Carlo)

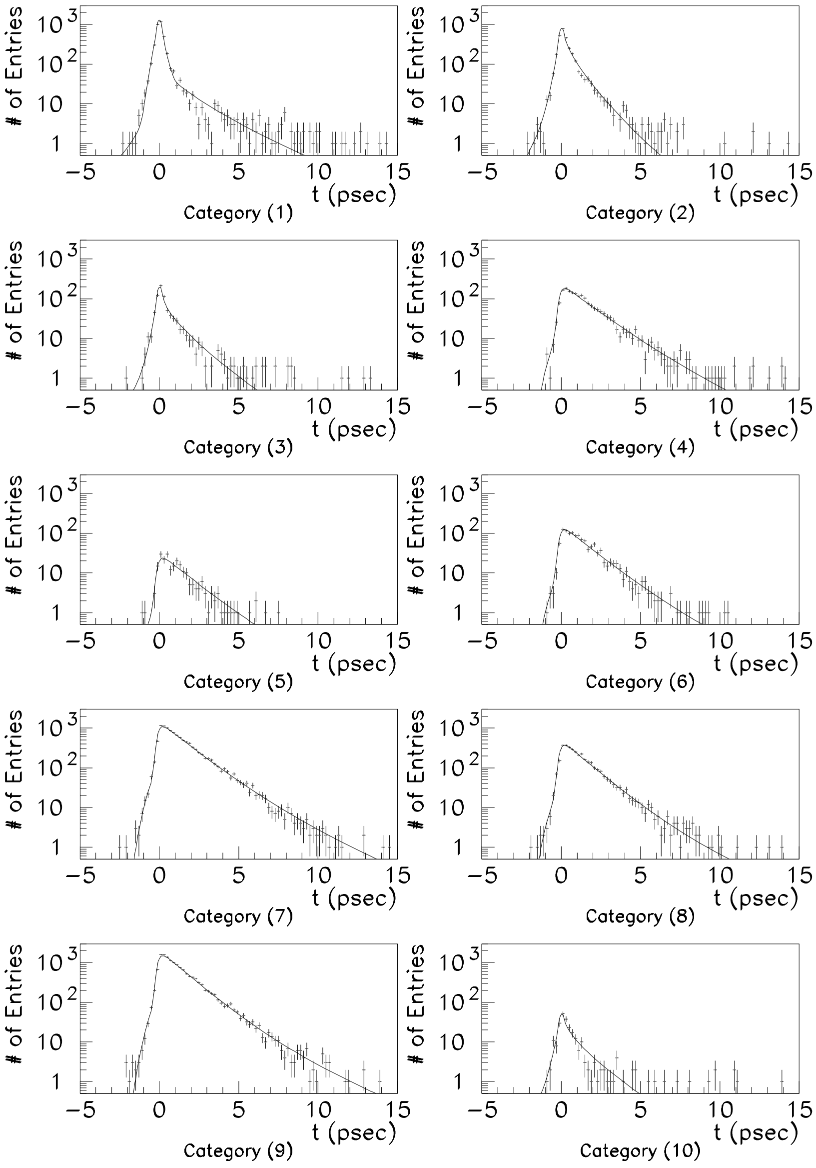

Category (1)

Category (2)

Category (3)

Category (4)

Category (5)

Category (6)

Category (7)

Category (8)

Category (9)

Category (10)

Figure 4.18: The observed and fitted proper time distributions for all categories for Monte Carlo samples.

results are 1.40 ± 0.01 psec for Monte Carlo samples and 1.57 ± 0.01 psec for real data. In figure 4.19, the observed proper time distributions with a fitted curve for both Monte Carlo samples and real data are shown. The observed distribution and the fitted curve agree very well. The lifetime 1.40 ± 0.01 psec for Monte Carlo samples is consistent with the given lifetime, 1.4 psec. The measured lifetime 1.57 ± 0.01 psec for real data is consistent with the LEP average lifetime. Thus the above mentioned fitting procedure are justified.

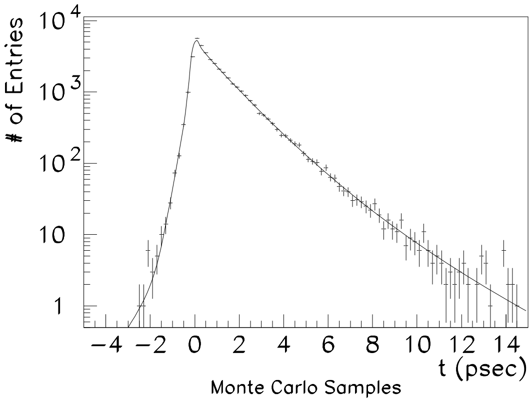

Monte Carlo Samples

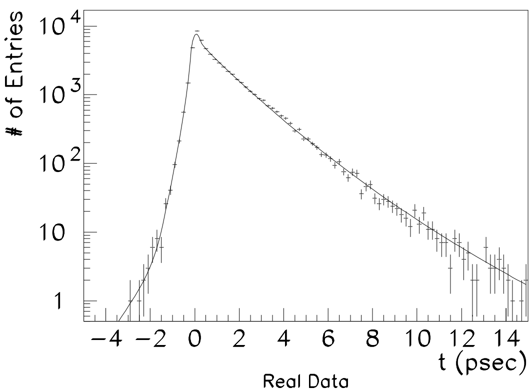

Real Data

Figure 4.19: The observed time distributions with the fitted curve using the events with at least one reconstructed secondary vertex for Monte Carlo samples and real data.

To estimate the fraction of $q\bar{q}$ pairs on dilepton events, $q\bar{q}$ pairs with at least one vertex were divided into $b\bar{b}$ pairs (N_b^{VTX}), $c\bar{c}$ pairs (N_c^{VTX}) and other pairs (N_l^{VTX}), where N_b^{VTX}, N_c^{VTX} and N_l^{VTX} are a number of vertices for each $q\bar{q}$ event type, respectively. And ϵ_b, ϵ_c and ϵ_l are the detection efficiencies for leptons coming from quark decays, ϵ_b for $b \to \ell$, ϵ_c for $c \to \ell$ and ϵ_l for $u, d, s \to \ell$. They are described as follows;

$$
\begin{aligned}
\epsilon_b &= \frac{N_b^{VTX}/\epsilon_b^{VTX}}{2N_{tot}R_{bb}} \\
\epsilon_c &= \frac{N_c^{VTX}/\epsilon_c^{VTX}}{2N_{tot}R_{cc}} \\
\epsilon_l &= \frac{N_l^{VTX}/\epsilon_l^{VTX}}{2N_{tot}(1 - R_{bb} - R_{cc})}
\end{aligned}
$$

where N_{tot} is the total number of multihadron events, $R_{bb} = \Gamma(\mathrm{Z}^0 \to \mathrm{b\bar{b}})/\Gamma(\mathrm{Z}^0 \to \mathrm{hadrons})$ $(= 0.2178)$ and $R_{cc} = \Gamma(\mathrm{Z}^0 \to \mathrm{c\bar{c}})/\Gamma(\mathrm{Z}^0 \to \mathrm{hadrons})$ $(= 0.1805)$ respectively [10]. ϵ_b^{VTX}, ϵ_c^{VTX} and ϵ_l^{VTX} are the efficiencies of the secondary vertex finder. Since the efficiencies for the secondary vertex finder for b $\to \ell$ and b $\to$ c $\to \ell$ are almost the same, the average value for these decay types is used. Numbers of $\mathrm{b\bar{b}}$ pair dilepton events ($N_{b\bar{b}}^{\geq 1VTX}$), $\mathrm{c\bar{c}}$ pair dilepton events ($N_{c\bar{c}}^{\geq 1VTX}$) and light $\mathrm{q\bar{q}}$ pair dilepton events ($N_{l\bar{l}}^{\geq 1VTX}$) with at least one secondary vertex are

$$\begin{aligned}
N_{b\bar{b}}^{\geq 1VTX} &= N_{tot} R_{bb} \epsilon_b^2 \left(1 - (1 - \epsilon_b^{VTX})^2\right) \\
N_{c\bar{c}}^{\geq 1VTX} &= N_{tot} R_{cc} \epsilon_c^2 \left(1 - (1 - \epsilon_c^{VTX})^2\right) \\
N_{l\bar{l}}^{\geq 1VTX} &= N_{tot}(1 - R_{bb} - R_{cc}) \epsilon_l^2 \left(1 - (1 - \epsilon_l^{VTX})^2\right).
\end{aligned}$$

So if the efficiency ϵ for each flavor is known, a number of dilepton events can be calculated. Taking into account a number of single lepton events that are estimated analytically, the following relations are given;

$$\begin{aligned}
N_{b\bar{b}}^{\geq 1VTX} &= N_{tot} R_{bb} \left(\frac{N_b^{VTX}/\epsilon_b^{VTX}}{2N_{tot}R_{bb}}\right)^2 \left(1 - (1 - \epsilon_b^{VTX})^2\right) \\
N_{c\bar{c}}^{\geq 1VTX} &= N_{tot} R_{cc} \left(\frac{N_c^{VTX}/\epsilon_c^{VTX}}{2N_{tot}R_{cc}}\right)^2 \left(1 - (1 - \epsilon_c^{VTX})^2\right) \\
N_{l\bar{l}}^{\geq 1VTX} &= N_{tot}(1 - R_{bb} - R_{cc}) \left(\frac{N_l^{VTX}/\epsilon_l^{VTX}}{2N_{tot}(1 - R_{bb} - R_{cc})}\right)^2 \left(1 - (1 - \epsilon_l^{VTX})^2\right).
\end{aligned}$$

Using information from Monte Carlo samples, the above numbers were estimated.

The fractions of each category for $\mathrm{c\bar{c}}$ and $\mathrm{b\bar{b}}$ dilepton samples are supposed to be the same as ones for single lepton samples. These fractions were defined as g_i $(i = 1 \ldots 10)$, which are normalized to be one for each flavor class, i.e.,

$$\begin{aligned}
&g_1 = 1 \quad \text{for light quark pairs} \\
&g_2 + g_3 = 1 \quad \text{for } \mathrm{c\bar{c}} \text{ pairs} \\
&g_4 + g_5 + g_6 + g_7 + g_8 + g_9 + g_{10} = 1 \quad \text{for } \mathrm{b\bar{b}} \text{ pairs}
\end{aligned}$$

In table 4.10, the estimated numbers from Monte Carlo samples are shown.

Using these parameters, the number of dilepton events with a category i for one thrust hemisphere and a category j for the other thrust hemisphere can be estimated without $\mathrm{B^0}$-$\mathrm{\bar{B}^0}$ mixing. The numbers of events for like-sign lepton events and unlike-sign lepton events were defined as $\xi_{i,j}$ and $\eta_{i,j}$ respectively. For example, the event with a category (7) for both thrust hemispheres is considered. In this case, this event is necessarily observed as an unlike-sign lepton event, so that $\xi_{7,7} = N_{bb} g_7^2$ and $\eta_{7,7} = 0$. And for the event with a category (4) in one thrust hemisphere and a category (7) in the other, this event is necessarily observed as a like-sign lepton event, so that $\xi_{4,7} = 0$ and $\eta_{4,7} = N_{bb} g_4 g_7$. In table 4.11, the predicted events with a category i and j ($\xi_{i,j}$ for unlike-sign lepton events and $\eta_{i,j}$ for like-sign lepton events) are summarized.

Now $\mathrm{B^0}$-$\mathrm{\bar{B}^0}$ mixing was taken into account.

The $\mathrm{B^0}$-$\mathrm{\bar{B}^0}$ mixing should be taken into account in Categories (4), (5), (7) and (9). Then the proper time distributions for these categories have to be modified. These distributions were

Primary flavor	Fraction of inclusive lepton	Fraction in dilepton events	Fraction for each flavor class
light quark decays	$r_{\mathrm{u,d,s}} = 0.089$	$r_{\mathrm{u\bar{u},d\bar{d},s\bar{s}}} = 0.009$	$g_1 = 1.000$
$\mathrm{c\bar{c}}$ decays	$r_{\mathrm{c}} = 0.096$	$r_{\mathrm{c\bar{c}}} = 0.029$	$g_2 = 0.784$ $g_2 = 0.216$
$\mathrm{b\bar{b}}$ decays	$r_{\mathrm{b}} = 0.815$	$r_{\mathrm{b\bar{b}}} = 0.962$	$g_4 = 0.041$ $g_5 = 0.006$ $g_6 = 0.027$ $g_7 = 0.350$ $g_8 = 0.112$ $g_9 = 0.454$ $g_{10} = 0.010$

Table 4.10: Fraction of the $\mathrm{q\bar{q}}$ pair events in single lepton or dilepton events and g-factors which are the fraction in each flavor class.

$\xi_{i,j}$	(1)	(2)	(3)	(4)	(5)	(6)	(7)	(8)	(9)	(10)
(1)	$\frac{N_{ll}}{2}$	-	-	-	-	-	-	-	-	-
(2)	-	$N_{cc}g_2^2$	$\frac{N_{cc}g_2g_3}{2}$	-	-	-	-	-	-	-
(3)	-	$\frac{N_{cc}g_3g_2}{2}$	$\frac{N_{cc}g_3^2}{2}$	-	-	-	-	-	-	-
(4)	-	-	-	$N_{bb}g_4^2$	$N_{bb}g_4g_5$	$N_{bb}g_4g_6$	-	-	-	$\frac{N_{bb}g_4g_{10}}{2}$
(5)	-	-	-	$N_{bb}g_5g_4$	$N_{bb}g_5^2$	$N_{bb}g_5g_6$	-	-	-	$\frac{N_{bb}g_4g_{10}}{2}$
(6)	-	-	-	$N_{bb}g_6g_4$	$N_{bb}g_6g_5$	$N_{bb}g_6^2$	-	-	-	$\frac{N_{bb}g_4g_{10}}{2}$
(7)	-	-	-	-	-	-	$N_{bb}g_7^2$	$N_{bb}g_7g_8$	$N_{bb}g_7g_9$	$\frac{N_{bb}g_7g_{10}}{2}$
(8)	-	-	-	-	-	-	$N_{bb}g_8g_7$	$N_{bb}g_8^2$	$N_{bb}g_8g_9$	$\frac{N_{bb}g_8g_{10}}{2}$
(9)	-	-	-	-	-	-	$N_{bb}g_9g_7$	$N_{bb}g_9g_8$	$N_{bb}g_9^2$	$\frac{N_{bb}g_9g_{10}}{2}$
(10)	-	-	-	$\frac{N_{bb}g_{10}g_4}{2}$	$\frac{N_{bb}g_{10}g_5}{2}$	$\frac{N_{bb}g_{10}g_6}{2}$	$\frac{N_{bb}g_{10}g_7}{2}$	$\frac{N_{bb}g_{10}g_8}{2}$	$\frac{N_{bb}g_{10}g_9}{2}$	$\frac{N_{bb}g_{10}^2}{2}$

$\eta_{i,j}$	(1)	(2)	(3)	(4)	(5)	(6)	(7)	(8)	(9)	(10)
(1)	$\frac{N_{ll}}{2}$	-	-	-	-	-	-	-	-	-
(2)	-	-	$\frac{N_{cc}g_2g_3}{2}$	-	-	-	-	-	-	-
(3)	-	$\frac{N_{cc}g_3g_2}{2}$	$\frac{N_{cc}g_3^2}{2}$	-	-	-	-	-	-	-
(4)	-	-	-	-	-	-	$N_{bb}g_4g_7$	$N_{bb}g_4g_8$	$N_{bb}g_4g_9$	$\frac{N_{bb}g_4g_{10}}{2}$
(5)	-	-	-	-	-	-	$N_{bb}g_5g_7$	$N_{bb}g_5g_8$	$N_{bb}g_5g_9$	$\frac{N_{bb}g_5g_{10}}{2}$
(6)	-	-	-	-	-	-	$N_{bb}g_6g_7$	$N_{bb}g_6g_8$	$N_{bb}g_6g_9$	$\frac{N_{bb}g_6g_{10}}{2}$
(7)	-	-	-	$N_{bb}g_7g_4$	$N_{bb}g_7g_5$	$N_{bb}g_7g_6$	-	-	-	$\frac{N_{bb}g_7g_{10}}{2}$
(8)	-	-	-	$N_{bb}g_8g_4$	$N_{bb}g_8g_5$	$N_{bb}g_8g_6$	-	-	-	$\frac{N_{bb}g_8g_{10}}{2}$
(9)	-	-	-	$N_{bb}g_9g_4$	$N_{bb}g_9g_5$	$N_{bb}g_9g_6$	-	-	-	$\frac{N_{bb}g_9g_{10}}{2}$
(10)	-	-	-	$\frac{N_{bb}g_{10}g_4}{2}$	$\frac{N_{bb}g_{10}g_5}{2}$	$\frac{N_{bb}g_{10}g_6}{2}$	$\frac{N_{bb}g_{10}g_7}{2}$	$\frac{N_{bb}g_{10}g_8}{2}$	$\frac{N_{bb}g_{10}g_9}{2}$	$\frac{N_{bb}g_{10}^2}{2}$

Table 4.11: The expected numbers of events with the category i in one hemisphere and the category j in the other hemisphere without $\mathrm{B^0}$-$\mathrm{\bar{B}^0}$ mixing. N_{bb}, N_{cc} and N_{ll} mean $N_{b\bar{b}}^{\geq 1VTX}$, $N_{b\bar{b}}^{\geq 1VTX}$ and $N_{b\bar{b}}^{\geq 1VTX}$, respectively.

divided into two terms; i.e., one term which describes the case where $\mathrm{B^0}$-$\mathrm{\bar{B}^0}$ mixing happened and the tagged lepton charge flipped, and the other term describes the case where $\mathrm{B^0}$-$\mathrm{\bar{B}^0}$ mixing did not happen. The function f_i ($i = 4, 5, 7$ and 8) is divided as follows;

$$f_i(t) = f_i^{NOMIX} + f_i^{MIX}$$

where

$$\begin{aligned} f_i^{NOMIX}(t) &= \frac{1}{k_i\tau_i}\int_0^\infty dt' e^{-\frac{t'}{k_i\tau_i}}\left\{(1-\chi_i)b_i u_i\left(\sigma(t');t\right) + (1-b_i)v_i\left(\sigma(t');t'-t\right)\cos^2(\frac{\Delta m_i}{2}t')\right\} \\ f_i^{MIX}(t) &= \frac{1}{k_i\tau_i}\int_0^\infty dt' e^{-\frac{t'}{k_i\tau_i}}\left\{\chi_i b_i u_i\left(\sigma(t');t\right) + (1-b_i)v_i\left(\sigma(t');t'-t\right)\sin^2(\frac{\Delta m_i}{2}t')\right\} \end{aligned}$$

and $\chi_i = \chi_d$ and $\Delta m_i = \Delta m_d$ for $i = 4, 7$ and $\chi_i = \chi_s$ and $\Delta m_i = \Delta m_s$ for $i = 5, 8$. The function $\tilde{f}_i$ was defined as the modified proper time distribution of f_i, given by

$$g_i\tilde{f}_i(t) = g_i f_i^{NOMIX}(t) + g_j f_j^{MIX}(t)$$

where $(i, j) = (4, 7), (7, 4)$ for $\mathrm{B_d}$-$\mathrm{\bar{B}_d}$ mixing and $(i, j) = (5, 8), (8, 5)$ for $\mathrm{B_s}$-$\mathrm{\bar{B}_s}$ mixing. But, $\tilde{f}_i(t)$ was redefined so as to be normalized to be unity, i.e., $\tilde{f}_i(t)/\int dt\tilde{f}_i(t) \to \tilde{f}_i(t)$.

For other categories$(1, 2, 3, 6, 9$ and $10)$, $\tilde{f}_i(t)$ was defined as $f_i(t)$, i.e.,

$$\tilde{f}_i(t) = f_i(t)$$

Then a number of events with two vertices which have measured proper times t_1 in one hemisphere (category i) and t_2 in the other hemisphere (category j) can be obtained. These numbers were defined as $F^2_{i,j}(t_1, t_2)$ for unlike-sign lepton events and $G^2_{i,j}(t_1, t_2)$ for like-sign lepton events, so that

$$\begin{aligned} F^2_{i,j}(t_1, t_2) &= \xi_{i,j}\tilde{f}_i(t_1)\tilde{f}_j(t_2) \\ G^2_{i,j}(t_1, t_2) &= \eta_{i,j}\tilde{f}_i(t_1)\tilde{f}_j(t_2). \end{aligned}$$

If one vertex was not reconstructed unfortunately, these numbers were defined as $F^1_{i,j}(t)$ for unlike-sign lepton events and $G^1_{i,j}(t)$ for like-sign lepton events, so that

$$\begin{aligned} F^1_{i,j}(t) &= (\xi_{i,j}(\int_{-\infty}^{+\infty}\tilde{f}_i(t_1)dt_1\tilde{f}_j(t) + \tilde{f}_i(t)\int_{-\infty}^{+\infty}\tilde{f}_j(t_2)dt_2)) \\ G^1_{i,j}(t) &= (\eta_{i,j}(\int_{-\infty}^{+\infty}\tilde{f}_i(t_1)dt_1\tilde{f}_j(t) + \tilde{f}_i(t)\int_{-\infty}^{+\infty}\tilde{f}_j(t_2)dt_2)). \end{aligned}$$

Proper time distributions for events with two vertices are obtained by

$$\begin{aligned} F^2(t_1, t_2) &= \sum_{i,j} F^2_{i,j}(t_1, t_2) \\ G^2(t_1, t_2) &= \sum_{i,j} G^2_{i,j}(t_1, t_2) \end{aligned}$$

for unlike-sign lepton events and like-sign lepton events, respectively. And for events with one vertex

$$\begin{aligned} F^1(t) &= \sum_{i,j} F^1_{i,j}(t) \\ G^1(t) &= \sum_{i,j} G^1_{i,j}(t) \end{aligned}$$

are given for unlike-sign lepton events and like-sign lepton events respectively.

Finally, a total likelihood function is given by

$$\mathcal{L}(\Delta m_d, \Delta m_s) = \prod_{i_1=1}^{N_1^{LS}} F^1(t_{i_1}) \prod_{j_2=1}^{N_1^{US}} G^1(t_{j_1}) \prod_{i_1=1}^{N_2^{LS}} F^2(t_{i_1}, t_{i_2}) \prod_{j_2=1}^{N_2^{US}} G^2(t_{j_1}, t_{j_2})$$

as a function of Δm_d and Δm_s, where $N_1^{LS}(N_1^{US})$ is a number of like-sign (unlike-sign) lepton events with one vertex and $N_2^{LS}(N_2^{US})$ is a number of like-sign (unlike-sign) lepton events with two vertices.

4.8.2 Δm_d Measurement

Dilepton events with at least one secondary vertex were selected in the sample of about 1.5 million multihadronic events. A number of selected dilepton events is 921 for like-sign lepton events and 2044 for unlike-sign lepton events. A number of the thrust hemisphere in which the secondary vertex was reconstructed successfully is 1460 for like-sign lepton events and 3261 for unlike-sign lepton events. A number of events with two reconstructed vertices is 539 for the like-sign lepton events and 1217 for the unlike-sign lepton events. In table 4.12, numbers of dilepton events for possible combinations of tagged leptons are summarized.

	e-e	e-μ	μ-μ	total	total vertices
unlike-sign	446	978	620	2044	3261
like-sign	206	426	289	921	1460

Table 4.12: The number of selected dilepton events for real data. e-e, e-μ and μ-μ mean the combination of the tagged leptons, where e is an electron and μ is a muon.

The mass difference for B_d, Δm_d, was extracted by fitting both observed proper time distributions for like-sign and unlike-sign lepton events simultaneously, with Δm_s fixed to be 10 psec^{-1} corresponding to $\chi_s \sim 0.5$.

The cascade decay fraction and B_s fraction were also fitted simultaneously under Gaussian constraint to reduce the total error. The uncertainty of the cascade decay fraction is estimated to be ±15% of its nominal value, which was obtained from Monte Carlo study. This includes uncertainties due to branching fraction, modeling effect and the kinematic selection.

The uncertainty on the B_s fraction is taken to be ±30% of its nominal value, which was obtained from Monte Carlo study.

The measurements from references [84] yield a combined branching fraction for $b \to \bar{B}_s \to D_s \ell^- \bar{\nu} X \to \phi\pi^+ \ell^- \bar{\nu} X$ to be $(4.8 \pm 1.0) \times 10^{-4}$. Dividing this by $B(D_s \to \phi\pi^+) = 3.6 \pm 0.6\%$ [10] gives $B(b \to \bar{B}_s \to D_s \ell^- \bar{\nu} X) = 1.33 \pm 0.36\%$. The branching fraction for $\bar{B}_s \to D_s \ell^- \bar{\nu} X$ is likely to be less than $B(\bar{B}_s \to \ell^- \bar{\nu} X)$ due to the presence of decays of the type $\bar{B}_s \to D_s^{**} \ell^- \bar{\nu} X$, since $D_s^{**} \to D_s \pi$ is forbidden by isospin conservation. Supposing B_s decays including D_s^{**} to be 30 ± 10 % is consistent with the relative production fraction of D_s^{**} in semileptonic B_s and B^+ decays [85]. Taking the above assumption and $B(\bar{B} \to \ell^- \bar{\nu} X)$ of $11.0 \pm 0.5\%$ yields $B(b \to \bar{B}_s) = 0.17 \pm 0.05$.

$B(b \to \bar{B}_s)$ can be also estimated from $\bar{\chi} = f_d \chi_d + f_s \chi_s$. Using $\bar{\chi} = 0.119 \pm 0.009$ [14] and a χ_d measurement [86], $B(b \to \bar{B}_s) = 0.11 \pm 0.03$ for $\chi_s \sim 0.5$. The semileptonic branching ratios for B_d and B_s are supposed to be equal.

By averaging these values, $B(b \to \bar{B}_s) = 0.13 \pm 0.03$ is obtained. This value is consistent with $B(b \to \bar{B}_s) = 0.12 \pm 0.036$ which is used in this analysis.

Finally, the fitted value of Δm_d is

$$\Delta m_d = 0.462 \pm 0.057 \text{ psec}^{-1}.$$

This error is a fitting error only. The fitted value of the cascade fraction was 1.05 ± 0.14 of its nominal value and the fitted value of the fraction of leptons from B_s decays was 1.23 ± 0.21 of its nominal value. In figure 4.20, the proper time distributions for unlike-sign lepton events and like-sign lepton events are shown together with the fitted curves. The observed proper time distribution and the predicted curve agree very well.

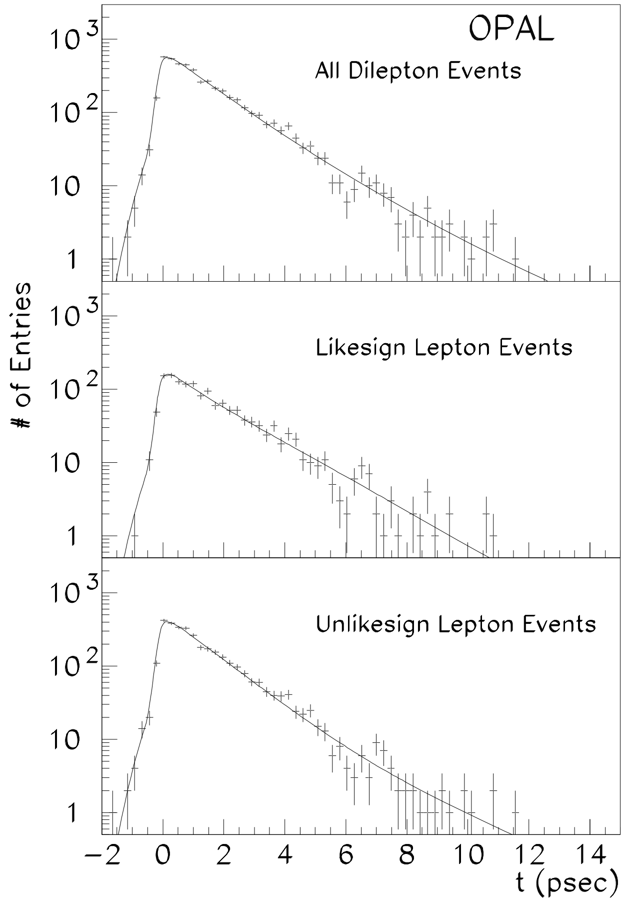

Figure 4.20: The observed proper time distribution with the fitted curve in case of the optimal value for all events (top), unlike-sign lepton events (center) and like-sign lepton events (bottom).

To illustrate a time dependent B_d oscillation, a fraction of like-sign leptons as a function of decay proper time was defined as

$$R(t) = \frac{N^{++,--}(t)}{N^{+-,-+}(t) + N^{++,--}(t)}.$$

In figure 4.21, the obtained $R(t)$ values are plotted together with the prediction curve for the optimal value of Δm_d. The prediction and data agree very well. The prediction without $\mathrm{B_d}$ mixing is shown in the same figure by a dashed line.

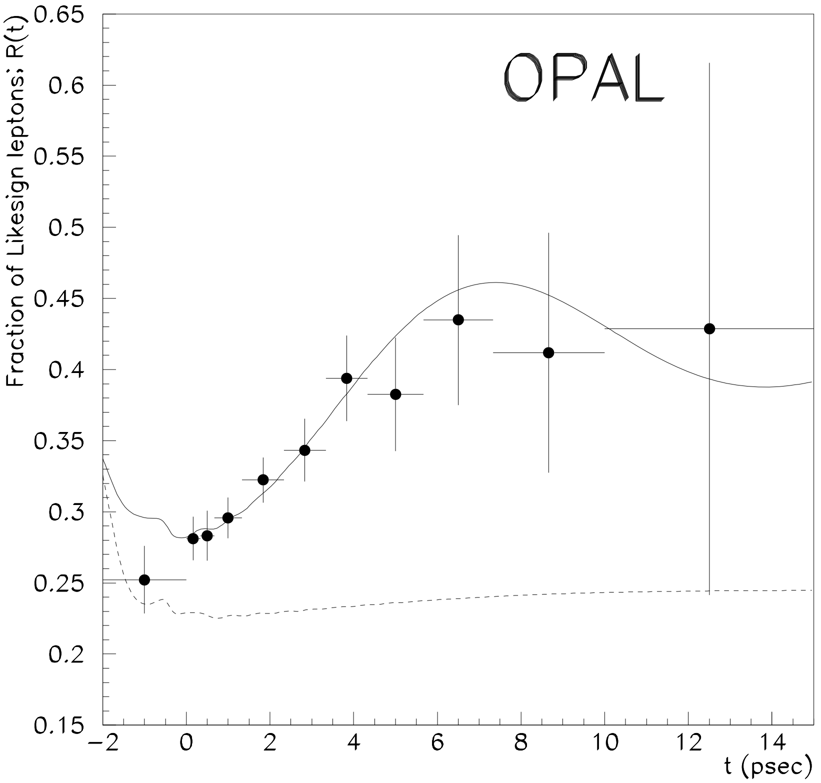

Figure 4.21: The fraction of the like-sign lepton events as a function of the observed proper time. The points with error bar are for data. The solid line is the prediction with the optimum value and the dashed line is the prediction without $\mathrm{B_d}$ mixing. The $\mathrm{B_s}$ mixing is supposed to be 10 psec^{-1}.

The mass differences Δm_d and Δm_s were fitted simultaneously using the likelihood function with the cascade decay fraction and the fraction of leptons from $\mathrm{B_s}$ decays fixed to the nominal values. In figure 4.22, the likelihood contour plot on Δm_d versus Δm_s is shown. The solid lines indicate $\ln(\mathcal{L}_{max}/\mathcal{L})$ corresponding to 1σ, 2σ and so on, where $\mathcal{L}_{max}$ is a maximum likelihood value. The best fitting point of this likelihood function is $(\Delta m_s, \Delta m_d) = (7.75\ \mathrm{psec}^{-1}, 0.513\ \mathrm{psec}^{-1})$. In the region of $\Delta m_s > \sim 2\ \mathrm{psec}^{-1}$, Δm_d and Δm_s are decoupled.

The reasons why the fraction of like-sign lepton events is not zero in the case of $\Delta m_d = 0.0\ \mathrm{psec}^{-1}$ are given as follows. One reason is due to the light quark decays. The long-lived particles are hardly generated by the light quark decays. So these reconstructed secondary vertices are due to the accidental reconstruction. The sign of a tagged lepton does not correlate to the sign of the parent quark. In this case, the probability that they are observed as a like-sign lepton event is the same as the probability that they are observed as an unlike-sign lepton

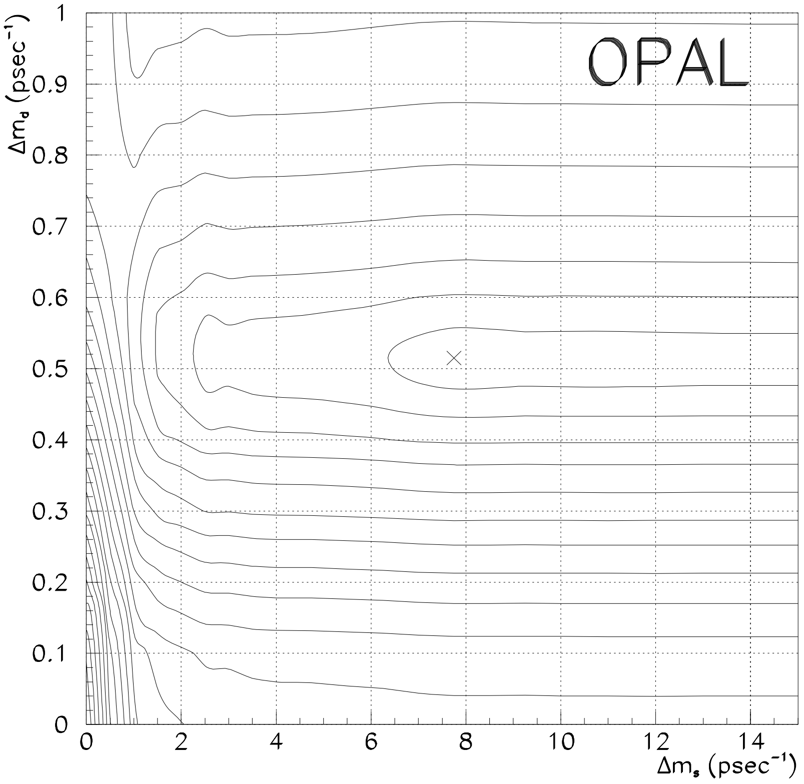

Figure 4.22: The contour plot on Δm_d versus Δm_s. The minimum point is $(\Delta m_d, \Delta m_s) =$ (7.75 psec^{-1}, 0.513 psec^{-1}).

event. The other reason is due to the cascade decay leptons. Even if there is no B mixing, events are observed as a like-sign event in case a direct decay lepton and a cascade decay lepton are tagged.

The fitting error includes the statistical error and the systematic errors due to uncertainties on the cascade fraction and the B_s fraction. So, the fitting error should be divided into a statistical error and a systematic error. To do that, three parameter fitting was iterated by changing the cascade decay fraction or the B_s fraction within $\pm 1\sigma$ from its nominal value. As a result, the statistical error is estimated to be $^{+0.040}_{-0.053}$ psec^{-1} and the systematic error related to these fractions is $^{+0.042}_{-0.019}$ psec^{-1}.

Systematic errors on Δm_d other than the cascade decay fraction and the production rate of B_s were estimated by varying corresponding parameters. The summary of the systematic errors is listed in table 4.13.

Source of uncertainty	$\delta(\Delta m_d)$ psec^{-1}
cascade decay fraction ($\pm 15\%$)	$^{+0.015}_{-0.007}$
B_s fraction ($\pm 30\%$)	$^{+0.039}_{-0.018}$
resolution function ($\pm 14\%$)	$^{+0.003}_{-0.002}$
lepton misidentification (e:$\pm 30\%$, μ:$\pm 20\%$)	± 0.011
charm background ($\pm 30\%$)	$^{+0.005}_{-0.004}$
b-baryon fraction (± 0.04)	$^{+0.013}_{-0.011}$
$b \to D^{**}$ decays	-0.008
$\tau_{B^+}/\tau_{B_d} = 1.01 \pm 0.11$	$^{+0.020}_{-0.023}$
$\tau_{B_s}/\tau_{B_d} = 0.99 \pm 0.18$	$^{+0.005}_{-0.003}$
$\tau_{\Lambda_b}/\tau_{B_d} = 0.69 \pm 0.12$	$^{+0.004}_{-0.003}$
$\Delta m_s = 2 - 20$ psec^{-1}	$^{+0.012}_{-0.000}$
Total systematic error	$^{+0.052}_{-0.035}$

Table 4.13: The summary on the systematic error for the Δm_d measurement.

Systematic errors due to various sources were estimated as follows,

Resolution: Taking into account the uncertainty of the detector resolution, the resolution was varied by $\pm 14\%$ [87]. To study this systematic error, three likelihood functions with a different smearing factor were prepared. An estimated systematic error due to the uncertainty of the resolution function was $\delta(\Delta m_d) = \; ^{+0.003}_{-0.002}$ psec^{-1}.

Lepton misidentifications: By the study of the lepton identification for electrons and muons, the uncertainty of the lepton misidentification was estimated to be $\pm 30\%$ for electrons and $\pm 20\%$ for muons. An estimated systematic error was $\delta(\Delta m_d) = \pm 0.011$ psec^{-1}.

Background of $c\bar{c}$ *pairs*: This uncertainty of $c\bar{c}$ background fraction was estimated to be $\pm 30\%$ due to the uncertainties on the branching fraction of $Z^0 \to c\bar{c}$ and the modeling effect of the semileptonic decays of charm decays. A systematic error was $\delta(\Delta m_d) = \; ^{+0.005}_{-0.004}$ psec^{-1}.

Uncertainty of a fraction of b-baryon: The uncertainty of the fraction of b-baryon production was estimated to be ± 0.04 [88] from the analysis of $\Lambda \ell$ correlation. An estimated systematic error was $\delta(\Delta m_d) = \; ^{+0.013}_{-0.011}$ psec^{-1}.

Uncertainty of $b \to D^{**}$: The decay mode of $b \to D^{**}$ is not included in the Monte Carlo samples. The contribution due to D^{**} was estimated by the contamination of D^{**} in multihadronic events. An estimated systematic error was $\delta(\Delta m_d) = -0.008$ psec^{-1}.

Uncertainty of B hadron lifetimes: The uncertainties for all cases are derived on the experimental results as described in table 4.4. An estimated systematic error was $\delta(\Delta m_d) = {}^{+0.020}_{-0.023}$ psec^{-1} for $\tau_{\mathrm{B}^+}/\tau_{\mathrm{B_d}}$, $\delta(\Delta m_d) = {}^{+0.005}_{-0.003}$ psec^{-1} for $\tau_{\mathrm{B_s}}/\tau_{\mathrm{B_d}}$ and $\delta(\Delta m_d) = {}^{+0.004}_{-0.003}$ psec^{-1} for $\tau_{\Lambda_b}/\tau_{\mathrm{B_d}}$.

Uncertainty of Δm_s: The standard model predicts $\chi_s = \frac{1}{2}\frac{(\Delta m_s \tau_{\mathrm{B_s}})^2}{1+(\Delta m_s \tau_{\mathrm{B_s}})^2} \sim 0.5$. In order to estimate this error, Δm_s was varied from $\Delta m_s = 2$ psec^{-1} to $\Delta m_s = 20$ psec^{-1}. An estimated systematic error was $\delta(\Delta m_d) = {}^{+0.012}_{-0.000}$ psec^{-1}.

These estimated errors were added in quadrature and the total systematic error was obtained. The estimated total systematic error is $\delta(\Delta m_d) = {}^{+0.052}_{-0.035}$ psec^{-1}.

So, the observed Δm_d is

$$\Delta m_d = 0.462 \; {}^{+0.040}_{-0.053} \; {}^{+0.052}_{-0.035} \; \mathrm{psec}^{-1},$$

where the first error is the statistical error and the second error is the systematic error.

4.8.3 Limit on Δm_s

In order to set the lower limit on Δm_s, the observed proper time distributions for the unlike-sign and like-sign lepton events were fitted by the likelihood function with one parameter, Δm_s. The parameter Δm_d was kept free under a Gaussian constraint. The constraint for Δm_d was estimated by the LEP results on B oscillation. But the analysis using dilepton events was not included because this analysis has already an effect from Δm_s. The LEP average of Δm_d is $\Delta m_d = 0.52 \pm 0.05$ psec^{-1}. This error includes both statistical and systematic errors.

The lower limit at 95% confidence level (denoted as 95% C.L.) was obtained as the points which satisfied with $\ln(\mathcal{L}_{max}/\mathcal{L}) = 1.92$, because the likelihood function is treated as a Gaussian distribution around the point, $\mathcal{L}_{max}$, where $\mathcal{L}_{max}$ means the maximum value of the likelihood function. In the case of a Gaussian distribution the region outside of $\pm 1.96\sigma$ is rejected at 95% C.L.

In order to study the sensitivity for setting the lower limit on Δm_s, a tremendous amount of sets of the Monte Carlo data samples were needed. Then the simplified 'Toy Monte Carlo' was developed to generate events. This Toy Monte Carlo simulates the observed proper time distributions for each event type, unlike-sign lepton and like-sign lepton events, depending on the measured proper time distributions from the real data analysis. The fractions of the unlike-sign and like-sign lepton events were a function of the mixing parameters, Δm_d and Δm_s. The proper time distributions generated by the Toy Monte Carlo and the distributions obtained from real data were compared. In figure 4.23, the proper time distributions from this Toy Monte Carlo are shown with one set of parameters. The prediction from this Toy Monte Carlo and the distribution obtained from real data analysis agree well.

A total of 200 data sets were generated each for $(\Delta m_d, \Delta m_s) = (0.5\ \mathrm{psec}^{-1}, 1.0\ \mathrm{psec}^{-1})$, $(0.5\ \mathrm{psec}^{-1}, 2.0\ \mathrm{psec}^{-1})$, $(0.5\ \mathrm{psec}^{-1}, 4.0\ \mathrm{psec}^{-1})$ and $(0.5\ \mathrm{psec}^{-1}, 15.0\ \mathrm{psec}^{-1})$. One data set contains dilepton events comparable with the real data. These data sets were fitted by the likelihood function as a function of Δm_s. In figure 4.24, the results are summarized. The first column shows the fitted Δm_s distributions. The second column shows the $\Delta \ln \mathcal{L}$ distributions, where $\Delta \ln \mathcal{L} = \ln(\mathcal{L}_{max}/\mathcal{L})$. There are about 95% of events in the region of $\Delta \ln \mathcal{L} < 1.92$. The third column shows the lower limit on Δm_s at 95% C.L.. In case Δm_s is lass than $\sim$4 psec^{-1} it might be possible to determine Δm_s. But in case Δm_s is greater than $\sim$4 psec^{-1} the sensitivity of Δm_s measurement is lost due to a large frequency of the $\mathrm{B_s}$ mixing.

In figure 4.25, the log-likelihood value is shown as a function of Δm_s for the real data. The dashed line stands for the case without taking the systematic error into account. In this case,

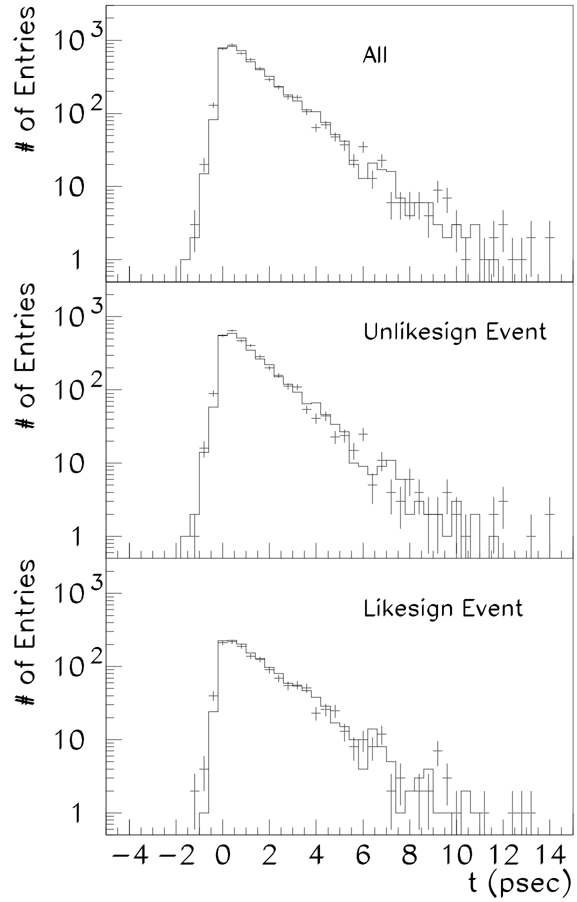

Figure 4.23: Comparison with the proper time distribution of Toy Monte Carlo and one of real data. For Toy Monte Carlo samples, the Δm_d and Δm_s are set to 0.5 psec^{-1} and 15.0 psec^{-1} respectively.

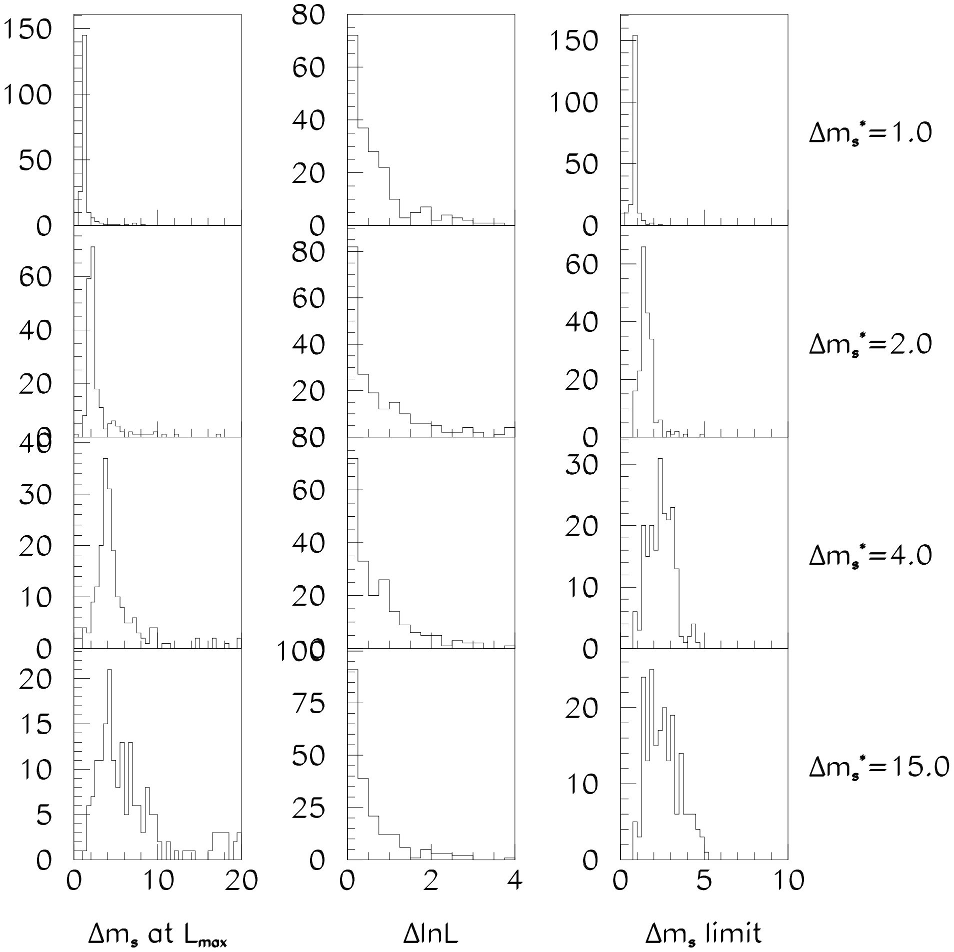

Figure 4.24: Sensitivity on studying B$_s$ mixing using the Toy Monte Carlo. Three parameter are described in the text.

the limit on Δm_s was obtained to be $\Delta m_s > 2.3$ psec^{-1} at 95% C.L.

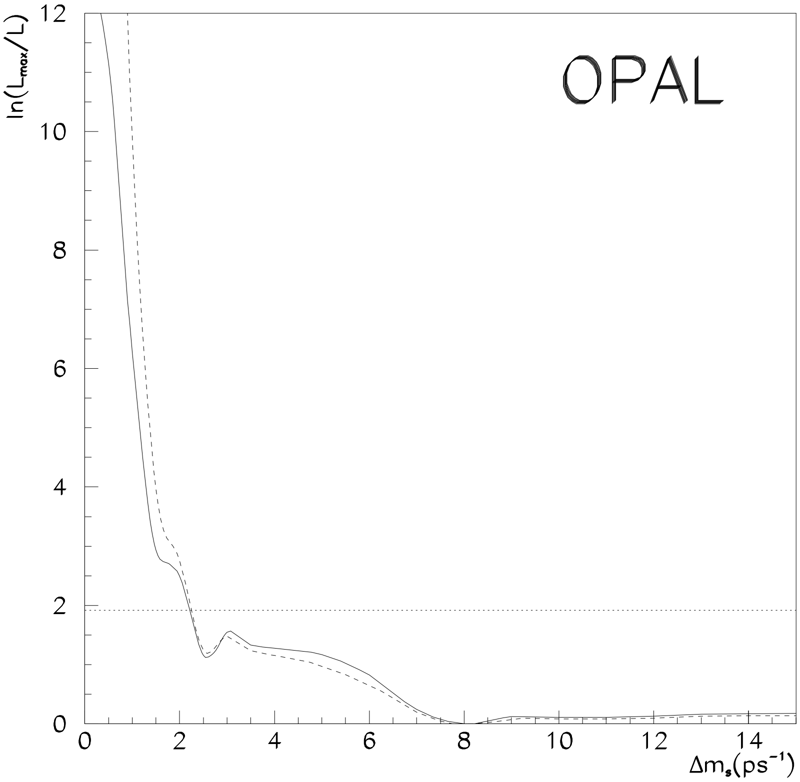

Figure 4.25: The log-likelihood function as a function of Δm_s. The solid line is for the case of taking into account the systematic effects and the dashed line is for the case without systematic effects. The dotted line, $\ln(\mathcal{L}_{max}/\mathcal{L}) = 1.92$ shows the 95% C.L.

Next, the limit on Δm_s was calculated taking into account systematic fluctuation on several parameters, i.e., lifetimes and ratios of B hadrons, the cascade fraction and so on. In this case, the result is shown in figure 4.25 by the solid line. The lower limit on Δm_s at 95% confidence level was obtained,

$$\Delta m_s > 2.2 \text{ psec}^{-1} \qquad \text{at 95\% C.L.}$$

Chapter 5

Discussion

5.1 Comparison with results from other experiments

In figure 5.1 and table 5.1, the Δm_d measurements are summarized. The result from this analysis is consistent with the previous results from other LEP experiments. For results from ALEPH, only 1991 and 1992 data were used. At present, the total error from our measurement is the smallest.

In table 5.2, the results of the lower limit on Δm_s are summarized. The lower limit on Δm_s from this analysis is consistent with the previous result from ALEPH. If a new secondary vertex finder with lower misreconstruction probability were developed, the lower limit from this OPAL result would be improved.

	Type	Δm_d (psec^{-1})	Ref.
ALEPH	$D^* + \ell$	$0.52\,^{+0.10}_{-0.11}\,^{+0.04}_{-0.03}$	[4]
ALEPH	Dilepton	$0.50\,^{+0.07}_{-0.06}\,^{+0.11}_{-0.10}$	[5]
DELPHI	D^* + Jet charge (Q_{jet})	$0.52 \pm 0.12 \pm 0.06$	[8]
OPAL	$D^* + \ell$	$0.57 \pm 0.11 \pm 0.02$	[6]
OPAL	$D^*\ell$ + Jet charge (Q_{jet})	$0.508 \pm 0.75 \pm 0.025$	[7]
OPAL	Dilepton	$0.462\,^{+0.040}_{-0.053}\,^{+0.052}_{-0.035}$	This analysis

Table 5.1: The comparison with previous Δm_d measurement.

	Type	Lower limit on Δm_s (psec^{-1})	Ref.
ALEPH	Dilepton	2.0 (95% C.L.)	[4]
OPAL	Dilepton	2.2 (95% C.L.)	This analysis

Table 5.2: The comparison with the lower limit on Δm_s.

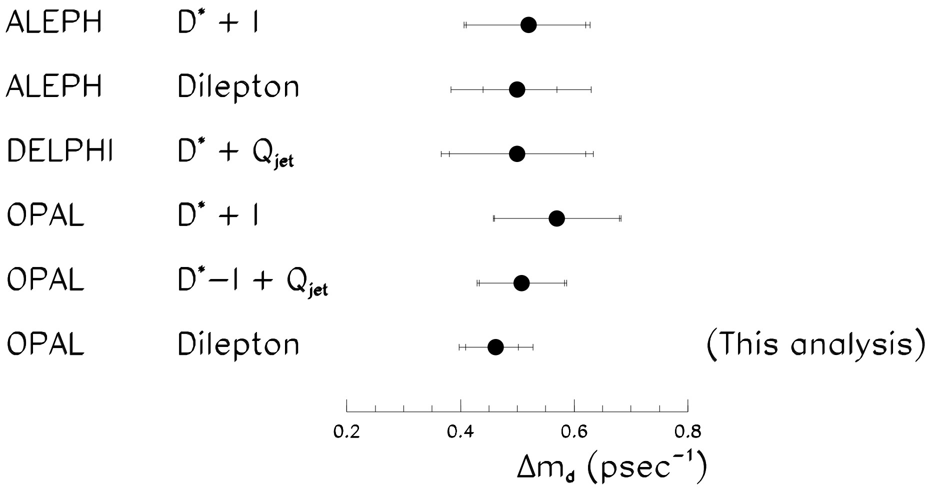

Figure 5.1: The comparison with previous Δm_d measurement.

5.2 CKM Matrix

The value of Δm_s divided by Δm_d provides information on the CKM matrix elements, $V_{\rm ts}$ and $V_{\rm td}$. This relationship has been calculated as $\Delta m_s/\Delta m_d = (1.35 \pm 0.15)|V_{\rm ts}/V_{\rm td}|^2$ [89].

In order to set the lower limit on $|V_{\rm ts}/V_{\rm td}|$, the observed proper time distribution was fitted with the parameter $|V_{\rm ts}/V_{\rm td}|$. The Gaussian constraint for this ratio was imposed as $(\Delta m_s/\Delta m_d)/|V_{\rm ts}/V_{\rm td}|^2 = 1.35 \pm 0.15$. The difference between the log-likelihood function and its minimum is shown in figure 5.2 as a function of $|V_{\rm ts}/V_{\rm td}|$. The point $\Delta \ln \mathcal{L} = 1.92$ is defined as the lower limit for $|V_{\rm ts}/V_{\rm td}|$, which is 1.72 at 95% C.L..

5.3 Future Prospects

The possible lower limit on Δm_s was investigated by the Toy Monte Carlo samples in case the statistics was twice (~3.0 multihadronic events (MH)), four times (~6.0 MH) and eight times (~12.0 MH). The results are shown in figure 5.3.

If there are more statistics, the lower limit of Δm_s will be increased even if the present method is not improved. The number of $Z^0 \to q\bar{q}$ events in 1994 data is about 1.5 MH. So, if this study is repeated including 1994 data, the observed lower limit of Δm_s is expected to be about 3.0 psec^{-1}. If some new techniques, for example, three dimensional secondary vertex finder, is adopted, this limit will be improved further.

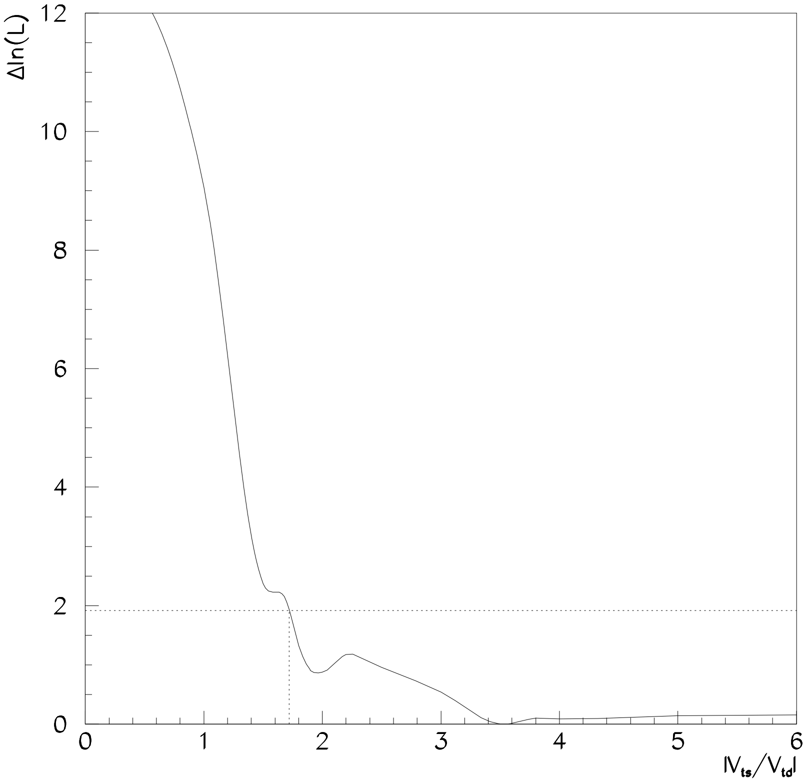

Figure 5.2: The log-likelihood value as a function of $|V_{ts}/V_{td}|$.

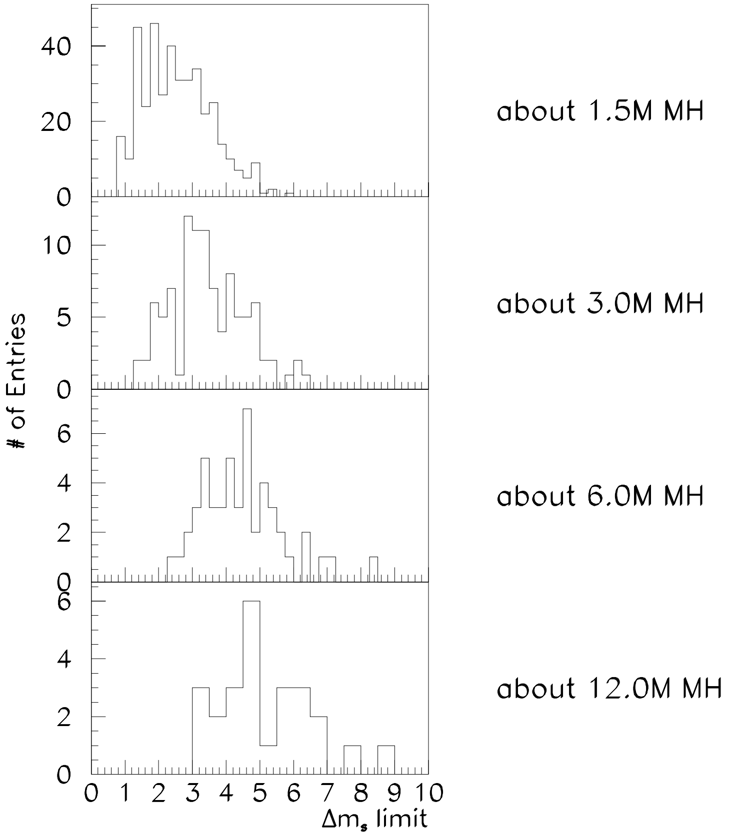

Figure 5.3: The lower limit for Δm_s for each statistics.

Chapter 6

Conclusion

The neutral B meson oscillations were studied using dilepton events and the mass difference of the B_d meson was measured to be

$$\begin{aligned}\Delta m_d &= 0.462\ {}^{+0.040}_{-0.053}\ {}^{+0.037}_{-0.036}\ \mathrm{psec}^{-1}\\ &= (3.04\ {}^{+0.26}_{-0.35}\ {}^{+0.34}_{-0.22}) \times 10^{-4}\ \mathrm{eV}\end{aligned}$$

where the first error is a statistical error and the second is a systematic error. This value is consistent with the previous OPAL measurements of Δm_d. The combined OPAL value for Δm_d is

$$\Delta m_d = 0.496 \pm 0.046\ \mathrm{psec}^{-1}.$$

Supposing B_d lifetime to be 1.50 ± 0.10 psec, this value corresponds to

$$x_d = \Delta m_d \tau = 0.74 \pm 0.07 \pm 0.05$$

where the last error is due to the uncertainty of the lifetime of B_d meson. This value is consistent with the previous ARGUS and CLEO measurements of $x_d = 0.68 \pm 0.08$ [86].

The lower limit on the mass difference of B_s meson was also obtained. The obtained lower limit was

$$\Delta m_s > 2.2\ \mathrm{psec}^{-1}\ \text{at}\ 95\%\ \text{C.L.}$$

These results of Δm_d and Δm_s are consistent with other previous ones.

Acknowledgments:

This work has been done as a part of the OPAL experiment and I would like to thank all of the physicists and the engineers participated in this project. I would like to thank Prof. Hiroshi Takeda who gave me an opportunity to join this experiment.

Special thanks are due to Prof. Sachio Komamiya and Dr. Masahiro Morii for providing me with many ideas in this analysis. I am also greatful to the members of the International Center for Elementary Particle Physics (ICEPP) for their fruitful discussions and advice.

I would like to thank Dr. Martin Jimack and Dr. Robert Kowalewski who collaborated with me and made many bright suggestions to this analysis. Without their help, I would have never completed this thesis.

It is also a pleasure to thank the SL Division for the efficient operation of the LEP accelerator, the precise information on the absolute energy, and their continuing close cooperation with our experimental group. I am pleased to acknowledge the following agencies for their support to the experiment;
Department of Energy, USA,
National Science Foundation, USA,
Particle Physics and Astronomy Research Council, UK,
Natural Sciences and Engineering Research Council, Canada,
Fussefeld Foundation,
Israel Ministry of Science,
Israel Science Foundation, administered by the Israel Academy of Science and Humanities,
Minerva Gesellschaft,
Japanese Ministry of Education, Science and Culture (the Monbusho) and a grant under the Monbusho International Science Research Program,
German Israeli Bi-national Science Foundation (GIF),
Direction des Sciences de la Matière du Commissariat à l'Energie Atomique, France,
Bundesministerium für Forschung und Technologie, Germany,
National Research Council of Canada,
A.P. Sloan Foundation and Junta Nacional de Investigação Científica e Tecnológica, Portugal.

Bibliography

[1] S. Weinberg, Phys. Rev. Lett. **19** (1967) 1264.
A. Salam, in *"Proceeding of the 8th Nobel Symposium"*, p.367.

[2] UA1 Collaboration, C. Albajar *et al.*, Phys. Lett. **B186** (1987) 247.

[3] ARGUS Collaboration, R. Albrecht *et al.*, Phys. Lett. **B 192** (1987) 245.
CLEO Collaboration, M. Artuso *et al.*, Phys. Rev. Lett. **62** (1989) 2233.

[4] ALEPH Collaboration, D. Buskulic *et al.*Phys. Lett. **B313** (1993) 498.

[5] ALEPH Collaboration, D. Buskulic *et al.*Phys. Lett. **B322** (1994) 441.

[6] OPAL Collaboration, R. Akers *et al.*Phys. Lett. **B327** (1994) 441.

[7] OPAL Collaboration, R. Akers *et al.*Phys.Lett. **B 336** (1994) 585.

[8] DELPHI Collaboration, P. Abreu *et al.*, Phys. Lett. **B 338** (1994) 409.

[9] CDF Collaboration, F. Abe *et al.*, FERMILAB-PUB-94/097-E.

[10] Particle Data Group, 'Review of Particle Properties', Phys. Rev. **D 50** (1994) 1173.

[11] S. L. Glashow, I. Illiopoulos and L. Maiani, Phys. Rev. **D 2** (1970) 1285.

[12] M. Kobayashi and T. Maskawa, Prog. Th. Phys. **49** (1973) 652.

[13] L. Wolfenstein, Phys. Rev. Lett. **51** (1983) 1945.

[14] R. Forty, CERN-PPE/94-154, to appear in Proc. of ICHEP Conference, Glasgow, July 1994.

[15] W. J. Marciano and A. Sirlin, Phys. Rev. Lett. **56** (1986) 22.
A. Sirlin and R. Zucchini, Phys. Rev. Lett. **57** (1986) 1994.
W. Jaus and G. Rasche, Phys. Rev. **D 35** (1987) 3420.
A. Sirlin, Phys. Rev. **D 35** (1987) 3423.

[16] H. Leutwyler and M. Roos, Z. Phys. **C 25** (1984) 91.
See also the earlier work of R. E. Shrock and L. L. Wang, Phys. Rev. Lett. **41** (1978) 1692.

[17] M. Bourquin *et al.*, Z. Phys. **C 21** (1983) 27.

[18] H. Abramowicz *et al.*, Z. Phys. **C 15** (1982) 19.

[19] C. Foudas *et al.*, Phys. Rev. Lett. **64** (1990) 1207.

[20] D. Hitlin, in *Proceedings of the 1987 International Symposium on Lepton and Photon Interactions at High Energies*, Hamburg, July 27–31, 1987, edited by W. Bartel and R. Rückl (North Holland, Amsterdam, 1988), p.179.

[21] CLEO Collaboration, A. Bean *et al.*, Phys. Lett. **B 317** (1993) 647.
Mark III Collaboration, J. Adler *et al.*, Phys. Rev. Lett **62** (1989) 584.
Mark III Collaboration, Z. Bai *et al.*, Phys. Rev. Lett **66** (1991) 1011.

[22] E691 Collaboration, J. R. Raab *et al.*, Phys. Rev. **D 37** (1988) 2391.
E687 Collaboration, P. L. Frabetti *et al.*, Phys. Lett. **B 263** (1991) 584.

[23] T. M. Aliev *et al.*, Yad. Fiz. **40** (1984) 823 [Sov. J. Nucl. Phys. **40** (1984) 527].

[24] M. Bauer, B. Stech and M. Wirbel, Z. Phys. **C 29** (1985) 637.
B. Grinstein, N. Isgur and M. B. Wise, Phys. Rev. Lett. **56** (1986) 56.
B. Grinstein, N. Isgur, D. Scora and M. B. Wise, Phys. Rev. **D 39** (1989) 799.

[25] F. Bartelt *et al.*, Phys. Rev. Lett. **71** (1993) 4111.
H. Albrecht *et al.*, Phys. Lett. **B 255** (1991) 297.
M. Danilov, rapporteur's talk at the *1993 EPS Conference on High-Energy Physics*, (Marseille, France, July, 1993).

[26] G. Altarelli *et al.*, Nucl. Phys. **B 208** (1982) 365.

[27] H. Albrecht *et al.*, Z. Phys. **C 57** (1993) 47.
H. Albrecht *et al.*, Phys. Lett. **B 275** (1992) 195.
G. Crawford *et al.*, CLEO Conf 93-30, submitted to *1993 EPS Conference on High-Energy Physics*, (Marseille, France, July, 1993).

[28] D. Karlen, *5th International Conference on heavy Flavor Physics* (Montreal, Canada, July, 1993).

[29] J. H. Christenson *et al.*, Phys. Rev. Lett. **13** (1964) 138.

[30] P. J. Franzini, Phys. Rep. **173** (1989) 1.
E. Psachos and U. Türke, Phys. Rep. **178** (1989) 145.

[31] ARGUS Collaboration, R. Albrecht *et al.*, Z. Phys **C 55** (1992) 357.

[32] ARGUS Collaboration, R. Albrecht *et al.*, Phys. Lett. **B 324** (1994) 249.

[33] CLEO Collaboration, M. Artuso *et al.*, Phys. Rev. Lett. **62** (1989) 2233.

[34] CLEO Collaboration, J. Bartelt *et al.*, Phys. Rev. Lett. **71** (1993) 1680.

[35] ALEPH Collaboration, D. Decamp *et al.*, Phys. Lett. **B 284** (1992) 177.

[36] DELPHI Collaboration, P. Abreu *et al.*, Phys. Lett. **B 322** (1994) 459.

[37] DELPHI Collaboration, P. Abreu *et al.*, CERN-PPE/94-67.

[38] L3 Collaboration, M. Acciarri *et al.*, CERN-PPE/94-89.

[39] OAPL Collaboration, R. Akers *et al.*, Z. Phys. **C 60** (1993) 199.

[40] UA1 Collaboration, C. Albajar *et al.*, Phys. Lett. **B 262** (1991) 171.

[41] CDF Collaboration, F. Abe *et al.*, Phys. Rev. Lett. **67** (1991) 3351.

[42] L. M. Jowett,*"Invited talk at the ICFA Seminar on Future Perspectives in High Energe Physics",DESY,Hamburg,*CERN SL/93-24(AP).

[43] R. Assmann *et al.*, CERN-SL/94-61 (AP).
L. Arnaudon *et al.*, CERN-SL/94-71 (BI).

[44] The OPAL Collaboration, K. Ahmet *et al.*, Nucl. Inst. and Meth. **A 305** (1991) 175.

[45] P. P. Allport *et al.*, Nucl. Inst. and Meth. **A 324** (1993) 34.
P. P. Allport *et al.*, Nucl. Inst. and Meth. **A 346** (1994) 476.

[46] NE110 scintillator, from Nuclear Enterprises.

[47] XP2262B phototubes, from Philips Components, 5600 MD Eindhoven, The Netherlands.

[48] An Ji-Gang *et al.*, Nucl. Inst. and Meth. **A 267** (1988) 386.

[49] An Ji-Gang *et al.*, Nucl. Inst. and Meth. **A 267** (1988) 396.

[50] SF57 lead glass, from Schott Glaswerke, Hattenbergstrasse 10, D-6500 Mainz 1, Germany. This glass has the following properties: 75% by weight PbO, density 5.54 g$\cdot$cm^{-3}, $X_0 =$ 1.50 cm, and refractive index 1.8467 at $\lambda = 586$ nm.

[51] R2238 phototubes, from Hamamatsu Photonics K.K., Ichino-cho, Hamamatsu, Japan. These phototubes have the following properties: 12-stage mesh dynodes, effective diameter of bialkali photocathode 70 mm, nominal amplification factor $\sim 1.0 \times 10^5$ at a typical high voltage of -1.0 kV.

[52] Cemedine 1565 adhesive, from Cemedine Co., Ltd., 5–9, Higashigotanda 4-chome, Shinagawa-ku, Japan. This adhesive has a refractive index of 1.56 at $\lambda = 586$ nm.

[53] TMB permaloy metal, from Tokin Corporation, 7–1, Kooriyama 6-chome, Sendai, Japan.

[54] C. Beard *et al.*, Nucl. Inst. and Meth. **A 286** (1990) 117.

[55] M. Akrawy *et al.*, Nucl. Inst. and Meth. **A 290** (1990) 76.

[56] M. Akrawy *et al.*, Submitted to Nucl. Inst. and Meth **A.**

[57] CEREN-25 lead glass, from Corning France, 44 Avenue de Valvins, Avon, Cedex 77210, France. This glass has the following properties: 55% by weight PbO, density 4.06 g$\cdot$cm^{-3}, $X_0 = 2.51$ cm, and refractive index 1.708 at $\lambda = 400$ nm.

[58] M. D. Rousseau *et al.*, IEEE Trans. Nucl. Sci. NS-30 (1983) 479.

[59] J. Allison *et al.*, Nucl. Inst. and Meth. **A 236** (1985) 284.

[60] J. Allison *et al.*, Submitted to Nucl. Inst. and Meth **A.**

[61] D. C. Imrie *et al.*, Nucl. Inst. and Meth. **A 238** (1989) 515.

[62] B. E. Anderson *et al.*, Nucl. Inst. and Meth. **A 238** (1989) 650.

[63] M. Arignon *et al.*, Nucl. Inst. and Meth. **A 313** (1992) 103.

[64] J. T. M. Bains *et al.*, Nucl. Inst. and Meth. **A 325** (1993) 271.
A data acquisition and experimental control system for the OPAL experiment at the CERN LEP collider, presented by S. Wotton at the 2nd Int. Conf. on Advanced Technology and Particle Physics, 1990.

[65] MC68020, MV68030 32-bit Microprocessors; Motorola Inc.

[66] OS9 is a single processor, multi-tasking Operation Systemfor the 68000 processor family; Microwave Systems corporation, 1900 N.W. 114th Street, Des Moines, IA 50322, USA.

[67] IEEE 1014/D1.0.

[68] ZEBRA Data Structure Management System; CERN Computer Centre Library.

[69] The OPAL Collaboration, G. Alexander *et al.*, Z. Phys. **C 52** (1991) 175.

[70] T. Sjöstrand, Comp. Phys. Comm. **39** (1986) 347
M. Bengtsson and T. Sjöstrand, Comp. Phys. Comm. **43** (1987) 367
M. Bengtsson and T. Sjöstrand, Nucl. Phys. **B 289** (1987) 810
T.Sjöstrand, CERN-TH/92-6488.

[71] Parameter values were tuned to describe global event shape variables:
OPAL Collaboration, M. Akrawy *et al.*, Z. Phys. **C 47** (1990) 505.

[72] J. Allison *et al.*, Nucl. Instrum. Methods **A 317** (1992) 47

[73] C. Peterson, D. Schlatter, I. Schmitt and P. M. Zerwas, Phys. Rev. **D 27** (1983) 105.

[74] The OPAL Collaboration, P. Acton *et al.*, Z. Phys. **C 58** (1993) 523.

[75] LEP Electroweak Working Group notes LEPHF/94-01 and LEPHF/94-02 list suggested values and ranges for parameters used in heavy flavor analyses at LEP. These notes contain references to the measurements and procedures from which the parameters ranges are derived.

[76] D. Bardin *et al.*, *ZFITTER, An Analytical Program for Fermion Pair Production in* e^+e^- *Annihilation*, CERN-TH.6443/92. For this prediction, the Z^0, top quark, and Higgs boson masses are set to $M_{Z^0} = 91.18$ GeV/c^2, $M_{\rm top} = 150$ GeV/c^2 and $M_{\rm Higgs} = 300$ GeV/c^2, and $\alpha_s = 0.12$.

[77] ALEPH Collaboration, D. Buskulic *et al.*, Phys. Lett. **B 322** (1994) 275.
ALEPH Collaboration, D. Buskulic *et al.*, Phys. Lett. **B 314** (1993) 459.
ALEPH Collaboration, D. Buskulic *et al.*, Phys. Lett. **B 307** (1993) 194.
ALEPH Collaboration, D. Buskulic *et al.*, Phys. Lett. **B 295** (1992) 396.
DELPHI Collaboration, P. Abreu *et al.*, Z. Phys. **C 63** (1994) 3.
DELPHI Collaboration, P. Abreu *et al.*, Phys. Lett. **B 312** (1993) 253.
DELPHI Collaboration, P. Abreu *et al.*, Phys. Lett. **B 311** (1993) 379.
OPAL Collaboration, P. Acton *et al.*, Z. Phys. **C 60** (1993) 217.

OPAL Collaboration, R. Akers *et al.*, Phys. Lett. **B 316** (1993) 435.
OPAL Collaboration, P. Acton *et al.*, Phys. Lett. **B 307** (1993) 247.
OPAL Collaboration, P. Acton *et al.*, Phys. Lett. **B 312** (1993) 501.

[78] CDF Collaboration, F. Abe *et al.*, Phys. Rev. Lett. **71** (1993) 3421.
CDF Collaboration, F. Abe *et al.*, Phys. Rev. Lett. **72** (1994) 3456.

[79] The production of strange quark pairs in the fragmentation was tuned to reproduce the inclusive K^0_S yield measured in
OPAL Collaboration, G. Alexander *et al.*, Phys. Lett. **B 264** (1991) 467.

[80] OPAL Collaboration, R. Akers et al., Phys. Lett. B327 (1994) 411.

[81] OPAL Collaboration, P. Acton *et al.*, Z. Phys. **C 58** (1993) 523.

[82] OPAL Collaboration, R. Akers *et al.*, Z. Phys. **C 60** (1993) 199.

[83] The OAPL Collaboration, R. Akers *et al.*, Z. Phys. **C 63** (1994) 197.

[84] ALEPH Collaboration, D. Buskulic *et al.*, Phys. Lett. **B 294** (1992) 145.
OPAL Collaboration, P. Acton *et al.*, Phys. Lett. **B 295** (1992) 357.

[85] ALEPH Collaboration, D. Buskulic *et al.*, CERN-PPE/94-173, submitted to Phys. Lett. **B**. OPAL Collaboration, R. Akers *et al.*, CERN-PPE/95-02, submitted to Z. Phys. **C**.

[86] The results in reference [31, 34] were combined by M. Danilov. Presented at the International Europhysics Conference on High Energy Physics, Marseille, July 1993.

[87] OPAL Collaboration, R. Akers *et al.*, CERN-PPE/106, submitted to Z. Phys. **C**.

[88] F. Pierre, to appear in Proc. of V Int. Symp. on Heavy Frav. Phys., Montreal (1993).

[89] Y. Nir, Phys. Lett. **B 327** (1994) 85.
A. Ali and D. London, CERN-TH/94-7398, submitted to Z. Phys. **C**.